January 2021

Development Of Image Processing Techniques For Core-Scale Characterization And Synthetic 3D-Printed Core Replicas

Ahmed Galal Alqassaby Almetwally

Development of Image Processing Techniques for Core-Scale Characterization and Synthetic 3D-Printed Core Replicas

by

Ahmed Galal Alqassaby Almetwally

Bachelor of Science, Cairo University, 2012

Master of Science, Cairo University, 2017

A Thesis

Submitted to the Graduate Faculty

of the

University of North Dakota

in partial fulfillment of the requirements

for the degree of

Master of Science

Grand Forks, North Dakota

May

2021

This thesis is submitted by (**Ahmed Galal Alqassaby Almetwally**) in partial fulfillment of the requirements for the Degree of Master of Science in petroleum engineering from the University of North Dakota, has been read by the Faculty Advisory Committee under whom the work has been done and is hereby approved.

_____

Dr. Hadi Jabbari, Chairperson, Date

_____

Dr. Minou Rabiei, Co-advisor, Date

_____

Dr. Vamegh Rasouli, Co-advisor, Date

_____

Dr. Mohammad Khavanin, Member at Large, Date

This thesis is being submitted by the appointed advisory committee as having met all of the requirements of the School of Graduate Studies at the University of North Dakota and is hereby approved.

_____

Chris Nelson

Dean of the School of Graduate Studies

_____

Date

Title: Development of Image Processing Techniques for Core-Scale Characterization and Synthetic 3D-Printed Core Replicas

Department: Petroleum Engineering

Degree: Master of Science

In presenting this thesis in partial fulfillment of the requirements for a graduate degree from the University of North Dakota, I agree that the library of this University shall make it freely available for inspection. I further agree that permission for extensive copying for scholarly purposes may be granted by the professor who supervised my dissertation work or, in his absence, by the Chairperson of the department or the dean of the Graduate School. It is understood that any copying or publication or other use of this dissertation or part thereof for financial gain shall not be allowed without my written permission. It is also understood that due recognition shall be given to me and to the University of North Dakota in any scholarly use which may be made of any material in my dissertation.

Ahmed Galal Alqassaby Almetwally

May 01, 2021

Table of Content

Page

List of Figures

List of Tables

Acknowledgment

This sincere acknowledgment goes to my advisor, Dr. Hadi Jabbari, whose support made the presented research a possibility. Further, I would like to acknowledge the support of the Petroleum Engineering Department at UND for providing me with the appropriate resources to finish the assigned research tasks. I would also like to thank Dr. Vamegh Rasouli and Dr. Minou Rabiei for providing their valuable inputs for editing the work. I want to express my foremost acknowledgment to my UND-EERC supervisors, Charlene Crocker and Lu Jin, for supporting me during my summer internships at UND-EERC. Lastly, I would like to express my gratitude for the spectacular offered support by my family during the thesis.

I would like to thank the American Chemical Society Petroleum Research Fund (ACS-PRF) for their financial support, through the contract of ACS-PRF No. 58746 (2017) for the grant award: A New Approach to Quantifying Adsorption/Diffusion Characteristics of Shale Formations. I would also like to thank Statoil (operator of the Norne field) and its license partners ENI and Petoro for the release of the Norne data. Further, the authors acknowledge the Center for Integrated Operations at NTNU for cooperation and coordination of the Norne Cases.

Abstract

Objectives/Scope:

Fluid-flow physics in porous media has been continually simplified by assuming isotropic homogeneous media with minimal rock-fluid interactions. Such simplification did not reflect reality and retained the ability to understand the flow behavior essence in unconventional reservoirs. The developed physics should be reevaluated on ideal porous media, indeed, which has minimal geometrical and interaction uncertainties. Therefore, image processing techniques were utilized to processs the CT scans of core samples to construct ideal 3D-printed replicas for coreflooding experiments and simulation models. The results from both were then compared for vcalidation and cross check.

Methods, Procedures, Process:

Grayscale CT-scan of a Berea core sample was digitally binarized to segment the grains cloud in the scan. That cloud was meshed and triangulated to form a 3D-printable object. The processed object was 3D printed with different 3D printing technologies and materials. The gypsum-replica, which had the closest petrophysical properties to the original Berea, was extensively investigated through a CO2 huff and puff experiment simultaneously with its original, geomechanical UCS (uniaxial compression strength) test, Nitrogen sorption, MICP (Mercury Injection Capillary Pressure), and contact angle wettability measurement.

Based on the image processed CT scan, a finite difference model was created in which the petrophysical characteristics, porosity and permeability, were inferred from the CT scan. The model was used to simulate a transient permeability experiment on the Berea sample and the CO2 huff and puff experiment. The 3D printable volume was also used to create a finite element model to simulate the UCS test on the replica. Figure 1 shows the 3D printed replicas with their original Berea along with the coreflooding and geomechanical simulation models based on the reconstructed CT scan.

Results, Observations, Conclusions:

The 3D printed replica was able to represent their original sample with close storage and transport capacities. The used image processing workflow generated a precise static model for black oil (transient permeability) and compositional simulation models (CO2 huff and puff) of both samples. The CO2 effect on the core sample was pictured after breaking the replica to check its interior, and the simulation model was able to predict a similar saturation distribution. The simulation results accurately matched the replica's measured oil recovery, pressure distribution during the transient permeability test. After including the UCS test schedule, the model succeeded in generating fatigue iso-surfaces, stress and strain contours, failure limits and modes, force reactions inside the core sample.

Novel/Additive Information:

The proposed image processing can produce the physical specimens for tests along with the needed models to simulate these tests. 3D-printed core replicas, which are created by reconstructing cores' CT scans by image processing, are valuable for repetitive and destructive experiments and obey the criterion

of ideality for laboratory research. The created coreflooding and geomechanical models are robust and precise for developing and understanding the physics of fluid flow in porous media.

1 Introduction

Understanding the fluid flow physics in porous media is essential to enhance reservoir management. Complexity associated with characterizing reservoir rocks and rock/fluid interactions is multifold. In the laboratory studies, especially repeated destructive experiments, the challenges of using real core-plugs include high acquiring cost, preserving to in-situ conditions, samples damage. Another challenge is the accurate characterization of uncertain pore network structure which is crucial in understanding the storage capacity and mass transport of fluids, especially in an EOR process and unconventional samples. Cheap 3D-printed core-plugs can help to avoid such problems with accurate 3d-printed pore network and with a uniform printing material which has a predictable fluid interaction. In this work, a new methodology is proposed to reconstruct the core-plugs' CT-scan data to create representative 3D-printable porous replicas. Image processing tools were used to segment the grains and pores in CT-scan data. The processed segmented CT volume is then converted from grayscale images to a binarized continuous volume to be meshed in a 3D-printable format. Finally, synthetic samples were produced by using different base and binding materials (i.e. gypsum/sandstone and plastics). Acceptable measured petrophysical properties for each replica (e.g. porosity and permeability) match the understudy core-plug (Berea sandstone) properties.

Petroleum practitioners rely heavily on laboratory work for visualizing the fluid flow in porous media by acquiring images to get a better understanding of the rock/fluid interaction physics. Most of the laboratory work starts with performing micro computed tomography (CT) imaging/scanning for the sake of preserving a soft image before any further destructive experiments on the core plugs and to be used also as a base reference for pore network modeling. Hence, CT scanning of core samples is of a great importance to the oil and gas industry.

CT scanning output is a series of 2D images. These 2D images can be visually analyzed by using light boxes and/or computers. CT is widely used by many researchers in characterizing the microscopic structures of rock samples: actual shape, size, and spatial distribution of the grains and voids inside samples, specially, in heterogeneous rock sample [1].

.In digital rock physics simulation workflows, the petrophysical properties (i.e. porosity, permeability, etc.) are estimated based on the CT scan of rock samples [2]. These properties and the inferred skeleton of the pore network help us to construct 3D conceptual model for the rock samples. That 3D model can be used for simulation purposes (core flooding or geomechnical tests modelling), experimental sensitivity studies and 3D printing technology (synthetic cores). Synthetic 3D printed cores have many advantages. They are repeatable, flexible, controllable, precise (but technology sensitive), time and effort saver, and economical [3]. It is very important to examine the validity of using such synthetically created 3D core plugs in laboratory studies, specially the destructive experiments, and simplifying/testing fluid flow physics in complex problems using these well-known 3D printed specimens (known material and pore network) for simulation validation purposes.

Repeatability of original cores is a key benefit of 3D printing [4]. Using 3D printing technology to prepare multiple core samples can eliminate the variability of pore network and static/dynamic properties of samples (and with lower costs) in repeated laboratory tests. Regarding the pore network

characterization, many researchers have worked to characterize pore network structures quantitatively with different direct imaging methods [5] and indirect methods [6]. Pore space configuration is the hydrocarbon flow paths. The ideal connectivity with a perfect digital description for the tortuosity of the flow path is a numerical challenge to define and to describe from any possible characterization mean. We can alleviate such uncertainty problem with 3D printing since the user has control over the generated 3D printing mesh and thus pore network structure.

The variabilities of static and transport properties arise from different lithology and mineralogy at each point in rock samples. Using a single 3D printing material can make it easier to comfortably use the assumption of uniform lithology and mineralogy of core samples in analytical and numerical models along with the easiness of measuring their uniform and predictable petrophysical, mechanical, and electrical properties based on the same conceptual model for the original core sample and under different conditions of pressure and temperature.

It is a challenging task to create 3D conceptual models automatically from 2D CT scans due to possible topologic and/or geometric errors, which requires further manual adjustments of the conceptual model mesh to produce a high quality 3D printed structure. These types of errors relate to the unclear and ambiguous documented processing algorithms for converting the 2D scans to a 3D skeleton, also to the limitations of 3D printing technology maximum feasible resolution, and generation of valid mesh files for manufacturing.

This paper proposes a robust methodology for automatically generating 3D porous printed models from 2D CT scan data for a full size core plug. This new approach is based on CT scan data volume reconstruction to be used in generating the resulting 3D printing surfaces. This approach differs from the existing methodologies of 3D printing which are based on 3D printing a small upscaled part of the pore network model not the CT scan data directly or the whole core plug as in [4] or 3D printing a solid not porous cylinder with a gypsum powder [3] to make it porous depending on the powder porosity.

This new approach for 3D reconstruction of a rock sample was applied to the CT scan data of a Berea sandstone core plug and the resulting 3D structure was utilized for 3D printing the sample with different materials and 3D printing technologies. Next, the static/dynamic properties (e.g. porosity and permeability) of the synthetic core samples were measured to compare several printing technologies which were tested in this study. The proposed workflow of the study is described below.

1.1 Process Overview

CT slices are cross sectional bitmaps that describe the geometrical/anatomical configuration of the scanned plane of core. The whole CT series of slices contain information regarding the entire core at regular intervals.

The process of generating a 3D conceptual model for 3D printing based on CT scan data includes:

1. Acquisition of 2D CT scan images
2. Conducting image processing including a two-step procedure:

   A. Image segmentation to distinguish the pore network (i.e. pores vs. grains) based on the grayscale value
   B. Converting the images from grayscale to digital binary bitmaps (i.e. 0 and 1)
3. Volume reconstruction procedure
4. Mesh generation based on the reconstructed core volume and storing it in a required 3D printing format (e.g. stereolithography; .STL file)
5. Mesh refinement before 3D printing the model

Berea sandstone core plug was used in this work (1.5 inches in diameter and 2 inches in length) with porosity and permeability measured as 20% and 100 mD respectively (**Figure 1**). Berea sandstone is a standard commercial source for sandstone core plugs, located in Ohio, USA, which is known to be well-sorted angular, fine quartz sandstone with a composition of mostly 87 to 93% quartz by volume with minor feldspar 3 to 9%, 0.5 to 3% dolomite, and 0.5 to 7% clays [7].

Figure 1.1: Original Berea sandstone core plug (1.5 inch in diameter and 2 inch in length)

These homogeneous properties and others like pore throat diameters range from 50 to 150 μm [8] can be perfect choice to avoid the limitation of the 3D printing maximum resolution to print a higher resolution (Fine grains or smaller pore throats). According to [9], a core sample should be selected properly to fit the current 3D printing technology and the abrupt changes in the sample structure should be avoided also to enable printing without geometrical errors.

The following explains the steps of the proposed approach for reconstructing CT scans to generate the conceptual model and create synthetic 3D printed core plugs along with the required concepts to be familiar with the proposed approach; CT imaging, mesh file format (*.STL), image processing techniques, converting 2D scan data into 3D conceptual models, 3D printing technology and selection of materials.

1.1.1 Acquisition of 2D CT Scan Images

CT is used as a tool for generating a visual representation of the interior structure of a core plug geometry. A CT scanner is utilized to generate cross-sectional slices along the core sample. A series of slices contain geometrical information through the entire core at regular intervals. These intervals are

determined by the user according to the sample size and the CT scanner capabilities. **Figure 2** shows a collection of selected CT slices along the scanned core plug (Berea sandstone). The CT scanner mainly consists of a source of X-ray beam and opposite detectors series. The X-ray beam attenuates while passing through the core sample [10]. A recorded CT scan is a measure of the attenuation of such X-ray beams (the X-ray absorption by the sandstone grains) as it passes through the object. Back projection is then applied to infer the material (grains and pores) density at each point in the core [11].

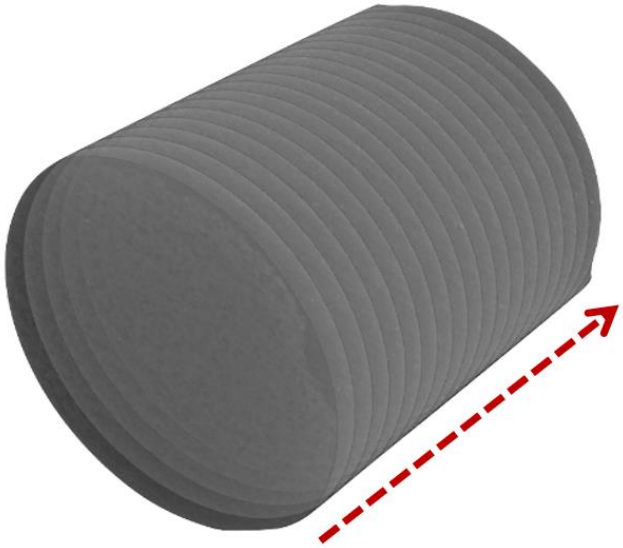

Figure 1.2: A combination of selected CT slices along the core plug

It is very important to understand the resolution aspects of CT scanning, which are related to the number of slices we can obtain along the core and to the lateral XY resolution.

There are two important resolution definitions: the XY resolution in the scan plane (spatial), and the along-the-axis resolution (Z-resolution or the separation between 2 scanned planes). The XY-resolution (i.e. in plane) is mainly representing the size of a squared pixel in the X and Y directions. A CT image has typically an XY pixel resolution of 512 x 512 pixel (Goldman, 2007). This scanner range should cover the whole cross section of the core. The XY resolution is strongly dependent on the field of view (sample size). If the core sample size is relatively small, then a higher XY spatial resolution is obtained and vice versa. We can find out the aspect ratio between the cross sectional area of the core 1.5 inch (38 mm in X direction x 38 mm in Y direction) in diameter over the number of pixels in each direction to find the area covered by each pixel. There are rules of thumb to tune the CT lateral resolution to match the 3D printer requirements and to avoid having too much redundant data [9].

The along-the-axis resolution (Z-resolution) is much less than that in the XY plane and the separation between two slices of the original core plug may be between from 0.1 to 1 mm. Thus, the volumetric generated voxels have a typical X:Y:Z aspect ratio ranges of 1:1:2 to 1:1:20. This means that in a Berea core plug, which is 2 inches long (~ 58 mm), we obtained approximately 1000 CT slices along that core. The Z resolution/slice thickness is mainly affected by the acquisition method and the CT scanner power [12]. If the number of slices are not enough to generate a continuous volume for 3D printing without

errors, (Almetwally and Jabbari, 2019) [9] proposed an interpolation scheme between slices to grantee this continuity.

A montage of the selected CT scans from the Berea sandstone core understudy is shown in **Figure 3**. It is essential to visually track these slices to ensure the continuity in the pore network and notice the possible abrupt changes, which can indicate the existence of natural fractures or scanner malfunction as we progress from one slice to another. From the CT slices of the Berea core plug, we can see a uniform geometrical/anatomical configuration of the core except for the first and last slice of core which is consistent with the original core exterior edges because of the damage occurring while coring of the original core itself (see **Figures 7** and **8**).

Usually the pores in a CT scan take the black color and the grains are in gray depending on the minerals and the spatial resolution.

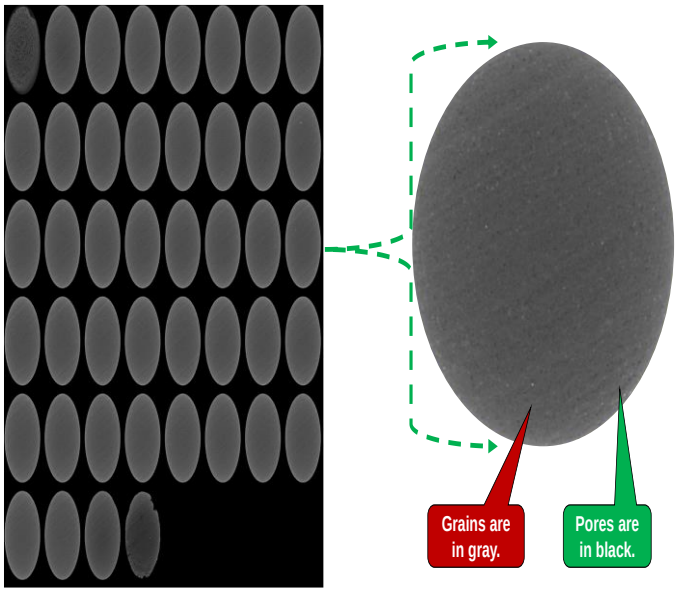

Figure 1.3: A montage from selected CT scans on the used Berea sandstone core

1.1.2 Image Processing

In this step of distinguishing the difference between pores and grains based on the grayscale pixel values, the threshold in the recorded response of the CT scans should be clearly determined for the acquired slices. The distinction between the grains and pores can be implemented by using the selected by user threshold on the CT scan gray scale histogram [13], which separates between different responses received from grains versus pores (see **Figure 4**). Other methods of particle recognition algorithms can be applied also to enhance this classification problem.

For CT grayscale images as shown in **Figure 3**, single numbers between 0 to 255 are generated as 8-bit integers. Each of which represents the brightness of the pixels. Typically, zero is set to be black, and 255 is set to represent white color [14].

In this work, we developed codes to conduct such supervised image processing and conversion. The histogram is generated by counting each integer between 0 to 255 in the bitmaps. The sandstone grains will have a hump to the far right side of the frequency histogram (i.e. the bright side) and the pores will skew towards the left-hand side of the histogram (i.e. the dark side). For CT scans with a high spatial resolution (i.e. on the XY plane), it is easier to visually see the two humps separated from each other. It may be challenging for larger samples with the reduction in the spatial resolution.

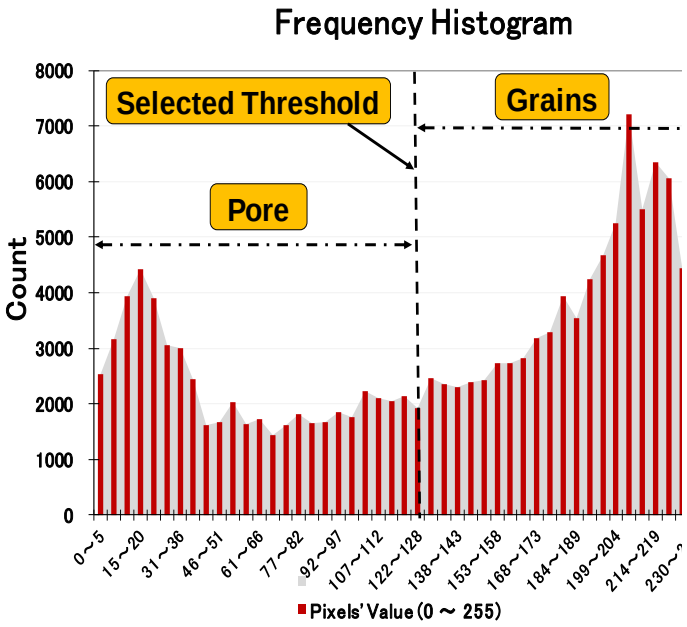

Figure 1.4: Grayscale histogram for all the CT scan slices

The selected threshold will let us to separate the two spectrums of pores and grains. The determination of such a threshold needs a trial and error process for establishing a clear distinction between pores and grains. The original core can help with inspecting the first and last slice to check the accuracy of this threshold. Note that this process is a crucial step for determining reliable pore network models and thus accurate *.STL files for 3D printing.

After determining the optimum threshold, all the CT images are digitally converted from a grayscale to binary (0 and 1) bitmaps. The importance of this step is preparing a volume that the 3D printer can handle as the 3D printer can understand only two objects (solid and void: nothing in between).

The zero value (i.e. black; the spectrum below the threshold. Zero (0) will replace all of the integers in that spectrum), is assigned to the pores while the one value (i.e. white; the spectrum above the threshold. One (1) will replace all of the integers in that spectrum) is assigned to the grains. As mentioned above, we should carry out this step with utmost care since for a 3D printer to work accurately, we need to prepare a robust stereolithography file (in *.stl format), which is a standard format for inputting the structure (i.e. pores and grains).

Figure 5, as an example, depicts the results from image processing a slice. On the left-hand side, it shows the original CT grayscale image which is binarized to 0 and 1 as shown on the right-hand side.

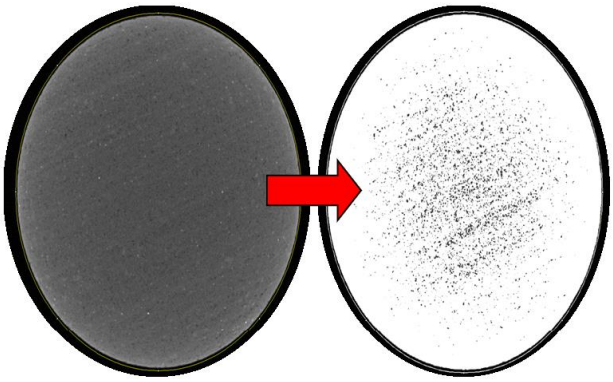

Figure 1.5: Binarization of a grayscale CT image (pores are shown are in black)

Similarly, all images are converted to the binary version. **Figure 6** illustrates a series of binary conversion for the slices.

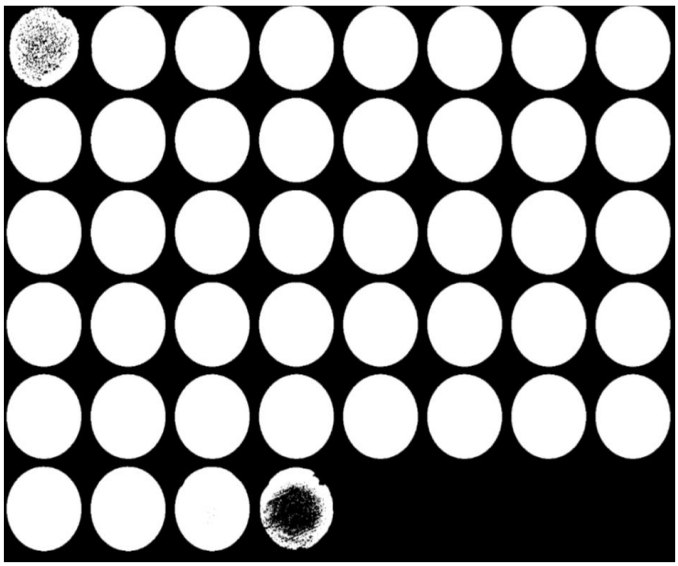

Figure 1.6: A binarized montage from selected CT scans on the used Berea sandstone core

Note that the grayscale histogram threshold to distinguish between pores and grains (see **Figure 4)** should be applied to each image individually. This is because the CT radiation intensity, and thus the image quality, is affected by the slice's relative position along the core plug. Hence, one single threshold determined for a slice would not result in accurate binarization process for other CT slices.

That being said, it will be a tedious task to obtain optimal thresholds for each slice of the image spectrum (1000 threshold for 1000 CT slice). In order to overcome such a problem, we proposed a methodology to train the image-processing program efficiently. The procedure includes calculating the mean of the pixels' value for each slice through all the CT slices (see **Figure 7)**.

For a homogenous core, this mean will be steady for all slices as long as there are no abrupt changes in core at any slice position. As shown in **figure 7**, it safe to apply the same distinction representative

threshold starting from slice number 50 to number 800. Any threshold based on a histogram from that range can be used as a global threshold. As for the first and last slices, the indentations observed in the original core has affected the CT scan image which gave more void space than the normal. These slices should be tweaked manually since they affect the rest of the CT slices.

In case of a none steady pixels' mean for the CT slices, it is highly recommended to normalize all slices to one acceptable range of colors. Another option is automatically applying a distinction threshold on each slice individually and a particle recognition algorithm should be applied to detected the grains accurately as the grayscale response is not uniform from one slice to another. A trained neural network model will efficiently track the grains and can be tested on some slices to check the validity. The only problem is the huge required memory to handle all CT slices in the background.

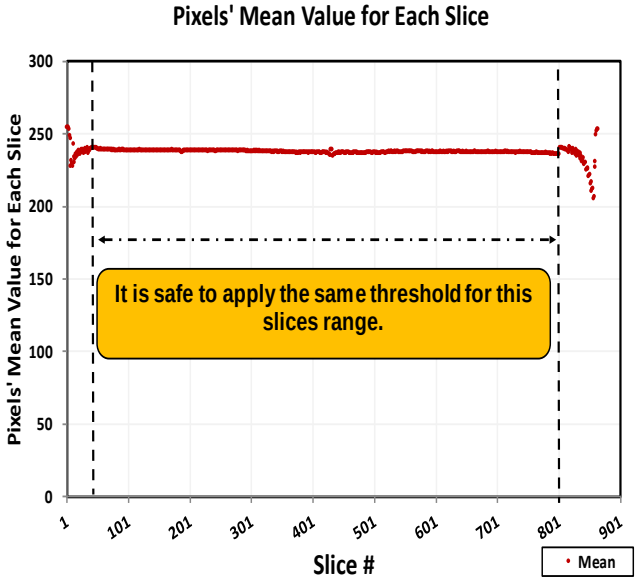

Figure 1.7: Pixels' mean value for each slice as guide to choose the distinction threshold between the grains and pores

1.1.3 Volume Reconstruction

The continuity of the object is essential for the 3D printer to work properly. Till now, we have created a spectrum of discrete slices which are not making up a continuous volume. So 3D interpolation, neural network model, and geostatistical algorithms are applied to connect the distinctive slices in order to establish the pore network model [9]. This step can be applied before or after the binarization process. As shown in **Figure 8**, the output will be a set of continuous orthogonal cross sections (lateral and longitudinal) in which we can track the pores along the core plug.

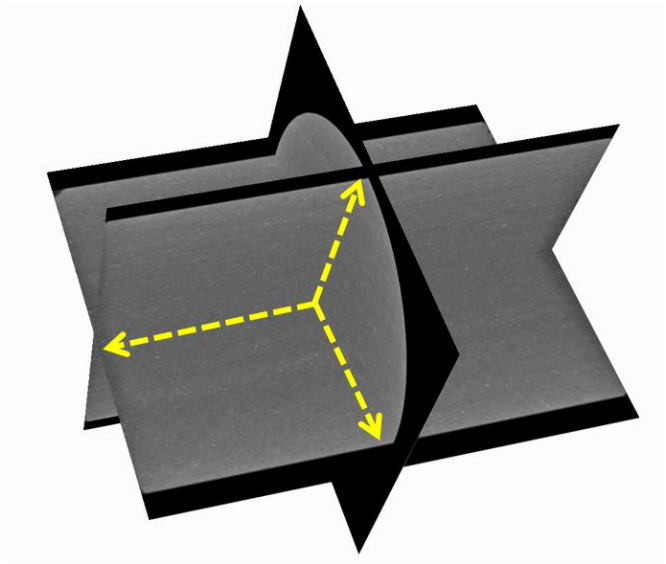

Figure 1.8: Lateral and longitudinal slices after filling the gaps between the slices

The generated volumetric geometry from these interpolation techniques can then be used as an input file for 3D printing, for pore network construction, core flooding simulation, and geomechanics simulation at core scale [9]. **Figure 9** shows the reconstructed volume of the Berea sandstone, from the above methodology in which each point in space of that final volume object file is the corresponding digital representation of the same point in the original core.

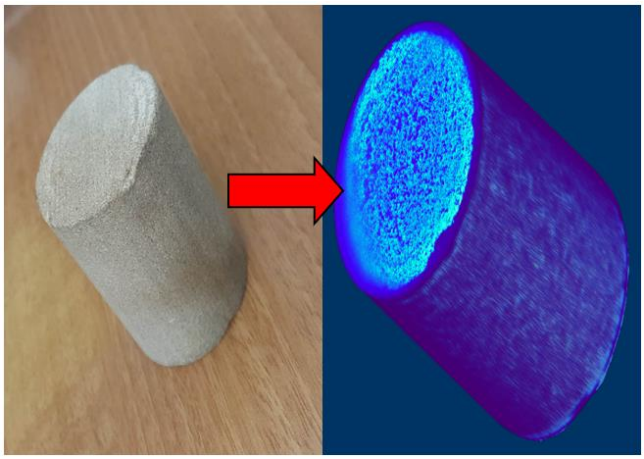

Figure 1.9: Reconstructed volume of the original core

1.1.4 Mesh generation file in 3D printing format

The stereolithography (*.STL) file format is a standard format that is used as input into a 3D printer apparatus. *.STL files are used to describe the surface geometry of an object with no determination of its color, texture or any other common attributes [15]. This type of files compiles a set of triangular facets (triangles vertices and unit normal in 3D Cartesian coordinates) into forming surfaces of an object.

Such triangles track the solid surfaces encapsulating the pores by connecting the points with binary values of one (i.e. grains) in the reconstructed binary (0 and 1) volume as shown in **Figure 10**.

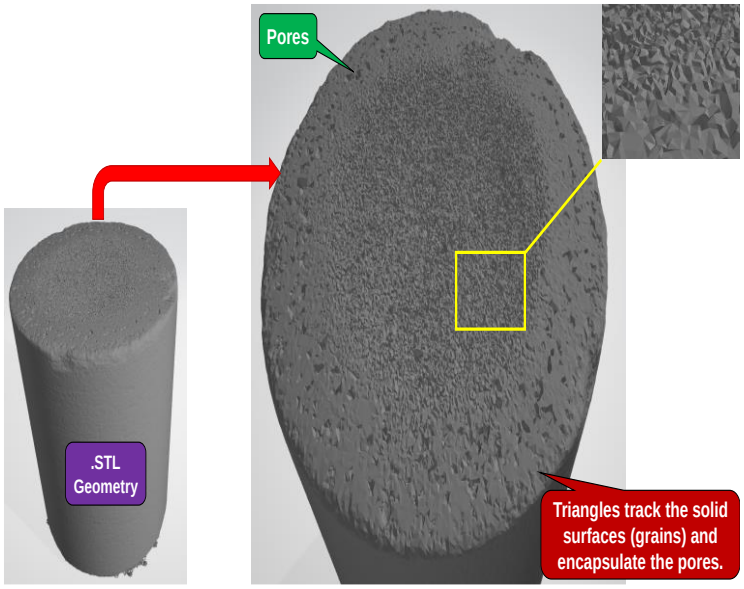

Figure 1.10: .STL geometry of triangles which track the solid surfaces (grains) and encapsulate the pores.

In order to prepare an accurate surface mesh file (*.stl), we need to perform a trial-and-error process (mesh refinement, step 5) and optimize a number of parameters to avoid discontinuity in the final model. These parameters include triangles area (minimized) and minimum triangle acute angles (maximized) to track grains/surfaces edges. **Figure 11** (RHS) shows the results from such a process for a Berea sandstone core plug (LHS). An accurate mesh file must reflect all the details of the original core plug such as pores, grains, and structure (see in **Figure 11** the small flaw on both prototype (Berea Core Plug) and 3D printable model).

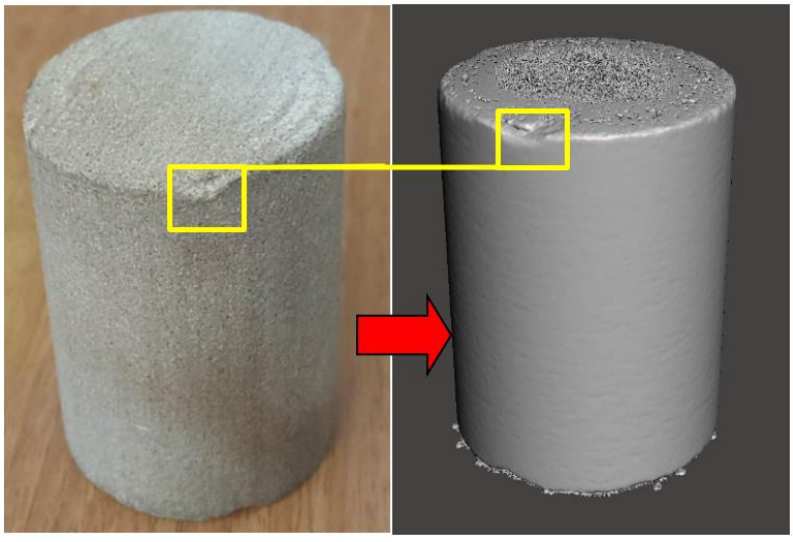

Figure 1.11: Outcome of the generated STL surface mesh file (RHS)

1.2 Conclusion

In this work, a novel workflow was developed to systematically combine CT scanning, image processing tools, and 3D printing technology in order to create synthetic core-plugs replicas for actual core-plugs (i.e. original Berea sandstone plug). This proposed workflow, unlike a number of similar works, replicates the actual pore network of the original core sample, and produces to-scale realistic 3D-printed core-plugs, which can be used for characterizing fluid flow and transport phenomena in laboratory experiments. The following summarizes the findings and conclusions of the study:

- Accurate 3D-printed replicas of a core sample can help us to understand the interactions among the porous environment and fluids in it under controlled conditions and known pore network structures in repeated experiments.
- 3D-printed core plugs are specifically useful in case of destructive tests are desired to conduct on a core sample. This will facilitate running repeated tests with the same pore network characteristics and preserve original cores.
- A major challenge for creating a synthetic core plug is accurate pore network modeling and pore throat characterization which can be addressed through accurate CT image processing.
- The proposed CT image processing workflow used to distinguish between pores and grains. Then, geostatistical and interpolation algorithms, developed in this work, will turn the discreet CT slices into continuous pore network. Next, the binarized volume of grains is converted to a solid mesh file in a format compatible with 3D-printers (i.e. *.stl format). Finally, synthetic core plugs can be generated using a 3D printer with desired materials (e.g. plastics, sandstone, etc. as printing powders).
- The results from this work confirm that using colored sandstone, rather than plastic, would produce more accurate representation of the original core characteristics (i.e. closer porosity and permeability to the original core's).

Finally, yet importantly, the 3D printing technology for replicating porous media is still in its infancy and the resolution of 3D printing machines needs to improve substantially to be used for core samples from tight rocks of unconventional reservoirs.

2 CT-Scan Image Processing for Accurate Pore Network Modeling and Core Samples 3D Printing

3D-printed core-plug replicas have wide applications in oil and gas industry. We can use synthetic plugs for repeatable set of experiments in which pore network geometry is accurately described for experiments' simulation purposes. We can also eliminate the complex effects of rock compositions on flow/transport characteristics. That will enhance our understanding for the physics of fluid flow processes in porous media. It is challenging to ensure that synthetic core-plug is accurately duplicating the original core-plug. The pore network accuracy in the 3D-printed replicas is controlled by the computed microtomography (CT) images resolution (both planar and longitudinal), 3D-printing file generation steps, and 3D-printer resolution limitations. We generated a robust workflow by combining CT scanning, image processing tools, and 3D-printing technology to create accurate synthetic replicas for core-plugs. Geostatistical tools (multi-azimuth variograms) and image processing tools (polynomial interpolation) were utilized to tune XY and Z resolution of a CT scan for Berea sandstone core-plug to fit current 3D-printing technology requirements, reduce the needed processing computational power, and construct a 3D-printable continuous volume. Based on the generated conceptual volume, 3D-printed sandstone replica was created and presented a close agreement with the petrophysical and transport behavior (porosity and permeability) of the original Berea core-plug.

3D printing of core plugs starts with processing a series of consecutive 2D grayscale CT images [16]. Each image has its array of specially defined attributes. These attributes include image number, height, width, minimum and maximum grayscale values, and the image data of each pixel (i.e. square picture element).

Next, adjusting and tuning the attributes of CT images to prepare the required optimal mesh file for creating 3D-printed synthetic porous core plugs and replicating the actual pore networks with identical petrophysical properties (porosity and permeability). The attributes of the CT images, which need to be tuned, enhanced, and tweaked in order to create accurate pore networks, include the CT image 2D width and height (i.e. number of pixels in each CT image), the number of images/slices along the core plug, and the grayscale of each pixel to distinguish between pores and grains. We discuss this process in details in this work.

The original XY resolution of a CT-scan image is highly dependent on the core sample size. For a small sample -1 inch in length or less-, a higher XY resolution can be obtained versus an average to low resolution for a relatively large sample –greater than 1 inch in length [16]. Even though, the CT images XY resolution (i.e. number of pixels in each CT image) still exceeds the possible resolution that can be handled by the current 3D printing technology. Another issue is the processing computational power needed to handle such high resolution. Therefore, we need to adjust the CT images width and/or height by reducing number of pixels in each image (Image Resampling).

Image resampling is a mathematical process in which a new version of the CT images with a different 2D dimensions-width and/or height is created [17]. There are two options in image resampling; a) up-sampling to increase the number of 2D pixels on each CT image (larger image size) and b) down-sampling to reduce the number of 2D pixels (smaller image size) [18].

In petroleum engineering terminology, the down-sampling of CT images is termed as upscaling. With the current 3D printing technologies and computer processing capabilities, first we need to conduct downsampling each of CT images (i.e. 2D upscaling). The downsampling/upscaling method can be conducted by a simple interpolation method.

The next step is up-sampling (i.e. increasing resolution) the upscaled 2D images in the Z direction (along core) and generate intermediate virtual images/slices between the original acquired CT slices. The reason of this treatment is to fill the gaps between the slices as the 3D-printer process only a continuous volume with no gaps in it.

The z-resolution of CT images, or the separation between two scanned planes, mainly depends on the core sample size, CT acquisition method, and CT scanner power [12]. A typical CT scan produces a limited number of images/slices (coarse z-resolution) for a (1 to 2) inch core sample.

The 3D printer requires a high number of slices to generate accurate representative porous replicas for the original core sample and to produce accurate pore network. Therefore, we utilized an interpolation scheme in Z direction to ensure a continuum in the data –pixels' grayscale values- and a smoother transition between (newly generated and original CT slices) data points.

The results of this procedure is a combined data of a virtual volume as a 3D cloud full of voxels' information which represents the entire scanned core sample volume. That continuous volume is ready to be meshed and 3D printed after applying a simplified particle recognition (grain/pore recognition) based on CT pixels' grayscale histogram [13].

A final step in the proposed workflow is to ensure that processing the CT scan gave a homogenous isotropic volume which can be 3D-printed without errors. The processed CT images are geostatistically analyzed to find their principal spatial variability attributes [19]. Multi-azimuth variograms are used as a quality control over the whole workflow by quantifying the homogeneity and isotropy parameters. This treatment step eliminates the need for an examining the processed CT slices on an image-by-image basis.

Finally, the generated virtual processed volume can be meshed for 3D-printing after examined it in all directions to avoid any open gaps. The output of meshing is a *.stl file (3D printing geometry file), which complies a collection of many triangles defined by their vertices and normal coordinates tracking the surfaces of the grains. 3D-printing of the synthetic core replicas is conducted layer by layer, horizontally, and from bottom to top.

The flowchart in **Figure 1** summarizes these steps, which are discussed below.

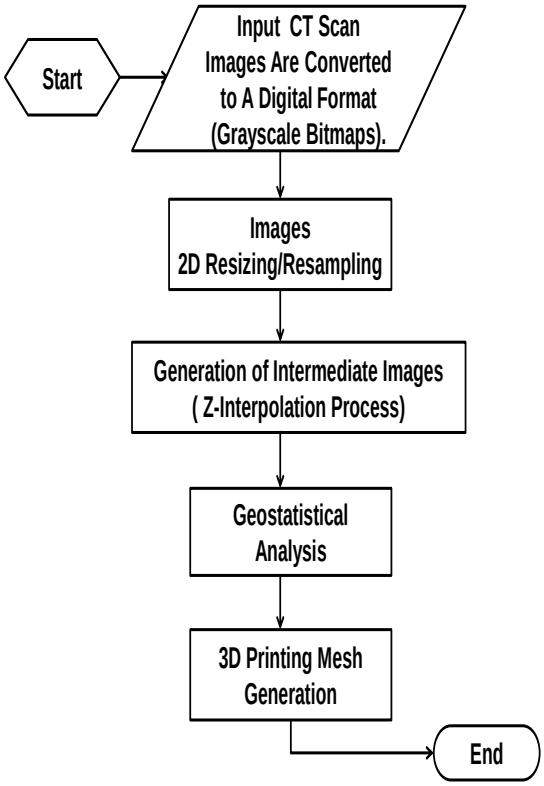

Figure 2.1: Workflow of generating a continuous virtual volume for synthetic porous core plugs using 3D-printing technology based on its CT scan

2.1 CT Imaging Technology

CT slices are the bitmaps of anatomical configuration for cross sectional scanned plane of the core sample. The core understudy in this work is a Berea sandstone core plug (2 inches long and 1.5 inches in diameter) with a porosity of 20% and a permeability of 100 mD (**Figure 2**). This is a well-sorted, conventional, and homogenous core sample. The pore throat diameters of the core sample, ranging from 50 to 150 μm, are beyond the limitations of current 3D printing technology and can be readily printed.

Figure 2 shows a series of selected CT slices along the core plug. The CT scanner consists of an X-ray beam source and a series of detectors mounted on the other side [10]. The X-ray beam attenuates through the core plug while passing through the object. The attenuation data are interpreted through back projection, which produces a CT image. The different colors on a CT image represents the intensity of such attenuations and different materials with different densities (voids, grains, minerals) [11].

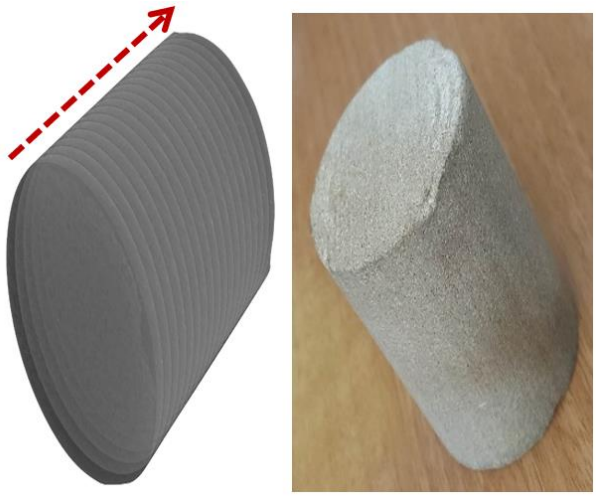

Figure 2.2: A series of selected CT slices (left) for the original Berea sandstone core plug (right)

It is an important task to adjust the CT scans resolution (i.e. the number of slices and spatial XY resolution). As mentioned above, this is a need to match the resolution requirements that can be processed by the available 3D printing technology. The XY-resolution is defined as the size of a pixel in the XY plane, typically 512 x 512 pixel/image [12]. 512 x 512 pixels cover the whole cross section of a core. To find the area that one-pixel cover, the ratio of number of pixels, in one image, in the X and Y direction to the dimensions of the core (1.5 inch in diameter) can be calculated.

On the other hand, the z-resolution, which is the separation between two consecutive slices of core plug, ranges typically from 0.1 to 1 mm. It can be calculated by dividing the core length (2 inch) over the number of the CT slices. In this work, 1000 CT slices were acquired along the core plug.

Figure 3 depicts a continuous volume required for 3D printing. It shows that the collection of a series of discrete 2D, CT images need to be processed first in order to create a whole object, which means to fill in the gaps between consecutive slices. Then, the 3D printer creates the synthetic object layer by layer and from bottom to top. The thickness between each two consecutive layers represents the maximum resolution we can get from the printer and that depends on the 3D-printer technology and the material used.

For each printed layer, 3D-printer generate a virtual horizontal plane to find the intersection contours with the virtual volume. These contours guide the nozzle of a 3D printer through the path on which the material will be released, meaning that the layer is constructed. The size of a nozzle varies from a machine to another and from material to material. The minimum spatial thickness of a 3D-printed point in space may not be greater than the thickness of the grains in a core sample. Therefore, a high number of CT scan pixels to cover the grain thickness (a high resolution) may not be necessary. This means that a thorough adjustment of the resolution on XY plane and along Z direction should be implemented to match the resolution of the machine used for 3D printing.

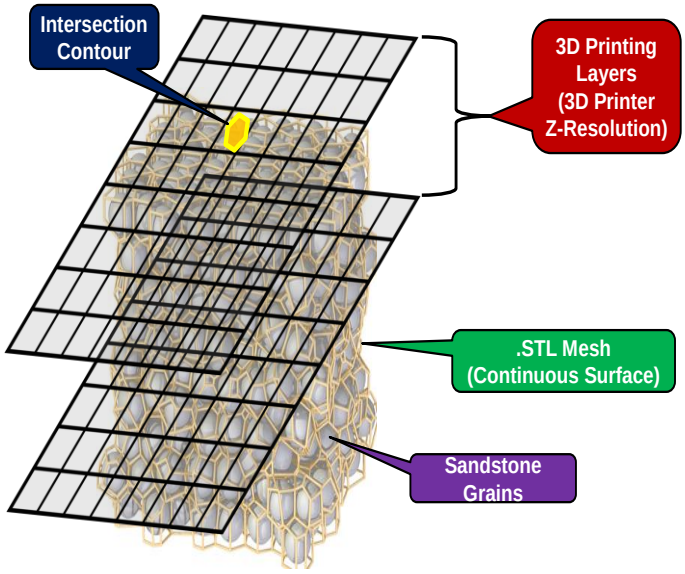

Figure 2.3: Tuning criteria for CT scan to fit the requirements of 3D-printing technology

2.2 CT-Image Resizing & Downsampling

The image downsampling reduces the XY-resolution of the 2D CT images. For instance, the original CT scan images in this study had a XY-resolution of 2084 x 2084 pixels, and it was upscaled (i.e. downsampled) 4 times, which resulted in a 512 x 512 resolution. The reason for that downsampling is that one pixel after downsampling covers an area of 0.05 mm by 0.05 mm, which is around the average pore throat size and grain size of a Berea sandstone sample. The appropriate upscaling level has to be determined manually. A rule of thumb should be considered which is the dimensions of a pixel should not be greater than the average grain size of a core sample. As shown in **Figure 3**, the average grain size of Berea sandstone ranges from 0.125 to 0.5 mm [8]. This rule of thumb guarantee one single grayscale value for a pixel is e a value for corresponding to a sandstone grain or a pore space.

The purpose of this step is to reduce computations effort for processing CT images and meshing the 3D conceptual volume later and by reducing number of redundant pixels. Contrast enhancement should be carefully considered at this stage as downsampling may result in loss of details on the created plug (jaggedness) since each upscaled pixel in the new processed image is a weighted average of multiple pixels.

A variety of interpolation functions for CT grayscale images have been developed in the literature. In each method, the discrete pixels' values to be resampled are initially mapped to create a continuous bicubic intensity function. The generated function with the fitting coefficients is used to match the new upscaled grid points and generate values for the new pixels as shown in **Figure 4.**

There are eight different methods of interpolation for the downsampling (upscaling) of an image, including: 1) windowed and truncated sinc; 2) nearest-neighbor; 3) linear; 4) quadratic; 5) bicubic; 6) cubic B-spline; g) Lagrange; and 7) Gaussian and 8) approximation techniques [20]. Lehmann [20] recommended the bicubic interpolation method, after comparing the 8 different interpolation methods,

to be the most suitable method for the downsampling (upscaling) of CT and MRI images due to its effective smoothing. The comparison was based on a detailed criteria of spatial analysis, computational complexity, runtime cost evaluations, and error analysis (qualitative and quantitative).

A bicubic interpolation method is a standard algorithm in commercial image processing software, such as Photoshop and Corel PaintShop [21]. It generates smooth polynomial spline functions of third degree on 2D planes (XY dimensions), taking into consideration sixteen adjacent points (see **Figure 4**) by finding the unknown coefficients of **Equation 1.** by regression. Then, function $f(x,y)$ will give us the values of new pixels. The bicubic function interpolation, in a discretized format for the 2D dimensions, is given by:

$$f(x,y)=\sum_{i=0}^{3}\sum_{j=0}^{3}a_{ij}x^{i}y^{j} \tag{2.1}$$

Where a_{ij} are unknown coefficients {i , j = 0 to 3 } to be obtained by regression.

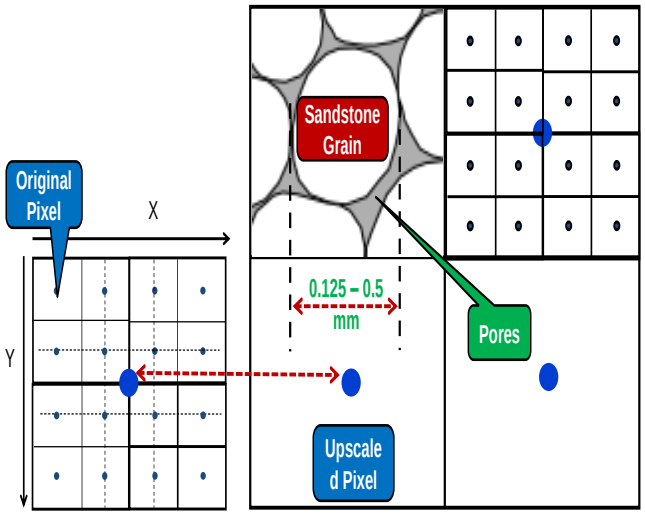

Figure 2.4: Bicubic interpolation downsampling is limited to the average grain and pore size.

Figure 5 depicts an example of downsampling one CT slice of from its original resolution to that of a quarter resolution. By implementing this method, a CT-scan data of 10 gigabytes data was compressed efficiently to almost 2 gigabytes of data without any negative impact on the quality of the images required for 3D printing process. In addition, as a result of downsampling it is easier for further enhancements.

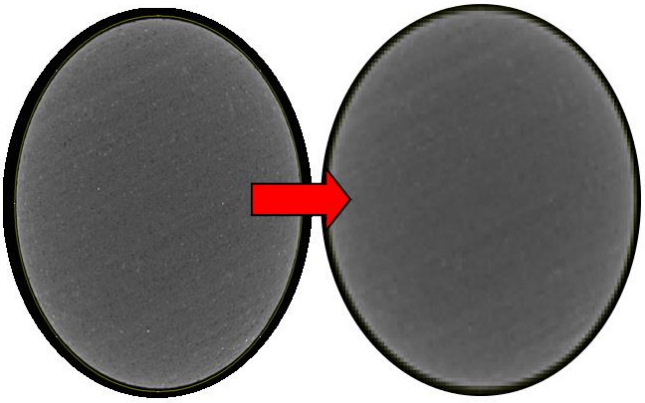

Figure 2.5: Downsampling of a CT-scan slice.

2.3 Interpolation of CT Images Along Z-Direction (Upsampling)

Rectangular voxels have a certain pitch (thickness) based on the sample size and the parameters of the CT scanner which determine the number of slices and their spacing. 3D-printer can process a certain layer thickness of a continuous volume -no gabs- (as it prints layer by layer). The 3D volume generated from the discrete CT images should be a whole (continuous) object resembling the actual pore network to ensure that the synthetically 3D printed core plugs represent the actual porous rocks. In this section, the optimal resampling along z direction for the acquired CT images to match such a requirement is discussed.

This means that we should generate a number of intermediate slices (virtual data) between consecutive images through proper interpolation methods. We have also the option to remove some slices from the original CT-scan set if they are more than the required number of slices to generate the continuous porous volume. Ideally, the spacing between two consecutive CT slices and 3D-printing thickness should not be greater than the average grain size. Therefore, the original CT number of slices are customized, decreased or increased by generating virtual intermediate slices, to enable the 3D-printer to distinguish and 3D-print the sandstone grains in one layer or more.

That being said, the 3D printing technology is developing with attention to reducing layer thickness (i.e. more CT slices will be needed), which will return better printing resolution in z direction. Interpolation techniques are typically used to generate the intermediate virtual slices along the z direction. Geostatistical tools (variograms and kriging) and artificial neural network (ANN) can be used also as an alternative for simple interpolation specially for heterogeneous core samples.

A CT image is a rectangular tiling of fundamental elements or pixels. A pixel (short for picture element) is a small block that represents the amount of gray intensity to be displayed for that particular portion of the rock sample. The pixel values on a CT image represents the material density distribution for that portion of rock. To fill in the gaps between the CT slices, there are eight methods to interpolate the grayscale pixel values as discussed above. In this work, a simple linear method was employed for the z-interpolation task. **Figure 6** depicts this process, and the computation is given by:

$$y = y_i + \frac{y_{i+1} - y_i}{x_{i+1} - x_i}(x - x_i) \tag{2.2}$$

Where (x_i, y_i) and (x_{i+1}, y_{i+1}) are the location and grayscale value of pixels in two consecutive slices, respectively.

The interpolation workflow starts with reading the grayscale values of each pixel on the two CT slices. Then, the in-between pixel values are estimated using a linear polynomial to construct the new slices with computed pixel values. This is repeated for all pixels and slices until a continuous 3D object are created. This constructed bank of data is ready to produce the mesh file (*.stl) to be used for 3D printing.

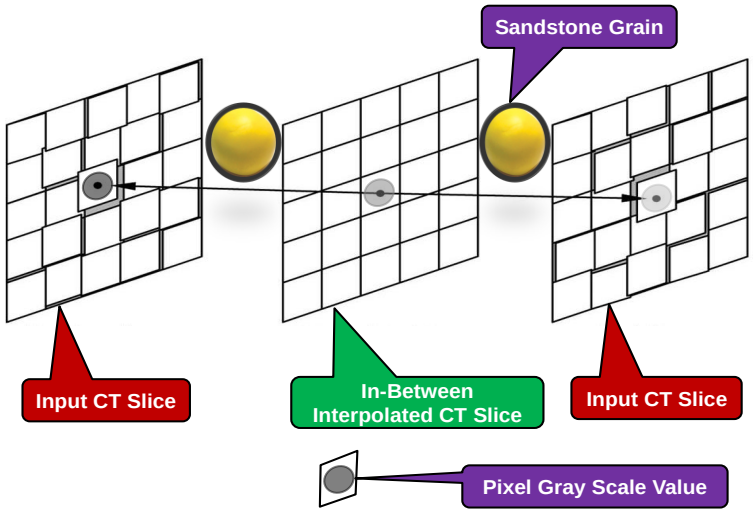

Figure 2.6: Generating CT scan intermediate slices

Figure 7 presents the pixels' value long a centered pixel through the core plug resulting from the linear interpolation of CT images (as an example, only the first 20 slices are shown). The grayscale values of intermediate slices are estimated from the straight-line interpolation between the two pixels. This procedure repeated for 512 pixels on the images. The linear interpolation technique is simple and straightforward, but as a drawback it may not be able to properly process heterogeneities, such as fissures and fractures (i.e. singularity problem). Cubic and nearest neighbor interpolation will be a better choice for heterogeneous cores. With the process developed in this work, we can also estimate other petrophysical properties, such as permeability and tortuosity, for core sample from its CT images.

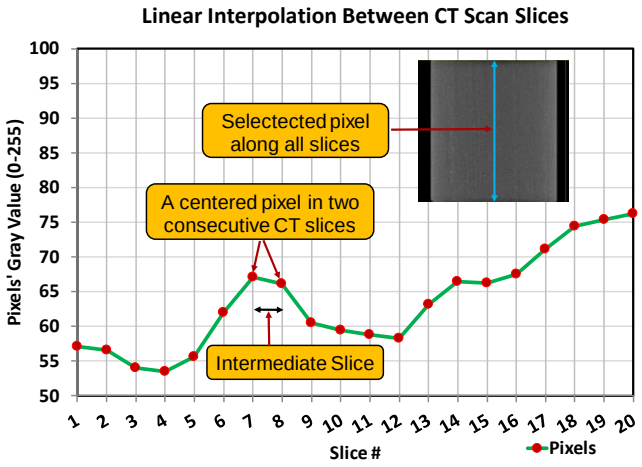

Figure 2.7: Linear interpolation to generate intermediate CT images from the original scanned slices

After applying this interpolation step, as shown in **Figure 8**, the output will be a set of continuous (lateral and longitudinal) orthogonal cross sections in which the sandstone grains and pores along the core plug can be tracked. This continuous cloud represents the continuous volume to be meshed and 3D-printed.

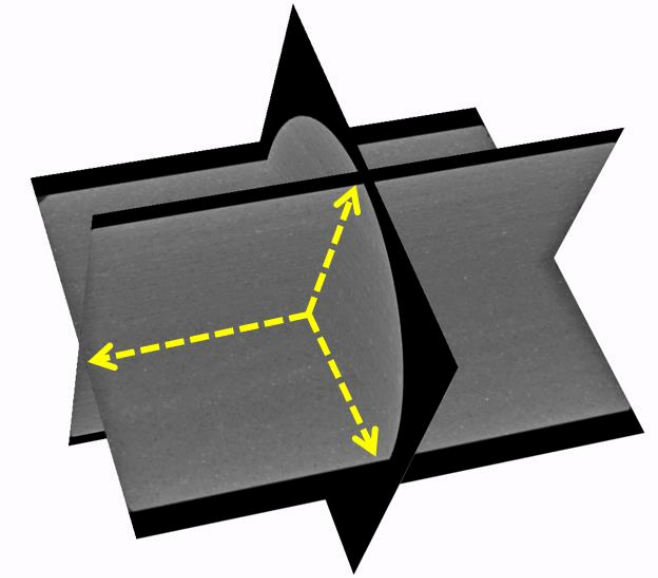

Figure 2.8: Continuous lateral and longitudinal slices after filling the gaps between the slices

2.4 Geostatistics Tools for Quality Control over Processed Reconstructed CT Conceptual Volume

Using the multi-azimuth variograms [19] in geostatistics, we analyzed the spatial variability of CT scan images in order to quantify their main characteristics, and check if the core sample is homogenous (quality control to check if it will be easy to process and to 3D-print). This helps us to better understand the core sample structure characteristics and avoid complexities/challenges of the current 3D printing technology. A variogram is the key function in geostatistics used to fit a spatial correlation model for

the observed phenomenon [22]. In this context, the observed phenomenon is the pixels' grayscale values of CT-scan images. It can be utilized to analyze the core characteristics through its CT-scan images [19]. Theoretically, a variogram is a function which analytically describes the degree of spatial dependence of a spatial random field; pixel values of a CT image. The variogram is the difference between the spatial variance of field values at two (s1 and s2) locations separated by distance h, in other wording, twice a semivariogram γ (h). The semivariogram was first introduced by Matheron [23] to be:

$$\gamma(h) = \frac{1}{2V} \iiint_{V} [f(M+h) - f(M)]^2 dV \tag{2.3}$$

where M is a location in the field V, and f (M) is the value at that location.

In this work, we used a commercial software (Petrel) to generate these multi-azimuth variograms for the processed CT-scan data. The scan date was uploaded to Petrel as a cloud data (x, y, z, and grayscale value for each pixel). 3D multi-azimuth variograms are basically 3 different variograms. One represents the major horizontal anisotropy and in its direction. Another is perpendicular to it, represents the minor horizontal anisotropy direction. The third is a vertical/longitudinal one. The main inferred parameters of a variogram include the type of variability (spherical, exponential, or Gaussian.), nugget (variogram jump at the origin), sill (variogram steady limit), range and anisotropy direction.

Analytical modeled variogram was fitted for the three experimental variograms of the acquired processed CT-scan data (grayscale pixels' values) of Berea core sample. The best spatial correlation modeled variogram to fit these data was found to be a Gaussian model with an isotropic spatial variability for the three directions.

Table 1 summarizes the results obtained from the three variograms with details as shown in **Figure 9**. The identical parameters for the major and minor variograms, small nuggets and ranges, and steady sills confirm the homogeneity and isotropy of the CT-scan data. Obviously, it is relatively easy to create synthetic core plugs (using current 3D printing technology) from homogenous and isotropic samples since there is no complexity in the core structure.

Table 2.1: The 3D variogram descriptive parameters

Variogram	Type	Sill	Range	Nugget
Major	Gaussian	0.5872	0.019	0.4128
Minor	Gaussian	0.5872	0.019	0.4128
Vertical	Gaussian	0.7893	0.05	0.6325

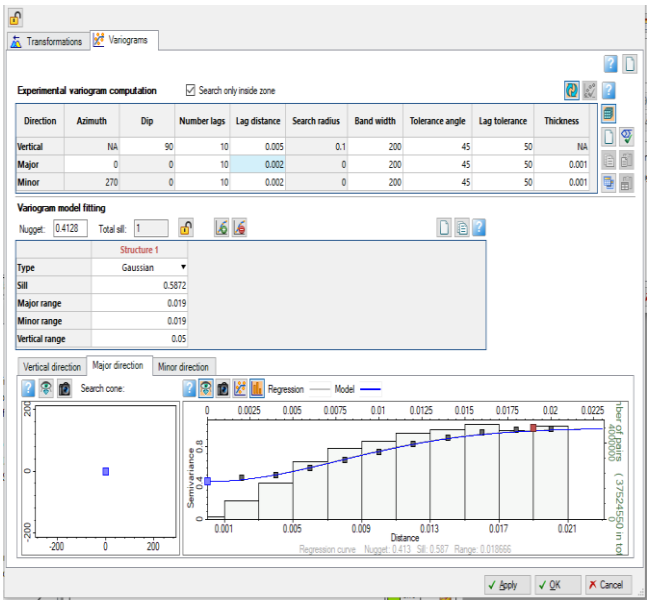

Figure 2.9: The 3D variogram generated for the CT-scan data, using a commercial simulator

A variogram map is also created for the processed CT-scan data. A shown in **Figure 10**, this map represents the variogram variability in any direction and at any distance from the core center. From this variogram map, the original core sample (from which the CT images are acquired) seems to be homogenous and isotropic since the iso-value contours are arranged as regular circles around the center.

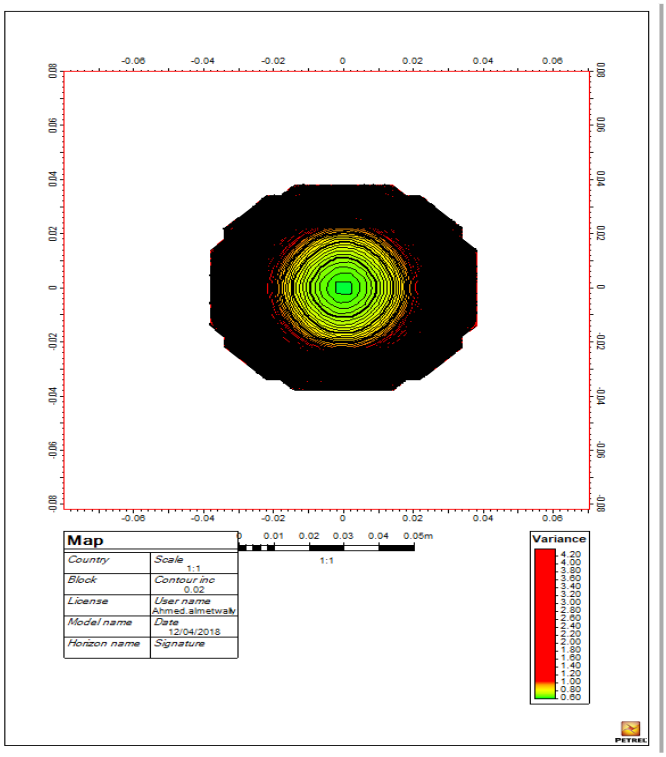

Figure 2.10: The variogram map generated for the processed CT-scan data, using a commercial simulator

It worth mentioning that analytical variogram along with a proper kriging technique can generate virtual data (intermediate slices) also and even be a better alternative for the usual interpolation tools but that will need a complex gridding to populate/allocate this data within it. The quality control over the CT-scan data can be conducted before applying image processing using interpolation algorithms or after it as proposed here.

2.5 Core Plug Replicas 3D Printing Process and Manual Segmentation Errors

Fabricating 3D printable objects need a thoroughly described geometry of their solid parts (grains in case of porous rock samples) to be 3D subsequently printed. After adjusting the lateral and longitudinal resolution of core's CT scan slices to match the 3D printing requirements, the workflow of 3D printing core replicas starts with segmenting the solid grains from the void pores [16][9]. The pores and grains are segmented based on their gray-value response using image processing [24]. Afterward, a binarized value is assigned to replace the grayscale voxels where the grains are spatially distinguished in the scan, i.e., one and zero for the pores. Finally, a triangular meshing algorithm is implemented to connect the processed one gray-value voxels in the scan to build continuous surfaces complying with the rock sample grains. The generated mesh file (stereolithography file) is conveyed to the 3D printer to fabricate the core replica. The technology of 3D printing itself is revolving with regards to object complexity and the resolution of the attainable details, and there are different printing materials suit various applications [25].

Segmentation is an image processing process in which pixels in CT scan slices are splitted to classes of objects based on similar attributes [26]. The segmentation accuracy controls the quality and resemblance of the replica to their original cores. Segmentation is challenging and aggravating when using a manual definite gray-value threshold to separate the pores from grains in the broad grayscale spectrum of the scan. Manual adjustment to the separation threshold cause overestimation for pore space and hence the sample porosity or vice versa. Figure 1 illustrates a continuous grayscale histogram for all pixels in the CT scan slices of the understudy Berea core sample. The continuous grayscale spectrum covers a range from 0 to 255 gray-value for pixels with two humps. The left hump is attributed to the pores and the right one to the grains' response in the sample scan. No distinct or a well-defined gray value can determine the right segmentation threshold. The selected threshold in Figure 1 represents an example of overestimating the pore space in the sample.

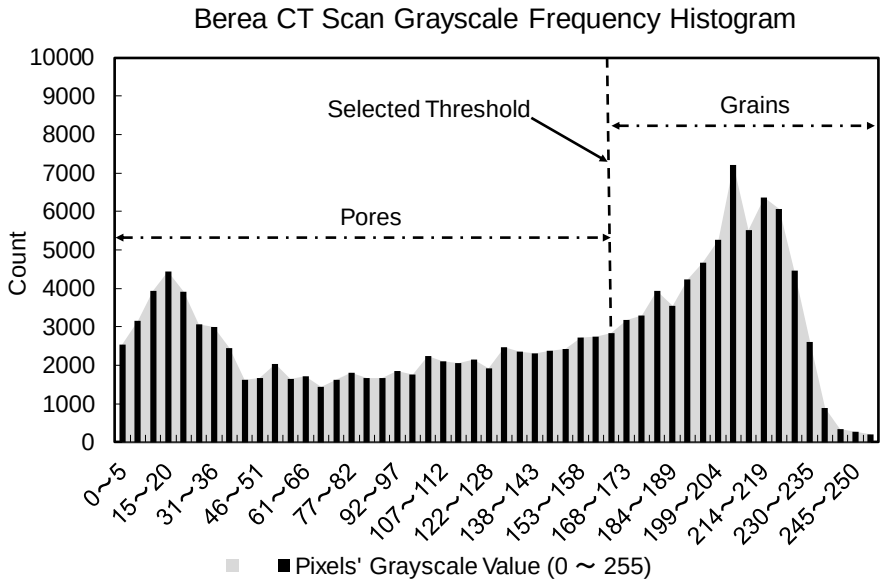

Figure 2.11: Grayscale histogram for all the CT scan slices of Berea core sample

Figure 2 explains the continuous gray spectrum in the scan without having a distinct threshold between grains' and pores' response. One single pixel can spatially cover a grain only (Pixel, P1), a pore only (Pixel, P3), or a combination of them (Pixel, P2). Pixel, P2, in Figure 2 does not belong to any of the two humps in Figure 1 and situates in between them as a constitute of the continuous middle interval. This pixel is a glaring example of manual segmentation errors and cannot be assigned to one binarized value (pore or grain). Consequently, we cannot implement object segmentation using pixels' gray intensity without any consideration for its physical representation or the continuity of the object [27].

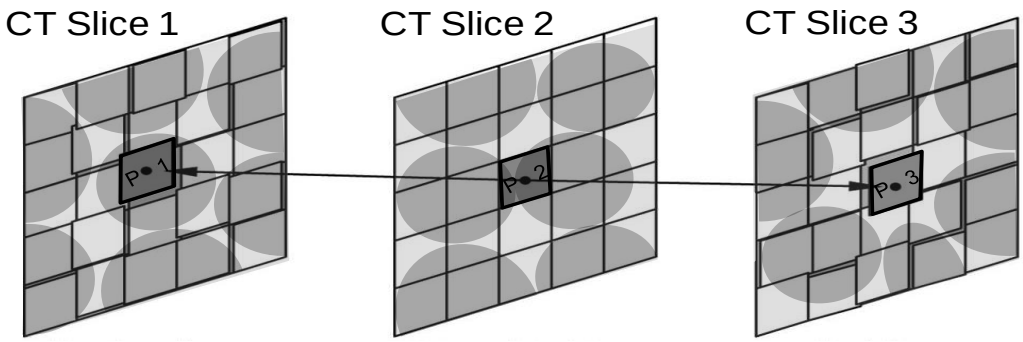

Figure 2.12: Manual segmentation error: Pixel, P1, is spatially representing a grain. P3 is spatially representing a pore. P2 is spatially representing a combination of a pore and a grain. P3 cannot be segmented correctly as a pore or a grain using manual segmentation.

2.6 Automated Machine Learning Morphological Segmentation

In a core sample CT scan, two structures of interest, e.g., pores and grains, must be detected for accurate 3D printing. Pores and grains segmentation can be considered as a classification and clustering machine learning problem. As a solution to overcome manual segmentation errors, an MLIPT was used to data-

mine the sample's CT scan for segmentation using automated trainable search for grains [28][29]. The MLIPT workflow is presented in Figure 3. MLIPT will track the two features in a training set of slices based on their gray intensity, texture/grain, and pore morphology, edge detection, location, etc…. A set of pixels is selected and labeled to be in one class (Pores or Grains) in the training set. Another set of pixels is assigned to the second class or feature. Once MLIPT classifier is trained, it can go through the rest of the CT scan slices.

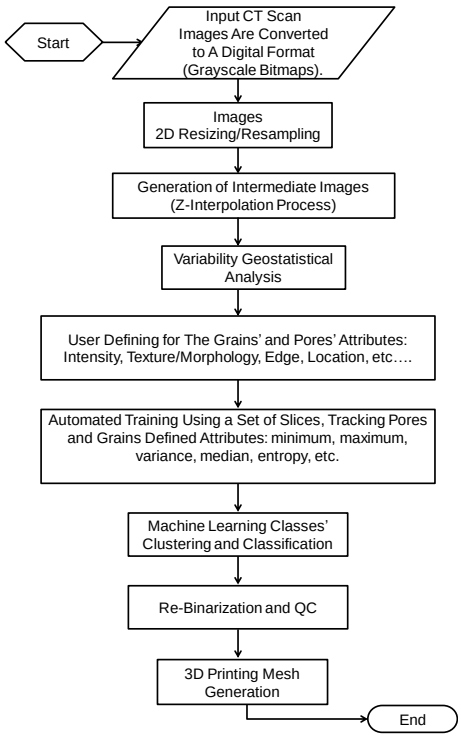

Figure 2.13: Automated machine learning morphological segmentation workflow for 3D printing of core samples replicas

MLIPT detects objects (pores and grains) by tracking their statistical attributes. Assuming MLIPT is trained intentionally that a grain covers four neighbor pixels. MLIPT will calculate the minimum, maximum, variance, median, entropy, etc. of their gray values. Then it will start tracking similar attributes in the rest of the slices' pixels [30]. Finally, MLIPT will localize and similar pixels with the same attributes and cluster them in one group and proceed to repeat the same steps for other classes. The training criterion is an initial manual delineation for grain and pore's group of pixels. Then, the tool follows that criteria geostatistically. The training data was 45 CT slices, selected randomly. The segmentation quality was judged by the quality of the simulation results in section 6, with a confidence training quality of 95%. Figure 4 shows a training slice a grayscale CT scan for the understudy Berea core sample (1 inch in diameter) with a resolution of 1024×1024 pixels. The middle picture is prepared by a manual segmentation threshold of 170 gray-value, as in Figure 1. White spots represent pores, and black ones are assigned for grains. All pixels in the original scan have a gray value from 0 to 170 will be classified as pores. That wide range (from 0 to 170) explains the high intensity of pores in the segmented picture, which gave a porosity of 30%. The right-hand image is the MLIPT output after training classes and classification then clustering the scan. The calculated porosity based on white pixels' intensity to the slice area was 20.01%, which matches the measured porosity of the Berea sample.

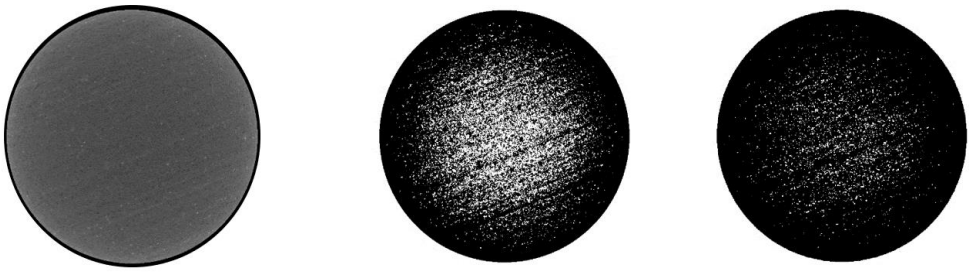

Figure 2.14: Manual threshold segmentation versus automated machine learning morphological segmentation

2.7 Results of Volume reconstruction

The continuity of a modeled 3D object from a series of 2D discrete CT images is essential for 3D printing. Using geostatistics and interpolation algorithms, we developed a workflow for adjusting the 3D resolution of the CT images; on XY spatial plane and along Z- longitudinal direction. The discrete CT slices were then successfully converted to a continuous volume as shown in **Figure 11**. Next, the methodology proposed by Almetwally (Almetwally and Jabbari, 2019), was used to 3D-print synthetic core plugs, using gypsum/sandstone. Finally, the petrophysical properties of the synthetic plug replica were measured and compare with the original core properties (see **Table 2**). The results show the synthetic sandstone plug represents acceptable petrophysical behavior compared to the original Berea core sample.

Table 2.2: Petrophysical properties for original and printed cores

	Porosity (%)	Permeability (mD)
Original core	20	100
Printing SS	22	110

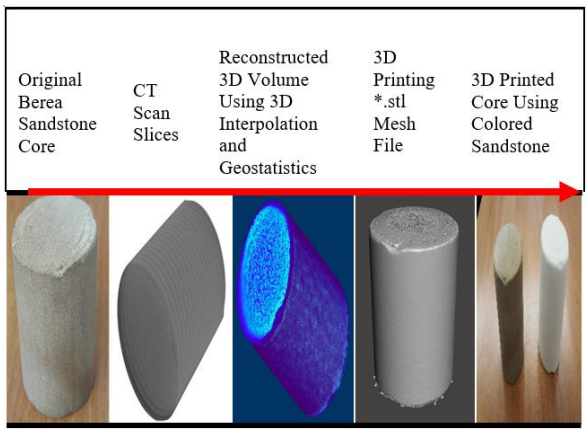

Figure 2.15: Workflow of generating synthetic core plugs from the original core sample (Berea sandstone)

2.8 3D PRINTING

The next step of the workflow is 3D printing the surface mesh geometry. A 3D printer does the reverse of what we do in preparing a surface mesh file. It starts to slice the generated continuous volumetric surface to layers. Then, it uses the printing material (plastics, sandstone, etc.) to follow the solid intersections between the horizontal plane and the input volumetric geometry and repeat layer by layer from bottom to top. Parameters like layer thickness and printing speed are determined based on the best fit for the object, the printing material, and the printing technology.

In this work, we have tested the proposed workflow of generating representative 3D-printed core plugs with print materials, such as common plastic (PLA), polylactic acid, acrylonitrile butadiene styrene (ABS), and colored sandstone as shown in **Figure 12**. In addition to close resemblance of printed cores to the original cores, the petrophysical properties of the 3D printed core plugs were then measured (using porosimeter and gas permeameter) to test the accuracy of the proposed method and the reliability of the produced synthetic core plugs. In fact, the porosity and permeability can reflect the storativity and connectivity of the porous system. Table 1 summarizes the results of these measurements.

Table 2.3: Petrophysical properties for original and printed cores

	Porosity (%)	Permeability (mD)
Original core	20	100
Printing SS	22	110
ABS	15	60
PLA	25	70

The permeability measurements were conducted based on Darcy's Law and by using gas. As the permeability data in **Table 1** shows, the colored-sandstone synthetic core (using gypsum powder as printing material) shows a similar hydraulic behavior (close permeability) to that of the original core. The issue in printing with plastics, which resulted in very low permeabilities, is that the material would have been melted during the printing.

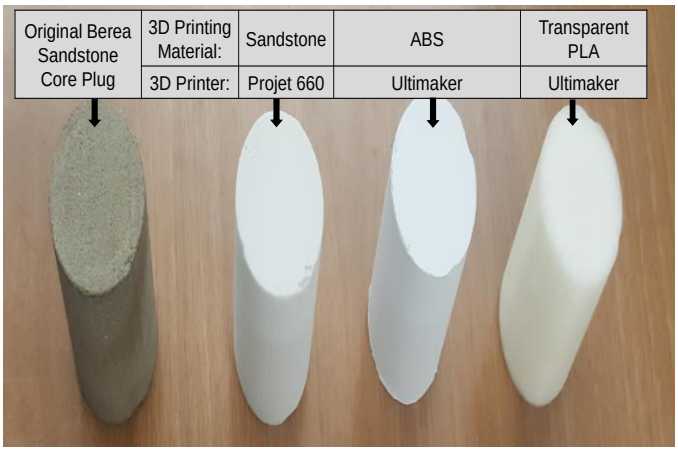

Figure 2.16: Synthetic 3D-printed core plugs with different printing materials; plastics (ABS and PLA), colored printing sandstone, and original Berea core

2.9 Conclusions

In this work, a general workflow is developed to customize the planar (XY) and longitudinal (Z) resolution of CT images to serve the requirements of current technologies of 3D printers for synthetic core plug creation and the computer processing capabilities required for that. Image processing tools; i.e. polynomial interpolation, and geostatistics tools for quality control; i.e. multi-azimuth variograms, are successfully used for this customization and construction of porous replicas for the original core. The static storage capacity; porosity, and hydraulic transport capacity; permeability, of the created replicas are compared with the original core sample capacities and the following summarizes the findings and conclusions of this study:

- A robust workflow was developed to use the bicubic and linear interpolation to tune the CT-image attributes, and to use geostatistics for quality control (QC) the image data.
- A methodology for reducing the XY-resolution was introduced by using the cubic interpolation to reduce unnecessary planar details (upscaling/downsampling). This procedure bases the pixel generation on pore/grain size and the limitations of the 3D printing machine, which is essential for creating representative pore networks of the original core sample.
- Linear interpolation was implemented to generate intermediate slices between consecutive CT images, and to create continuous 3D conceptual volume to be used for mesh generation files (i.e. filling in the gaps between discrete CT slices).
- Geostatistics, through variograms, was utilized to examine the spatial variability of the final volume obtained from CT-image interpolation to ensure the isotropy and homogeneity before 3D printing the core sample final processed mesh file.
- Following the proposed methodology in this work, we can generate porous 3D-printed core replicas, which can represent the pore network and petrophysical/transport properties (porosity and permeability) of original core samples.

3 Experimental Investigation of 3D Printed Rock Samples Replicas

Laboratory Experiments on rock specimens are designed for understanding and characterizing subsurface environment, quantifying potential recovery, and tuning fluid flow models in porous media. The spatial variability and reservoirs' heterogeneities predicate acquiring expensive cores from different locations. These experiments are mechanically and petrophysically destructive and cannot be repeated or extended on the same core. Replicating core samples with 3D-printing technology innovation alleviates the acquiring cost of rock samples and enables experiments repeatability and extension. This paper explains the workflow of creating accurate 3D printed core samples replicas using a machine learning image processing tool (MLIPT) based on natural cores' CT scans. In addition to that, an extensive experimental investigation was conducted to check the veracity of the similarities between the natural samples and their 3D printed replicas. This comprehensive investigation showed that 3D printed rock-sample replicas are accurate, inexpensive, and adaptable specimens for laboratory research in the oil and gas sector.

Rock mineralogy heterogeneity in oil and gas reservoirs causes many uncertainties accompanying the petrophysical properties population to the whole reservoir models. These uncertainties embed accurate petrophysical characterization of rock and fluid interactions and hence the quality of numerical and analytical reservoir models. The number of acquired core plugs for laboratory experiments determines the quality of a reservoir model. Geomechanics and fluid flow experiments destroy these cores and alter their nature; therefore, researchers have to use other cores to extend or repeat their experiments. Different cores have different mineralogy and pore network configuration even if they are acquired from the same well, formation, and with the same orientation. Pore network geometrical uncertainties also are geostatistically challenging in analytical or numerical modeling validation for any experimental work [31]. The geometrical uncertainties complicate modeling interpretation of laboratory results. Experimental results from different cores will be changed and lack consistency.

Upstream oil and gas industry research focuses on better understanding and characterizing fluid-rock interactions to enhance recovery. Subsurface is a complex system with a great deal of heterogeneity and anisotropy at all scales. Over-simplified Fluid flow physics failed to characterize and describe such a complex system accurately. Reducing fluid-rock characterization uncertainties using 3D printing is beneficial to fundamental research aspects of experimental and modeling efforts in oil and gas research. 3D printed replicas of core plugs can eliminate those uncertainties [16]. Their spatially invariable chemical composition compels rock-fluid interaction to be accurately quantifiable [9]. In addition to that, usage of the same geometry file in creating replicas and modeling experiments leads to precise and close results to its original core if compared to extended modeling of experiments on different natural cores from the same well.

Advances in 3D bio-fabrication of custom living tissues boosted the geometrical preciseness of 3D printing technology using micro to nanomaterials with inert chemical and stable mechanical properties [32]. The replicas preciseness in the experimental research is attributed to a well-described pore network geometry and the uniformity of the printing material composition. This paper explains the workflow of creating accurate 3D printed core samples replicas using a machine learning image processing tool

(MLIPT) based on natural cores' CT scan. The workflow succeeded in tailoring the physical dimensions of the samples according to the needs of the experiment setup. An extensive experimental investigation was also conducted to check the veracity of the similarities between the natural samples and their 3D printed replicas. The experiments were gas porosity and permeability, Nitrogen sorption, MICP (Mercury Injection Capillary Pressure), huff-and-puff CO_2, and contact angle wettability measurement. Finally, a simulation model was built using the MLIPT pore network for the MICP experiment and compared with the experimental results.

3.1 3D Printing Berea Replicas

Commercial Berea sandstone core sample of 1 inch in diameter and of 1 inch in length is used as a reference sample. Berea sandstone is well-sorted, angular, and fine quartz sandstone. Its grain composition is mostly Quartz, around 87 to 93% [7]. The measured gas porosity for it was around 20% and gas permeability of 100 mD. Figure 5 shows Berea reconstructed 3D volume and the generated stereolithography mesh file (*.stl mesh file) after following the workflow presented in Figure 3. 3D printing technology and used printing material affect the printing preciseness. 3D printer limitation resolution on object details and printing material characteristics cause printing errors. Berea core sample was replicated with different materials and 3D printers, as shown in Figure 6. By measuring the petrophysical properties of the replicas (porosity and permeability), It was concluded that Gypsum-based replica is more precise with 22% porosity and 110 mD permeability. A gypsum-based replica was 3D printed with Gypsum-based powder called "VisiJet_PXL with ColorBond" [33]. The used binding chemical was "Instant-cure_ColorBond Infiltrant" [34]. The 3D printer was ProJetx60 series, which uses the technology of selective deposition to build the 3D printing layers [35].

3.1.1 3D Printing Berea Replica and Samples Preparation

A Berea sandstone core sample was CT-scanned to be a base for 3D printing and CO_2 huff-n-puff testing [7]. The used core was 1.5 inches in diameter and of 2 inches in length. Its measured porosity was around 20% and its gas permeability of 100 mD. The 3D interpolation workflow was followed to adjust the CT scan resolution to match the 3D printing resolution requirements [9]. Image processing tools were utilized to segment pores and grains voxels based on the gray-value response in the scan [16]. The processed grains/solid points are triangulated to construct the 3D printable volume. The generated stereolithography mesh file is conveyed to a ProJetx60 series 3D printer to fabricate the core replica [35]. The ProJetx60 printer uses gypsum-based powder, called "VisiJet_PXL," and a binding chemical, called "Instant-cure_ColorBond Infiltrant" which is Acrylic thermoplastic resin-based, for fabricating its objects [33] [34]. The created replica had a measured 22% gas porosity and 110 mD gas permeability. **Figure 4** shows the steps of 3D printing the gypsum-replica starting from CT-scanning its original Berea core sample.

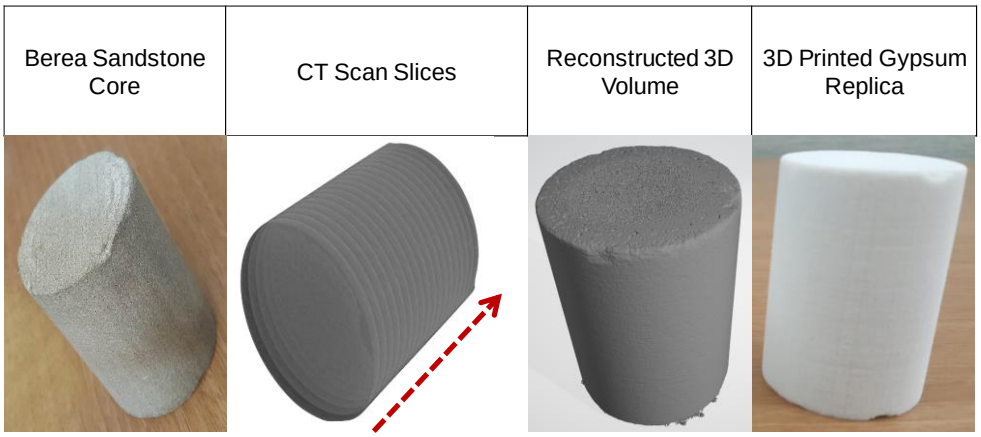

Figure 3.1: 3D printing the CT-scanned Berea sandstone core sample after reconstructing its volume using image processing

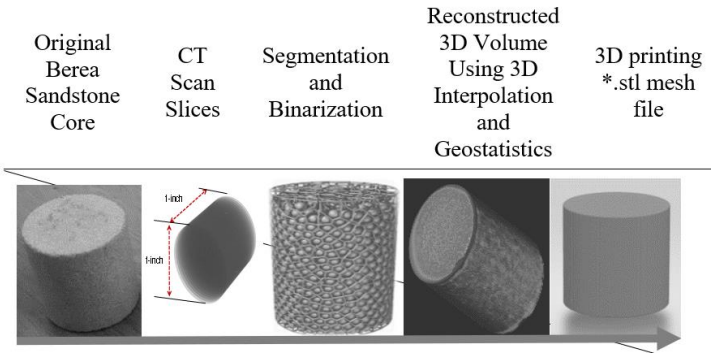

Figure 3.2: Automated machine learning morphological segmentation workflow for 3D printing of core samples replicas

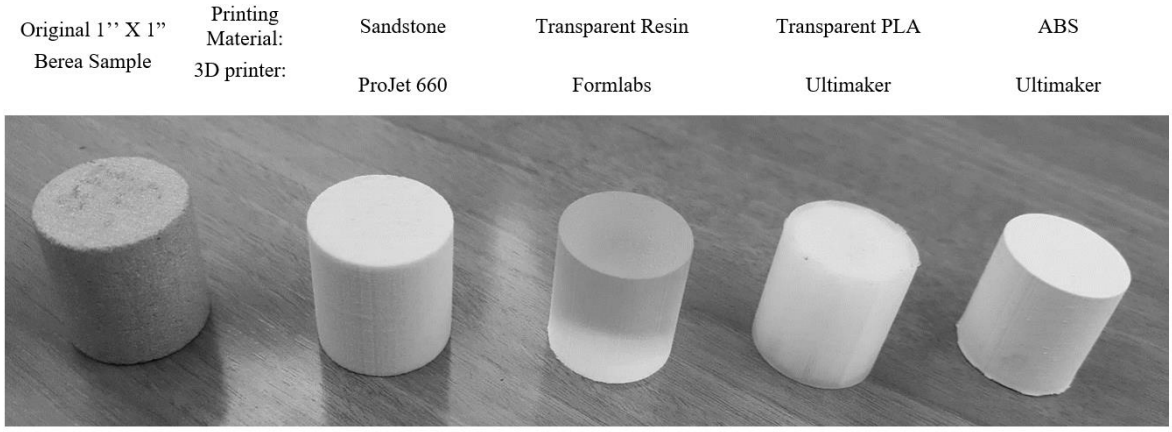

Figure 3.3: Berea core sample with its replicas created using Gypsum, Resin, PLA, ABS 3D printing material and different 3D printers

3.2 Experimental Investigation

Laboratory experiments are conducted on core samples to determine their petrophysical properties. The veracity of 3D printed replicas to be used in oil and gas research should be supported with a similarity in petrophysical properties with their natural rock samples. Therefore, the focus of this paper will be on experiments conducted under the same operating conditions on both the Berea core sample and its replica. The similarity criteria will be the fluid content within the pores and fluid transmissibility through the core. The quantification of rock-related fundamental parameters like porosity, grains surface area, and pore size distribution, and contact angle wettability is the rubric for these criteria through the next four experiments. Even the oil recovery from the CO_2 huff-n-puff experiment is estimated on both samples to support the premise [36].

3.2.1 Nitrogen Adsorption - Desorption Experiment

Measuring porosity and evaluating grains' texture are essential in understanding oil and gas reservoirs and their performance characteristics. Samples with the same physical dimensions perform differently if they have differences in grains' texture and porosity. A physical adsorption/desorption experiment can accurately determine these properties. Nitrogen sorption (adsorption-desorption) is a technique used to characterize the surface and pore features of core samples [37]. Attributes about specimen texture, include pore volume distribution by pore size, surface area, and total pore volume, can be quantified by this experiment from the sample's free space measurements.

Nitrogen sorption measurements were performed with a Micromeritics 3Flex surface analyzer [38]. It uses static volumetric physical adsorption technology [39]. Figure 7 explains the schematic of the static volumetric physical adsorption experiment. The experiment starts by the degassing (cleaning and preparation) process. For that purpose, using either evacuation or an inert gas purge or heating can help to remove the weakly adsorbed molecules. Samples' free space measurements (porosity, pore-volume, surface area, …) in gas sorption experiment are typical gas-phase volume measurements. Gas-phase behavior in this experiment is controlled by pressure, available volume, and temperature of the system. The apparatus has an empty reference tube for calibration and another tube to accommodate the sample. Nitrogen in the coolant area evaporates, and its level changes with time. A static level control system is used to keep Nitrogen effectively going up through a wick around the reference tube [40]. The control system will ensure keeping the level in the reference tube fixed with minimal changes through the experiment. The fixed nitrogen level keeps the start and end conditions of the experiment alike. Contrarily, the Nitrogen level in the sample's tube is monitored for estimating the amount of adsorbed gas to the sample at different relative pressures. Relative pressure is calculated by dividing liquid Nitrogen pressure in the sample's tube to the saturation pressure of liquid Nitrogen.

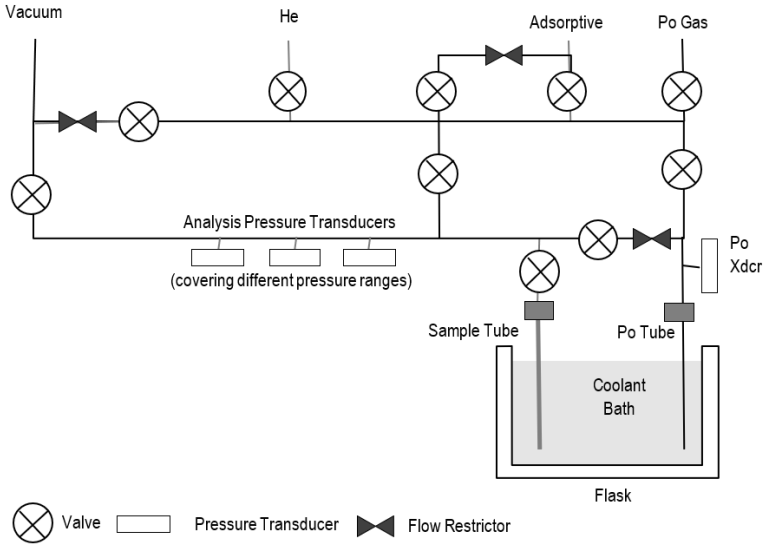

Figure 3.4: Nitrogen adsorption-desorption experimental setup using static volumetric physical adsorption technology (courtesy of Micrometrics) [38]

The experiment is typically performed at Nitrogen liquefaction temperature. The adsorbed and desorbed quantity of Nitrogen molecules can be estimated from level changes during the experiment in the sample's tube. These quantities are plotted versus relative pressure to generate exclusive adsorption and desorption isotherms to the understudy sample [41]. Figure 8 and Figure 9 compare the generated isotherms for both the Berea sample and its replica. The two isotherms resemblance can strengthen the hypothesis of the potential of using 3D printed replicas in laboratory research experiments. It can also be a good indicator to judge the used segmentation algorithms to prepare the replica itself.

Understanding the physical sorption phases can explain the different isotherm slopes at different pressures. The earliest adsorption phase, monolayer adsorption, happens once Nitrogen molecules encounter the sample surface, and it gets attracted to grain's surface by intrinsic surface energy (attraction forces between Nitrogen molecules and solid ions) and bound momentarily to that surface. The second phase, multilayer adsorption, starts with increasing pressure as the number of molecules hitting the surface increases and correspondingly the adsorbed quantity. By applying more pressure, multiple layers of Nitrogen molecules on a sample's grains are created. This process continues until, ultimately, pores are filled and grains' surface is completely covered (pore filling phase). The adsorption energy is minimal; thus, adsorbed molecules can be easily removed/desorbed by decreasing the pressure or by increasing the temperature (desorption phase). Each adsorption phase has its characteristics and follows different analysis models, e.g., early monolayer phase follows Langmuir linear equation. There are six types of adsorption isotherms associated with different textures of solids, according to Brunauer–Emmett–Teller (BET) classification [42]. Both samples surprisingly showed exact adsorption isotherm type; "Type II" [43]. Both of them did not show any hysteresis between the adsorption and desorption branches. Isotherms don't reveal hysteresis effect when samples have relatively large pores.

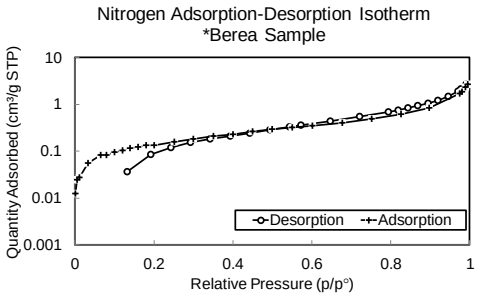

Figure 3.5: Nitrogen Adsorption-Desorption isotherms for Berea core sample

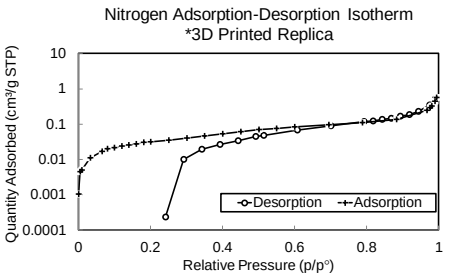

Figure 3.6: Nitrogen Adsorption-Desorption isotherms for the Gypsum replica

3.2.1.1 Mono-layer Adsorption Analysis: Specific Area Using Langmuir Adsorption Model

Early adsorption linear data points belong to the monolayer origination phase around the grains [44]. That part of the data fits a linear model called Langmuir adsorption isotherm [45]. Equation 1 conveys the Langmuir model, demonstrating that the adsorbed Nitrogen quantity reciprocal (1/ q_a) is following a linear relationship with pressure [37].

$$\frac{p}{q_a} = \frac{1}{q_m b} + \frac{p}{q_m} \tag{3.1}$$

Where P is the equilibrium pressure in mmHg, q_a is the quantity of adsorbed gas at a specific pressure in cm^3/g STP, q_m is the quantity of gas required to produce a monolayer in cm^3/g STP, and b is Langmuir model constant in 1/mmHg. Figure 10 and Figure 11 shows a linear graph of (p/ q_a) versus p for both samples. The linear relationship slope is used to estimate q_m, and Y-intercept is used to determine Langmuir constant; b. Berea sample has a larger estimated monolayer adsorbent quantity, q_m, or a gentle Langmuir model slope compared to its replica steep slope. The explanation for that is referred to as sandstone grains larger surface area compared to the 3D printing gypsum power grains surface area.

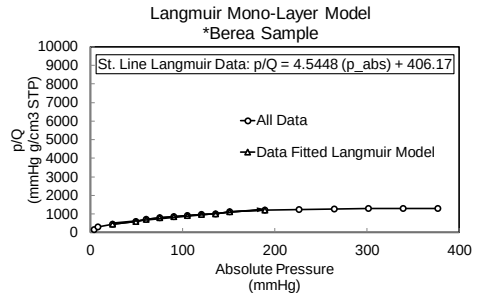

Figure 3.7: Langmuir surface area analysis for the Berea core sample

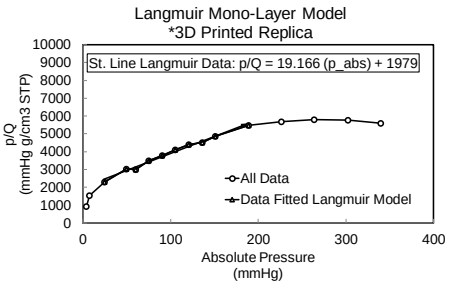

Figure 3.8: Langmuir surface area analysis for the Gypsum replica

3.2.1.2 Multi-layer Adsorption Analysis: Specific Area Using BET Adsorption Model

Multi-layer phase data points have a horizontal plateau after the linear mono-layer data. Brunauer–Emmett–Teller (BET) model is widely used to describe the extended mono-layer interval to the multi-layer portion [46]. Equation 2 is presenting the linearized form of the BET model.

$$\frac{1}{q_a((\frac{p^0}{P})-1)} = \frac{1}{q_m C} + \frac{C-1}{q_m C} p/p^0 \tag{3.2}$$

C is a dimensionless constant associated with the adsorption energy between the adsorbent layers and the sample. Adsorption isotherm data, which conforms to the BET model, is used in a linear plot between the left-hand side of Equation 2 and relative pressure (p/p^0) to estimate q_m and C. Surface area can be determined from that plat with low relative pressures (below value of 0.4) [47]. Figure 12 and Figure 13 show the fitted BET model for both samples. The BET model plot is consistent with the Langmuir model about estimating a larger mono-layer adsorbent quantity, q_m, for Berea.

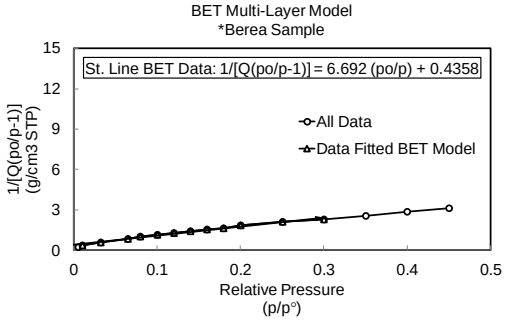

Figure 3.9: BET surface area analysis for the Berea core sample

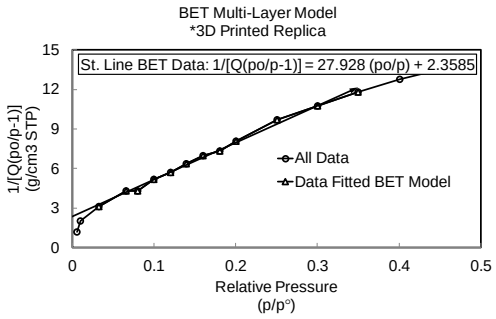

Figure 3.10: BET surface area analysis for the Gypsum replica

Grains' specific surface area, in (m^2/g), can be estimated using q_m for both models (Langmuir and BET) using Equation 3 [45].

$$\text{Specific Surface Area} = \frac{q_m \, \sigma \, N_a}{m} \tag{3.3}$$

Where σ is the area occupied by each molecule in the case of Nitrogen at liquid Nitrogen temperature, the molecular area equals 0.162 nm^2/molecule for Nitrogen, N_a is Avogadro's number or 6.0221415×10^{23} molecule/mole, and m is the molar mass of Nitrogen (m^3/mol). Table 1 shows the Langmuir and BET calculated specific surface areas for both samples.

3.2.1.3 Filled Pores Adsorption Analysis: External Area Using t-plot

The pore space, which can be filled after the multi-layer phase, whereas micro-pores have already filled by the adsorption, are larger pores like meso-, macro- pores, or grains' exterior surface. The further isotherm data after the plateau of the multi-layer formation phase contribute to larger pore space-filling. The t-Plot method is developed by Lippens and De Boer to quantify this external area. Simply, it is a linear plot of adsorbed quantity (q_a) versus the estimated layer thickness (t) around the grains. The thickness t is calculated by Harkins and Jura equation (Equation 4) [48][49].

$$t = [\,13.99 / (\,0.034 - log(P/Po)\,)\,]\,\hat{}\,0.5 \tag{3.4}$$

The t-Plot linear range lies between the mono-layer phase data and the capillary condensation phase. t-plot linear slope, q_a/t, is equal to that external area of the grains per one gram. Figure 14 and Figure 15 show the resulted t-plot for both samples. The results of the t-plot analysis are appended to Table 1. Negative results for both samples confirm that both samples have pores of the same micro-scale. No larger size pores in the samples are present.

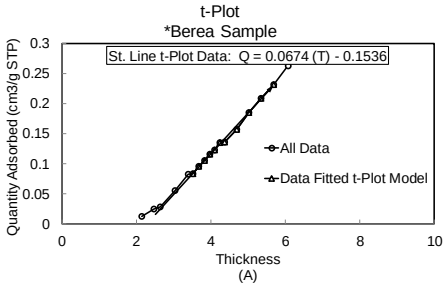

Figure 3.11: External Area estimation using t-plot analysis for Berea core sample

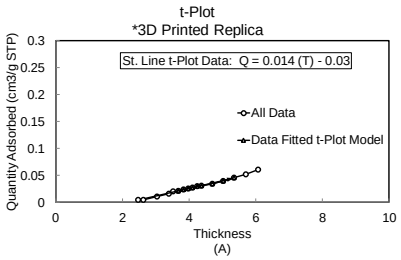

Figure 3.12: External Area estimation using t-plot analysis for the Gypsum replica

3.2.1.4 Pore Volume Estimation

Porosity determination needs both full adsorption and desorption isotherm data to determine the flip point. The pores should be filled with Nitrogen, not only a layer or multiple layers. The last few points of the adsorption isotherm represent the pores being filled. The total pore volume and hence the porosity of the sample can be estimated by converting the final cumulative adsorbed quantity to the total pore volume by applying Gurvitch rule (Equation 5) [50].

$$Total\ Pore\ Volume = \frac{34.67\ ml_{liquid}}{mol_{gal}} q_{aTotal} \tag{3.5}$$

Where $\frac{34.67\ ml_{liquid}}{mol_{gal}} = \frac{1.5468\ x\ 10^{-3} ml_{liquid}}{cm^3_{gal}}$ The calculation results of pore volume reported in Table 1 show a higher pore volume of Berea, which confirms the presence of non-connected pores in the 3D printed replica. The remaining binding materials block these non-connected pores.

3.2.2 Pore Volume and Surface Area Distribution Using BJH Equation

The final adsorption phase is the capillary condensation, which happens after all pores are filled with Nitrogen. For this phase, pore volume distribution ($d(V_p)/d(d_p)$, cm^3/ g nm) or surface area distribution ($d(S)/d(d_p)$, m^2/g nm) can be correlated with pores' radius distribution as proposed by Barrett, Joyner, and Halenda (BJH) [51]. The cylindrical pore radius (r_p) is modeled as a function of the adsorbed layer thickness (t) and relative pressure, as given by the Kelvin capillary condensation equation (Equation 6). q_a can be tabulated against r_p using this equation. For the capillary condensation phase, this tabulation represents the nitrogen amount to fill all the pores by condensation. BJH proposed that the derivative of this relationship ($d\,q_a/d\,r_p$) can give the pore volume distribution.

$$r_p = t - 4.5/log(P/Po) \tag{3.6}$$

Pore volume, as mentioned in the previous section, is estimated from q_a, and by assuming cylindrical pore radii. The BJH surface area distribution and the cumulative surface area are calculated as in Equation 7 and Equation 8. Finally, The average diameter can be calculated from the surface area and pore volume for cylindrical pore radii using Equation 9 [51].

$$S = 2V_p/r_p \tag{3.7}$$

$$S_{cum} = 2\sum V_p / \sum r_p \tag{3.8}$$

$$d_{av} = 4V_p/S \tag{3.9}$$

Figure 16 (left and right) and Figure 17 (left and right) show pore and surface area distribution by BJH adsorption and desorption respectively method for both samples. The results of BJH analysis are appended to Table 1. The distribution characteristics and the trends for both samples are the same but with different intensities considering the smaller Gypsum grain size.

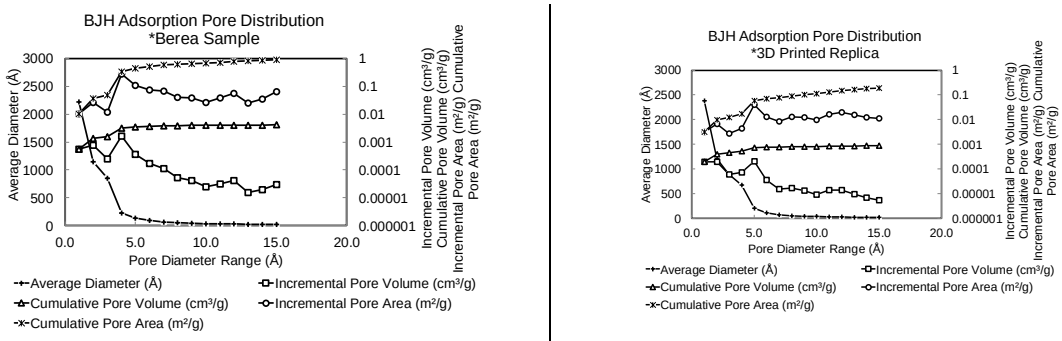

Figure 3.13: Pore volume and surface area distribution estimation using BJH analysis for adsorption data of Berea core sample and its Gypsum replica

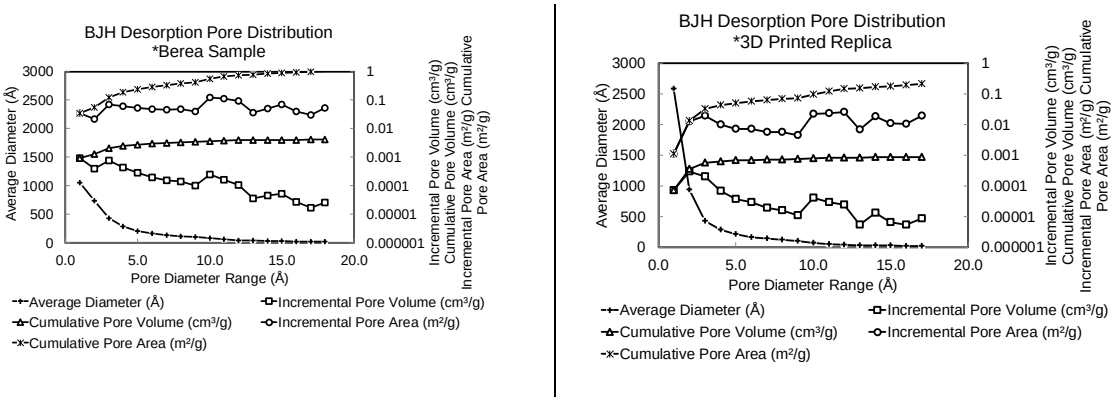

Figure 3.14: Pore volume and surface area distribution estimation using BJH analysis for desorption data of Berea core sample and its Gypsum replica

The samples' texture (Specific Area, External Area, Pore Volume and Surface Area Distribution, and Porosity) is fully quantified using Nitrogen adsorption, and the differences between the original Berea core sample and its replica are presented in Table 1.

Table 3.1: Nitrogen Adsorption-Desorption Isotherms Analysis

	Berea Core Sample	3D Printed Replica
Surface Area		
Langmuir/Single point surface area at P/Po = 0.300423811:	0.9578 m^2/g	0.2271 m^2/g
BET Surface Area:	0.6107 m^2/g	0.1437 m^2/g
t-Plot Surface Area:	(-ve) m^2/g	(-ve) m^2/g
Pore Volume		
Single point desorption total pore volume of pores less than 1,934.646 Å diameter at P/Po = 0.990000000:	0.004104 cm^3/g	0.000872 cm^3/g
Pore Size		
Desorption average pore diameter (4V/A by BET):	260.2191 Å	224.7210

3.2.3 CO2 Huff and Puff Experiment

Figure 18 shows the dry Berea core sample and its gypsum 3D printed replica. Both samples were saturated for one day with crude Bakken oil after being vacuumed [52]. The purity of the Gypsum replica enhances the clarity of the oil saturation effect on the core sample as shown in Figure 19. The samples were soaked for 6 hours in a core flooding holder at three different CO_2 injection pressures of 800, 1200, and 3500 psi, and under different temperatures of 70, 120, and 220 °F. CO_2 was injected as a gas, immiscible liquid/gas, and in a miscible super-critical phase. The oil recovery was estimated by calculating the weight difference between samples before and after each CO_2 injection cycle. Another used method to determine the oil recovery was by measuring the recovered oil weight.

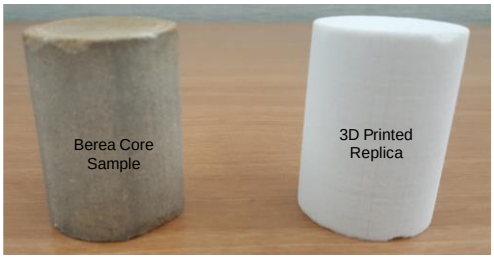

Figure 3.15: Dry Berea core sample and its gypsum replica

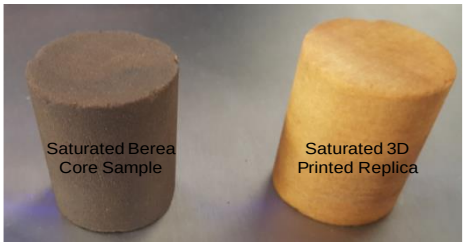

Figure 3.16: Saturated Berea core sample and its gypsum replica

Figure 20 to Figure 22 show the samples after each cycle of CO_2 injection. It is noticeable the clarity of the CO_2 effect on the 3D printed replica. The 3D printed sample has no impurities in its material, which eliminates deviation in the expected recovery results with CO_2. 3D printed cores showed its effectiveness as an ideal choice for experimental work because we can generate as many synthetic core samples as we want at a low cost. Therefore, we afford to destroy a core replica and break it along a

lateral and longitudinal plane as shown in Figure 23 and Figure 3.21 (left and right). Observing the interior of the cores after the CO_2 injection helps us to physically and visually check the effect of CO_2 on oil recovery inside the core. We cannot break a real core sample as it is expensive to acquire another core with close characteristics, but with 3D printed cores, we can do that and continue the experiment on another similar replica.

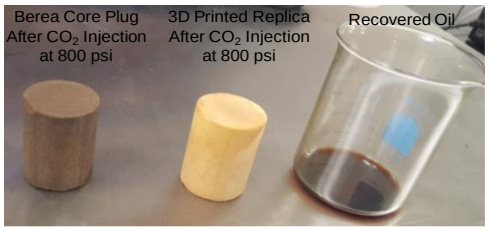

Figure 3.17: Samples after CO_2 injection at 800 psi

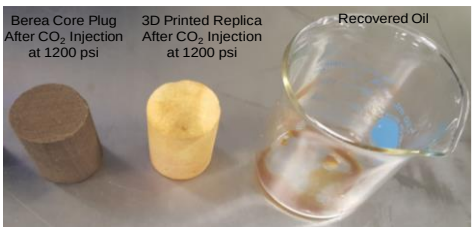

Figure 3.18: Samples after CO_2 injection at 1200 psi

Figure 3.19: Samples after CO_2 injection at 3500 psi

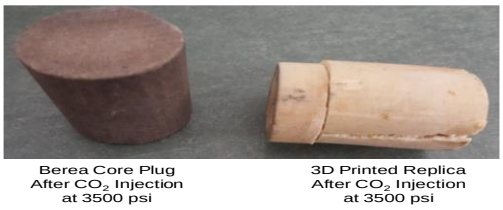

Figure 3.20: Lateral and longitudinal breaking for the 3D printed core sample to check the effect of CO_2

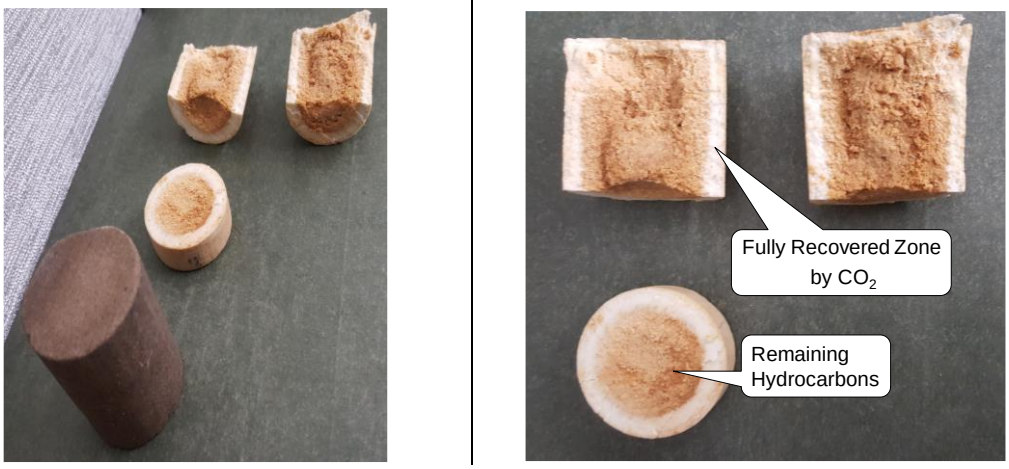

Figure 3.21: CO_2 huff and puff injection effect on the 3D printed core sample

Figure 25 and Figure 26 provide a comparison between oil recovery from Berea and synthetic core samples. A notable result was that temperature affected, to some extent, the recovery from the synthetic replica compared to its original Berea sample. The temperature profoundly affects oil properties, e.g., oil viscosity and interfacial tension, but, in the presence of material impurities, that effect will be diminished. Another explanation for that phenomenon is the removal of the blocked binding materials with temperature, which increases the connectivity between pores and hence the recovery. It is also noted that the maximum recovery form the 3D printed core sample has reached about 80% after 3500 psi but 60% for the Berea sample.

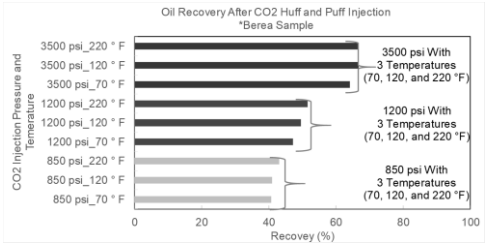

Figure 3.22: Berea core sample oil recovery after CO_2 huff and puff injection

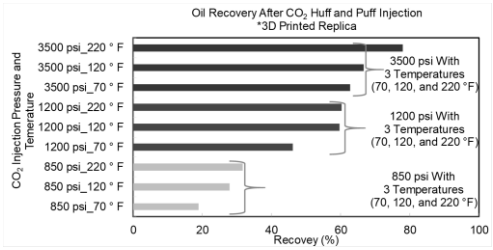

Figure 3.23: Synthetic 3D printed replica core sample oil recovery after CO_2 huff and puff injection

3.2.4 **Contact Angle Wettability Experiment**

The state of wettability dictates the amount of recovery as a response to CO_2 injection. Therefore, after each CO_2 injection cycle, wettability chips were used to measure the contact angle wettability. The contact angle wettability measurements were conducted using a high-resolution ramé-hart camera integrated with a high-pressure sample chamber and illumination system [53]. The sample chips, as shown in Figure 27**,** were used to reflect the core material's response to the exposure to CO_2. Figure 28 and Figure 29 show that CO_2 has altered the wettability of the 3D printed replica from intermediate to strongly water-wet and very repulsive to oil. On the other hand, the wettability of the Berea sample did not change drastically for the cases before and after CO_2 injection. Core sample mineralogy plays a significant role in determining the recovery response from the sample. The3D-printed chip surface repulsion to oil minimizes the rock/fluid interaction, which is ideal for studying fluid flow and transport phenomena in porous media. That is considered as a beneficial outcome since generating valid analytical and numerical models for fluid flow in porous media requires idealized porous media with a minimum number of factors or uncertain parameters. Therefore, synthetic core samples created from CT scans and image processing with uniform composition and known pore network can be robust, accurate, affordable, and, most importantly, a time-saving replacement for actual and repetitive core sampling from a formation.

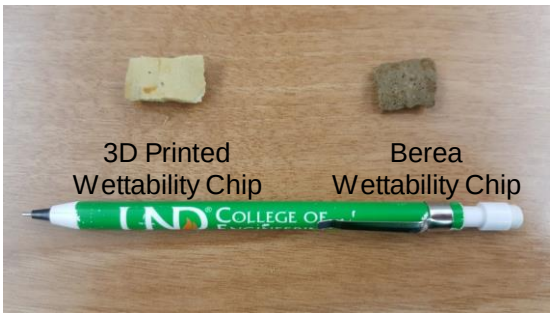

Figure 3.24: Wettability chips from Berea sample and its gypsum replica

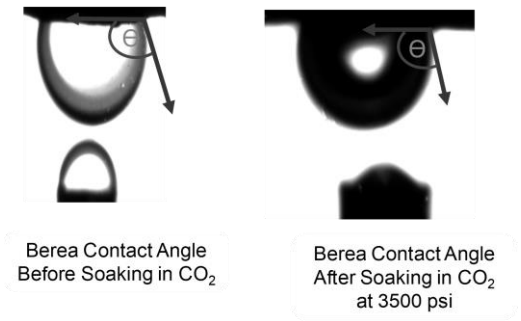

Figure 3.25: Examples from wettability measurement for Berea before and after soaking in CO_2

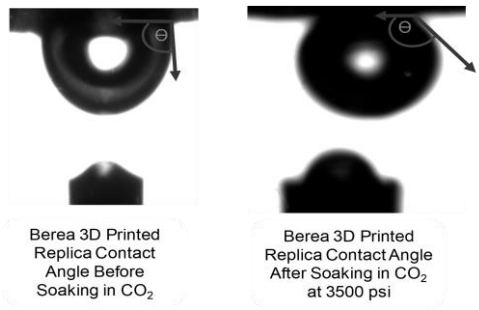

Figure 3.26: Examples from wettability measurement for Berea 3D printed replica before and after soaking in CO_2

3.2.5 Mercury Injection Capillary Pressure (MICP) Experiment

Mercury porosimetry is an experimental technique from which we can infer information about pore sizes, pore volumes, and pores' areas within a solid sample [54]. With some additional analysis, the technique can also be used to calculate bulk density, skeletal density, and porosity, and it can even be extended to measure permeability, pore tortuosity, and sample compressibility [55]. We used 60,000 psi AutoPore IV Mercury Porosimeter from Micromeritics [56]. AutoPore IV 9520 can cover the pore diameter range from 360 to 0.003 µm. It has four low-pressure sample ports and two high-pressure chambers. Figure 30 demonstrates the MICP experiment schematic. The pressure is implemented to force mercury to intrude on the sample pores. The volume of intruded Mercury, and hence Mercury saturation, is reported versus a wide range of applied pressures. By increasing the applied pressure in appropriate increments, we can generate an intrusion curve or MICP capillary pressure curve of Mercury intrusion pressure against water saturation (complementary of Mercury saturation).

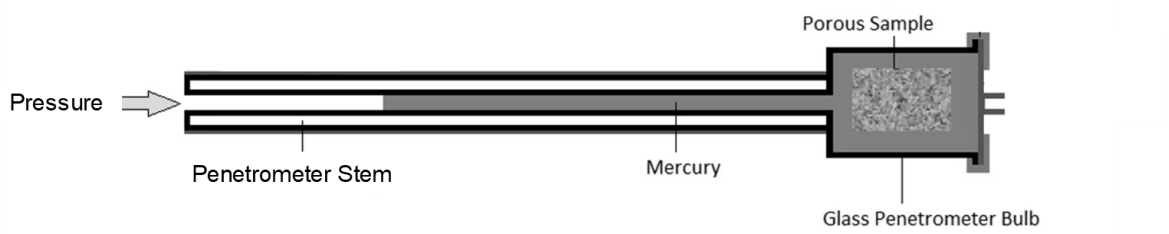

Figure 3.27: Mercury injection capillary pressure (MICP) experiment schematic

The American society for testing and materials published the procedure of MICP experimental testing as a standard protocol [57]. In that protocol, intrusion volume is correlated with the remaining mercury volume in the penetrometer stem, which is measured by electrical capacitance changes. Figure 31 and Figure 32 illustrate the difference between MICP capillary curve for Berea and its replica. That difference is referred to the difference in pore size distribution between the two samples. High intrusion pressures are noted for the replica, which confirms the presence of non-connected pores.

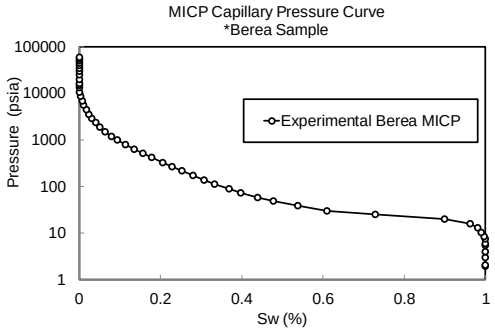

Figure 3.28: MICP capillary pressure curve for Berea sandstone sample

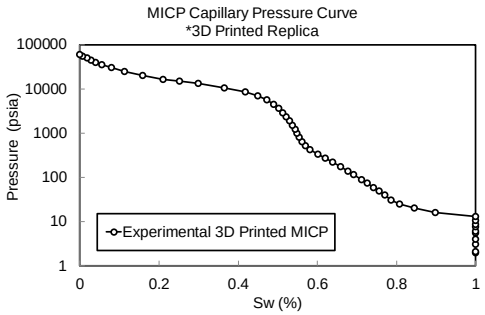

Figure 3.29: MICP capillary pressure curve for the Gypsum replica

MICP pore size distribution is another sample characteristic which can be inferred from the experiment. Because Mercury is a non-wetting fluid to most materials and has a high surface tension, its contact angle and curvature radius are used to convert the intrusion pressure to the corresponding pore diameter by applying Washburn's equation (Equation 10) [58]. In that equation, the required pressure to intrude mercury into a pore is inversely proportional to the size of the pore.

$$D = 2\gamma \cos\theta / P \tag{3.10}$$

Where D is the pore diameter in microns, γ is the surface tension of mercury (485 dynes/cm), θ is the contact angle of mercury (130°), and P is the applied pressure in psi. By knowing the contact angle and the surface tension of mercury, precise control, and measure for the applied pressure can be used to calculate the corresponding pore sizes after loading the sample into a MICP penetrator. Figure 33 and Figure 34 show the resulted pore size distribution for Berea and its replica. IUPAC set ranges of macro-, meso- and micropores, which are greater the 50 microns for macropores, from 2 to 50 microns for mesopores, and less than 2 microns for micropores [7]. Berea sample had an incremental intrusion volume peak around a diameter of 10 microns. On the other hand, not only the replica showed the same diameter, which confirms the quality of 3D printing but also showed another peak of 0.01 micron of the non-connected pores. These non-connected pores are intruded, in the crushed sample, at higher pressures and increase the estimated MICP porosity for the sample.

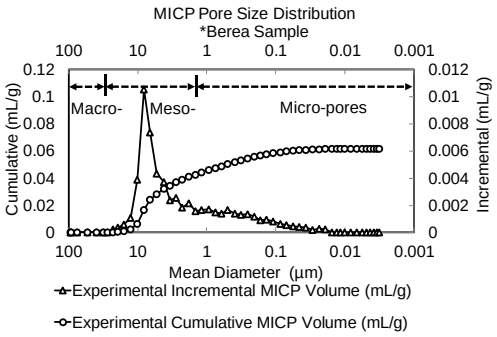

Figure 3.30: MICP capillary pressure curve for Berea sandstone sample

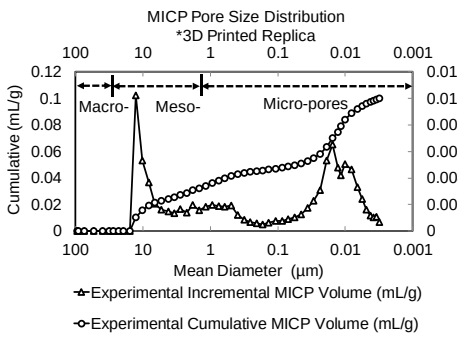

Figure 3.31: MICP capillary pressure curve for Gypsum replica sample

Sample bulk density can be calculated by weighting the sample after low-pressure MICP run using Equation 11.[55]

$$\rho_b = \frac{W_s}{V_p - \left(\frac{W_a - W_p - W_s}{\rho_{HG}}\right) - C_v} \tag{3.11}$$

Where ρ_b (g/cm^3) is the bulk density, W_s is the sample weight in g, V_p is the penetrometer volume in cm^3, W_a is the apparatus with the sample weight in g, W_p is the empty penetrometer weight in g, ρ_{Hg} is mercury density in g/cm3, and C_v is the conformance volume in cm^3. Ultimately, porosity is calculated once the mercury injection has concluded at a high MICP pressure of around 60,000 psi using Equation 12 [55].

$$\Phi = \left(PV_{Hg} - C_v\right) * \frac{\rho_b}{W_s} \tag{3.12}$$

Where PV_{Hg} is the total injected mercury volume at 60,000 psi in mL or cm^3. Additionally, the skeletal/grain density (ρ_g) in g/cm^3 can be calculated as a function of bulk volume (BV_{Hg}) in cm^3 as in Equation 13 [55].

$$\rho_g = \frac{W_s}{(BV_{Hg} - PV_{Hg})} \quad where\ BV_{Hg} = \frac{W_s}{\rho_b} \tag{3.13}$$

The MICP results are tabulated in Table 2 for both samples (Berea and its replica). The results confirm that the 3D printed replica has a higher porosity because of the non-connected pores. Contrarily, less replica porosity, in the Nitrogen sorption experiment, is referred to the low-pressure range of Nitrogen intrusion.

Table 3.2: MICP Results

		Berea Core Sample	3D Printed Replica
Total Intrusion Volume =	mL/g	0.0635	0.1886
Total Pore Area =	m²/g	0.528	20.835
Median Pore Diameter (Volume) =	µm	4.2201	12.6677
Median Pore Diameter (Area) =	µm	0.0784	0.0080
Average Pore Diameter (4V/A) =	µm	0.4805	0.0362
Bulk Density at 1.93 psia =	g/mL	2.2524	1.5218
Apparent (skeletal) Density at 59972.16 psia =	g/mL	2.6281	2.1344
Porosity =	%	14.2973	28.6984
Stem Volume Used =	%	32	28

3.3 Conclusion

The following can summarize the outcomes of this work:

- 3D printed rock-samples replicas can represent the original pore network of core samples for hydrocarbon recovery experiments. Under the conditions of known geometry (pore network) and wettability (core material) of 3D printed replicas, there are a few factors and uncertainties which may affect the CO_2/oil/rock interactions.
- For 3D printing core samples, the most used method in pores/grains segmentation and building pore network models is manual segmentation. Simulation and experimental investigation showed that manual segmentation of CT scans might fail to mimic the original core sample responses. The reason is attributed to the indistinctive assignment of pixels in the scan to their corresponding pore and grains.
- In this work, an automated machine learning segmentation algorithm was utilized to create a virtual 3D printable object from a CT scan of a Berea core sample to replicate the original sample accurately.
- Nitrogen adsorption-desorption experiment was used to compare the actual physical texture of the Berea core sample and its created gypsum replica, including surface area, pore-volume, pore throats, and their distributions. Different isotherm phases, e.g., linear Langumiar, BET multi-layer, and capillary condensation, were analyzed to reflect the pore texture for both samples.
- MICP experiment was conducted to infer information about pore size distribution, pore volumes, and pores' areas for both samples.
- Digital rock physics software was used to simulate the MICP experiments with two different segmentation algorithms. The comparison showed that the automated machine learning segmentation could produce 3D-printed core replicas and pore network models effectively compared to manual segmentation.
- CO_2 huff-and-puff experiment was conducted on the Berea core sample and its replica. Even though both samples had similar porosity and permeability, the recoveries were different, which explained by the impact of different core material on CO_2-medium interactions. The complicated mineralogy of the natural core sample (Berea) reduced the oil recovery while the 3D printed replica presented higher recovery due to its uniform gypsum-powder material. 3D printed replicas also proved their ability to withstand very high experimental pressures and temperatures.
- The maximum CO_2 oil-recovery occurred above miscibility pressure and at the highest temperature. The purity of the 3D printed replica enhances the effect of CO_2 injection pressure and temperature on the recovery process, which referred to replicas' strong water wettability. By using the 3D printed core samples, we were able to visually examine the interior of the samples to study the impact of CO_2 from a huff-n-puff process.
- Gypsum replica's wettability, as measured in the lab, was found to be strongly water-wet and had a repulsive surface to hydrocarbon, which makes it an ideal choice for experimental research if minimal interactions between rock and hydrocarbon (low residual oil saturation; S_{or}) are desired.

4 Numerical Simulation Based on a Reconstructed CT Scan

Numerical simulation and experimental research of fluid flow in porous media enhance the practices of petroleum reservoirs' management. Experiments on acquired reservoir-rock samples are conducted for accurate characterization and realization of the insitu hydrocarbon reserves. Implementing precise numerical simulation of those experiments is crucial to acquire accurate conclusions from the obtained experimental results. Coreflooding experiments quantify reservoir rock's storage capacity, measure its transport connectivity, and evaluate recovery methods' effectiveness for that rock. In this paper, a reconstruction image-processing workflow of cores' CT scan is developed to build a finite difference numerical model for simulating coreflooding experiments. In a transient coreflooding experiment, a controlled pressure pulse with a known frequency and amplitude is transmitted to the rock sample. Rock permeability can be quantified by analytically solving the diffusivity flow equation for that experiment. Simulating the transient permeability experiment is very sensitive to the level of details of the pores' structure described in the numerical model. A transient permeability experiment with two different transient modes, sinusoidal oscillation, and pulse decay, was conducted on a standard Berea core sample. The Berea CT scan was image-processed to reconstruct the static porosity and permeability model in Petrel software using a 3D variogram geostatistical population. Injection and production sources were assigned to the finite gridblock, which correspond to flow nozzles of injection and production coreflooding setup's heads. Scheduled flow and controlled-pressure boundary-conditions were imposed on the dynamic model. Eclipse simulator was used to solve the dynamic model and calculate the pressure in each gridblock. The outlet pressure was calculated at each time step by three different realization approaches for porosity and permeability, i.e., from experiments, from statistical analysis for the CT scan, and by the proposed image processing workflow. The simulated outlet pressure from the prosed workflow matched ideally, with a Pearson correlation coefficient of 0.98 and 0.99, the recorded one in the two experiments compared to underestimated or overestimated outlet pressure from the other two traditional realization approaches, i.e., statistical or experimental.

4.1 Porosity and Permeability Estimation Using Image Processing for Samples' CT Scan

The CT scan slices reflect the local anatomical configuration of the core sample [59]. Therefore, An image processing algorithm is proposed for estimating samples' porosity and permeability from a CT scan. Pores and grains are segmented using their pixels' grayscale response in each slice [30]. A particular grayscale threshold is selected to separate pores from grains based on the whole scan's color histogram [16]. After segmentation, pores' pixels are converted from grayscale to porosity scale with a linear relationship, e.g., zero-grayscale pixels become 2D square units with 100 % porosity, one-grayscale pixels (255 on a grayscale color code) become 0 % porosity units, and in between zero and one pixels will be scaled linearly to their corresponding 2D units. Then, the areal 3D volumetric fractions are calculated to give porosity for each 3D voxel in the scan. From that porosity 3D cloud, permeability for each 3D porosity voxel can be estimated using Kozeny-Carman correlation as a function of porosity as shown by **Equation (4)** [60].

$$k = c\frac{\phi^3 S^2}{(1-\phi)^2} \tag{4.1}$$

Where ϕ is the porosity of local voxels, S is the average grain diameter, and c is a unity proportionality factor [mD/mm^2].

The generated cloud of porosity and permeability data precisely defines the local heterogeneities at a very small scale, i.e., Microscale. The usefulness of estimating the petrophysical properties at that small scale is accurately reflecting local heterogeneities in coreflooding numerical models. Consequently, the resolution attributes of the converted scan should be adjusted/upscaled to match the numerical model grid configuration. The attributes to be tweaked are the scan's 2D XY resolution (i.e., images' height and width or the number of pixels in each direction) and Z resolution (i.e., slices number along with the sample) [9]. The original XY and Z resolutions should be upscaled because of computational power limitations to handle the equivalent numerical model. The upscaling process should honor representing the pore network of the sample. Therefore, coreflooding model finite gridblocks will be constructed to have the dimensions of upscaled pixels that are close to the average size of the sample's pore throats. **Figure 3** explains the upscaling criteria and the relation between the coreflooding model gridblocks' dimensions and grains' size.

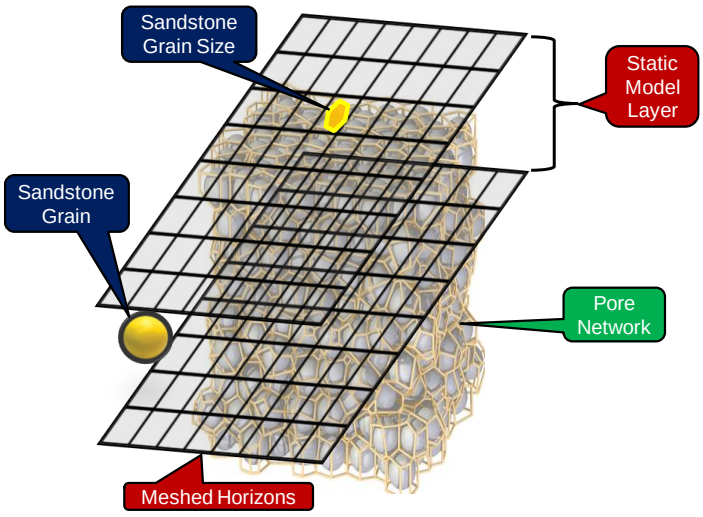

Figure 4.1: Finite volume grid dimensions are chosen to conform to the grain size

The used sample, in this work, is a standard commercial Berea sandstone core sample (**Figure 4**). Its dimensions are 1.5-inches in diameter and 2-inches in length, and its measured gas-porosimeter porosity and gas-permeameter permeability are 20% and 100 mD, respectively. Berea sandstone has a uniform mineral composition of 87 to 93% quartz, 3 to 9% feldspar, 0.5 to 3% dolomite, and 0.5 to 7% clays by volume [7]. Berea sandstone is homogenous and well-sorted with a pore throat diameter of is ranging from 50 to 150 µm.

Figure 4.2: Original Berea sandstone core plug (1.5 inches in diameter and 2 inches in length)

The optimum upscaled dimensions are selected to be 0.1 mm (100 µm) by 0.1 mm based on the average pore throat diameter of the Berea sample. The original CT scan images had an XY-resolution of 2084 x 2084 pixels, and it is upscaled (i.e., downsampled) 40 times, which resulted in a scan resolution of 52 x 52 pixels. After downsampling, one pixel covers an area of ~0.1-1 mm by 0.1-1 mm, as shown in **Figure 5**. The upscaling process is conducted by a simple mathematical interpolation to reach the required dimensions, i.e., width, height, and scan depth [61]. A discretized bicubic interpolation algorithm was used to conduct the XY-resolution upscaling [62]. The algorithm generates a 2D XY-smoothed regressed polynomial spline function of the third degree (**Equation (5)**). Sixteen adjacent pixels, indexed by x^i and y^j and i, j is from 0 to 3, are upscaled to create one new upscaled pixel. The regression coefficients, a_{ij}, are used to generate the new equivalent grayscale value of the new pixels.

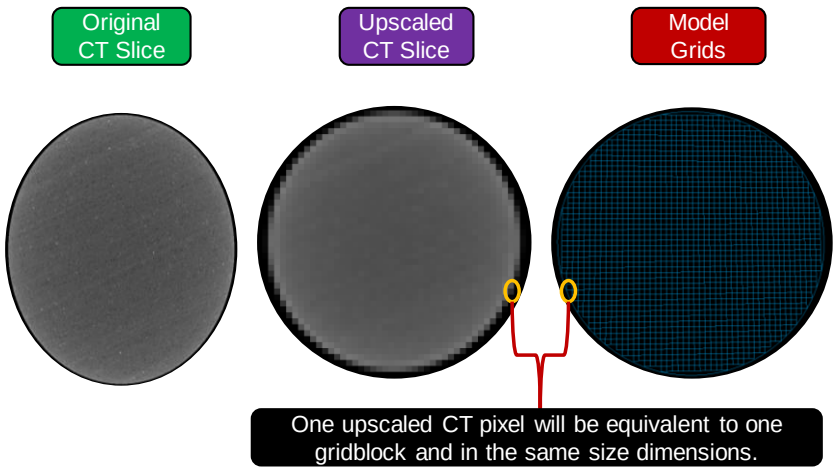

Figure 4.3: One upscaled CT pixel will be equivalent to one coreflooding simulation gridblock and in the same size dimensions.

$$f(x,y) = \sum_{i=0}^{3}\sum_{j=0}^{3} a_{ij}x^i y^j \tag{4.2}$$

A simple linear interpolation was employed to upscale the z-resolution from 1000 slice to 70 slices to keep the same aspect ratio of the XY-resolution. The linear Z-interpolation is implemented on the grayscale values of consecutive pixels. Then, the generated upscaled in-between pixels are combined

to construct new hypothetical slices. **Figure 6** (a and b) shows the final processed scan-stack, seventy CT slices, before and after applying the areal bicubic interpolation. This upscaled scan will be used to populate porosity and permeability data for the corresponding layers in the simulation model.

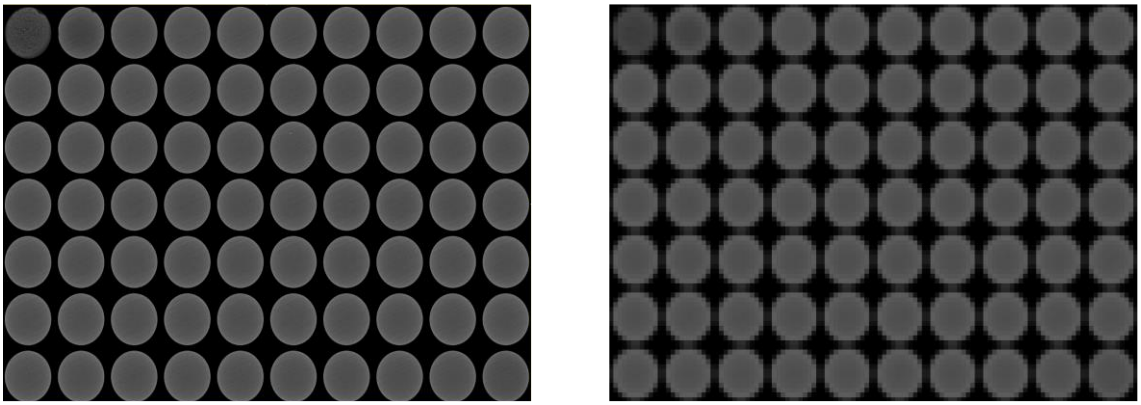

a. Original CT slices before upscaling its grayscale value

b. CT slices after upscaling its grayscale value using bicubic interpolation

Figure 4.4: Berea CT scan before and after upscaling its XY-resolution using bicubic interpolation

4.2 Constructing a Static Porosity and Permeability Static Model

A static model is a set of finite grids that represents the studied system architecture, such as its geometry and the static distribution of petrophysical properties like porosity and permeability [63]. Each grid is a small volume that has unique values for fluid, rock, fluid/rock properties, which reflect the geological structure of the system at this point in space. Petrel™, Schlumberger geologic modeling software suite, was used to build the static model based on the CT scan of the Berea sample. The following steps were followed to construct the 3D skeleton/static model in Petrel™.

4.2.1 Defining the Areal Extension and Boundaries of the Sample's Skeleton

The used Berea sample is a perfect cylinder with a diameter of 1.5 inches; therefore, a circular boundary was defined as a 2D boundary for the model. As shown in **Figure 7**, a reasonable number of bounding points wae defined to delineate the boundary circle. These points represent geometry restriction nodes for the constructed Cartesian mesh of the model. The number of boundary nodes is selected considering a tradeoff compromise between the model complexity, i.e., fewer points, and the boundary roundness, i.e., more points, to be as close as possible to the Berea sample.

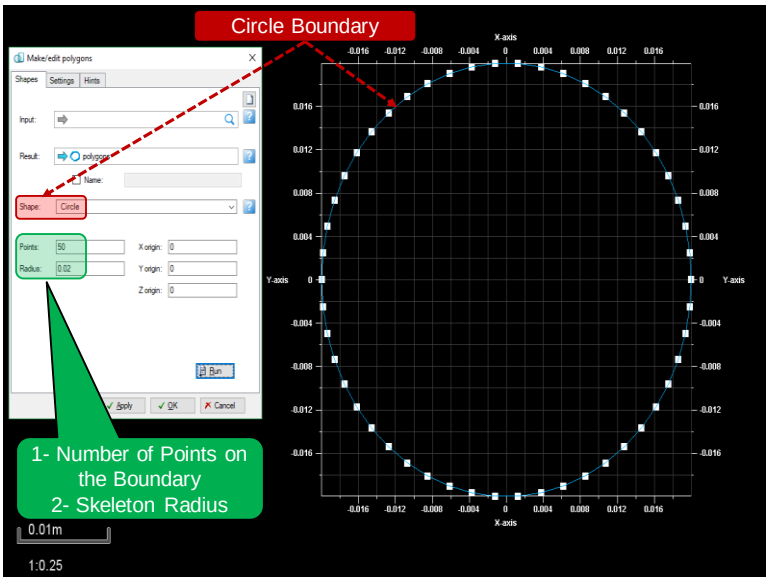

Figure 4.5: Circular boundary has the diameter of the core sample

4.2.2 Cartesian Meshing the Horizontal Section to the Required Dimensions

The 2D number of grids, in the static model, should match the upscaled CT images' XY-resolution, i.e., the upscaled number of pixels. Each grid will be equivalent to one upscaled pixel, as explained in **Figure 5**. Gridding is a tradeoff balance between computational power limitations, solution stability, and geometrical complexity. The chosen gridding system is a structured uniform Cartesian gridding which cannot track curved boundaries. **Figure 8** depicts this issue of trimming a part of the circular boundary, but on the other hand, other unstructured gridding systems, e.g., hybrid Cartesian-cylindrical gridding, cause matrix solvers' stability and conversion issues.

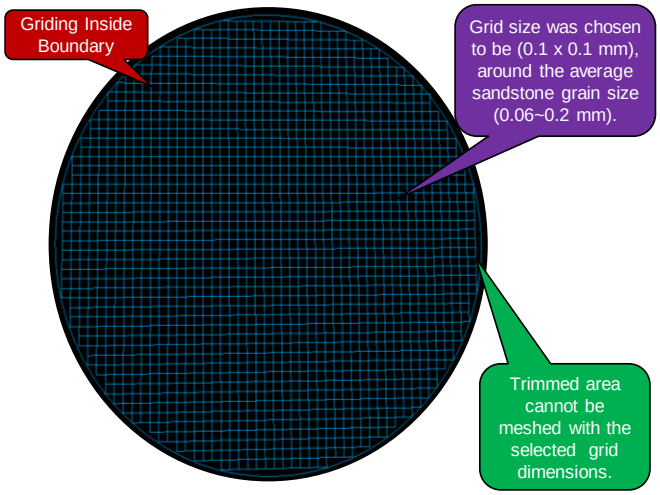

Figure 4.6: Meshing inside the circular boundary with a grid dimension of a sandstone grain

4.2.3 Extruding the Meshed Top Horizon Middle and Bottom Horizons

3D Coreflooding models require representing the studied sample's volume with consecutive layers of gridblocks. These layers are contained between meshed horizons; therefore, the 2D meshed top horizon is extruded to other 2D horizons, i.e., middle and bottom, in Z-direction. For a perfect cylindrical core sample, the three horizons have the same grid configuration, and coordinates expect for Z-coordinate as per **Figure 9**. The length of the Berea sample is 2 inches so that the top horizon is defined at zero Z-depth, the middle horizon is at (-ve) 1-inch depth, and the bottom one will be at (-ve) 2-inch depth.

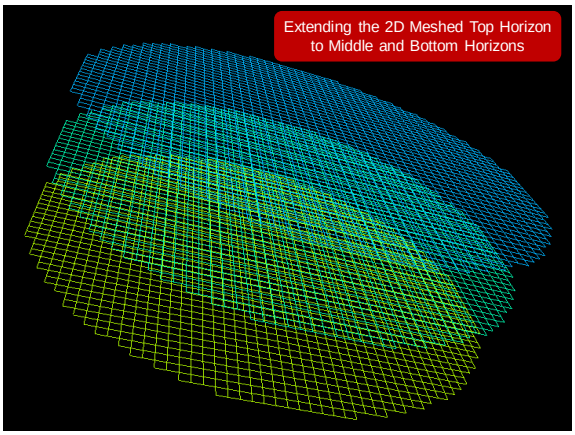

Figure 4.7: Extending the 2D meshed top horizon to middle and bottom horizons

4.2.4 Converting Meshed Horizons to Continuous Surfaces

Layering the coreflooding model, in Petrel, requires converting the three horizons to continuous surfaces to reflect the actual geologic topology of the sample. The fourth step (**Figure 10**) enables including layers' structure contour maps in the model. For core scale simulation, samples are represented with continuous horizontal surfaces as they are perfect cylinders, and there are no structural changes.

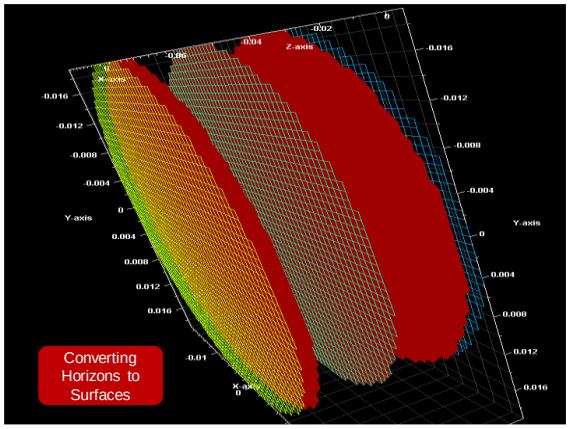

Figure 4.8: Converting top, middle, and bottom horizons to continuous surfaces

4.2.5 Model Vertical Layering

The number of layers, which is determined by the defined layer thickness, is controlled by the average grain size, as explained in **Figure 5**. Layers' thickness was selected to generate seventy layers corresponding to the seventy upscaled CT scan slices. The final skeletal Cartesian-configuration of the model is shown in **Figure 11,** in which the number of grids in each direction, i.e., Nx*Ny*Nz, equals 48*48*70, the number of total gridblocks is 161280, the number of active gridblocks is 129080, and the number of non-active gridblocks is 32200. Non-active gridblocks are the grids which are allocated outside the physical dimensions of the model or inside it but with zero porosity [64].

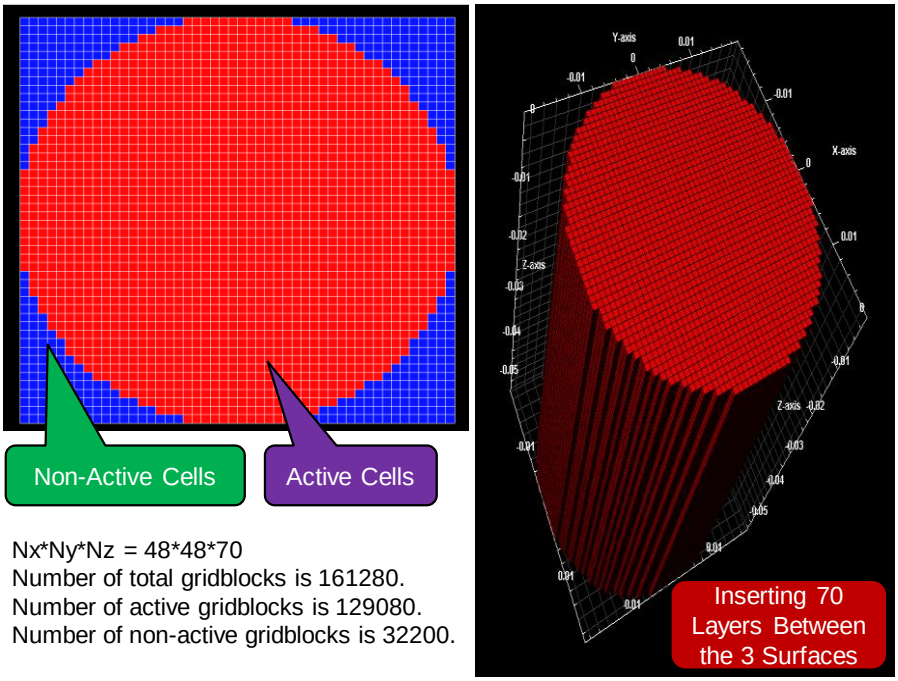

Figure 4.9: Vertical layering between the surfaces to construct final model 3D Skeleton

4.2.6 Geostatistical Populating the CT Scan-processed Porosity and Permeability

The upscaled CT porosity is populated to the 3D skeleton using a 3D multi-azimuth variogram. A variogram is a function that is used to fit a spatial correlation for an observed phenomenon, e.g., porosity [65]. A 3D variogram is mathematically defined by the difference between the spatial variance of the phenomenon value at two locations(s1 and s2). Given distance h, which separates s1 and s2, the semivariogram, γ (h), half the variogram, is defined in **Equation (6)** [66].

$$\gamma(h) = \frac{1}{2V} \iiint_{V} [f(M+h) - f(M)]^2 dV \tag{4.3}$$

Where M is a location in the cloud V, and f (M) is the value of the phenomenon at that location. CT Porosity was uploaded to Petrel as a cloud-data (x, y, z, and porosity value for each CT scan pixel).

Populating these data to the 3D skeleton requires three different variograms, aka, 3D multi-azimuth variogram. The first horizontal variogram represents the major horizontal anisotropy, and the second one is perpendicular to that major anisotropy direction. The third one is generated in the vertical/longitudinal direction. The fitting attributes, for the three variograms, reflect the porosity spatial variability. These attributes are variability type (exponential, spherical, or Gaussian.), sill (The steady limit of the variogram), nugget (variogram's jump at its origin), range, and anisotropy direction [67]. **Table 1** summarizes the obtained attributes for the three variograms. **Figure 12** (a and b) shows that the best spatial-fitted correlation was a Gaussian variogram model, while the variogram iso-value contour map shows an isotropic spatial variability around the core center. After populating the porosity to the model, the Kozeny-Carman correlation (**Equation (4)**) was used to generate the permeability model from the populated porosity model. Finally, **Figure 13** summarizes all the steps of generating a static model for a core sample based on its CT scan.

Table 4.1: 3D variogram descriptive parameters

Variogram	Type	Sill	Nugget	Range
Major	Gaussian	0.5872	0.4128	0.019
Minor	Gaussian	0.5872	0.4128	0.019
Vertical	Gaussian	0.7893	0.6325	0.05

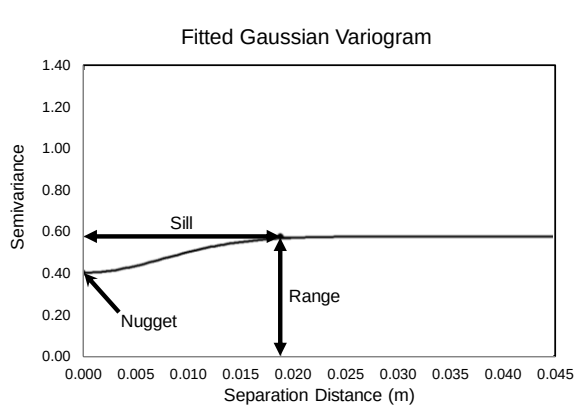

a. The 3D variogram generated for the CT-scan data using a commercial simulator

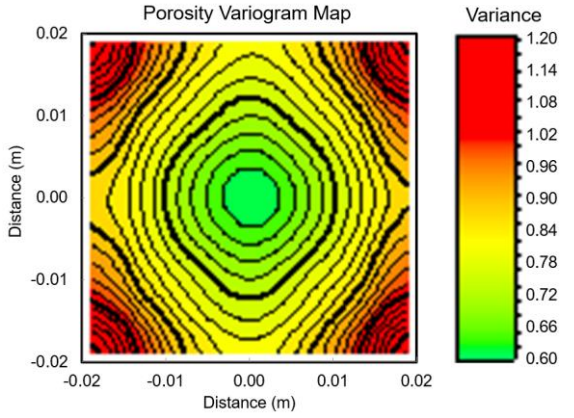

b. The variogram map generated for the processed CT-scan data, using a commercial simulator

Figure 4.10: Geostatistical multi-azimuth variogram and variogram map for porosity population

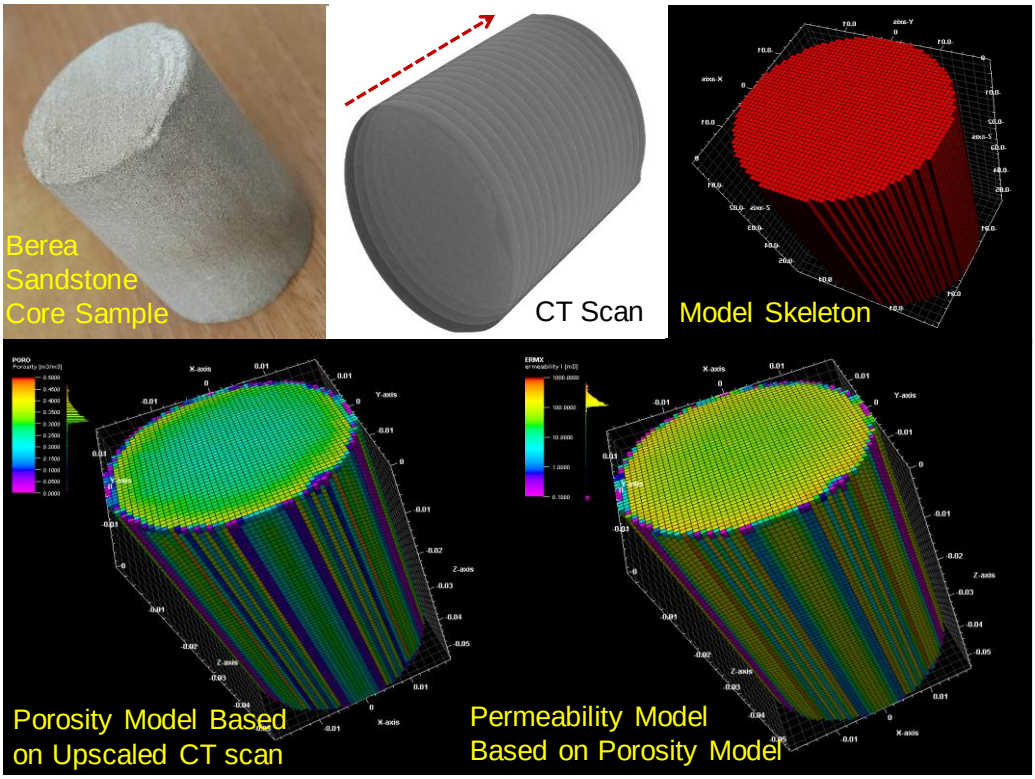

Figure 4.11: Steps of generating a static model for a core sample based on its CT scan

4.3 Modeling Transient Oscillating and Pulse Decay Permeability Experiment

Laboratory petroleum-related research provides reliable support for managerial decisions about developing oil and gas reservoirs [68]. Experiments like corefloodings are performed to experimentally simulate fluid flow in subsurface porous media under controlled conditions [69]. Corefloodings experiments enable predicting hydrocarbon recovery at early development stages and studying the feasible development options. Samples' petrophysical characterization is crucial to be conducted before analyzing coreflooding results and building their numerical models. The petrophysical characterization is a quantification for samples' hydraulic-flow properties [70]. Absolute permeability is a fundamental intrinsic flow-property that reflects samples' transport capacity and hence has a priority to be quantified precisely to build accurate coreflooding numerical models [71].

Permeability measurement techniques are categorized into steady-state and unsteady-state; transient techniques [72]. In the steady-state method, either a constant pressure difference or a constant flow rate is applied, and permeability is calculated from Darcy's law [73]. Tight samples will take a long stabilization time in steady-state experiments with high induced stress, which might affect the structure of the pore network. Transient methods with gases like Nitrogen are recommended for low permeability samples [74]. Notwithstanding its effectiveness, using gases has a problem of slippage and temperature sensitivity. Liquids, e.g., water, operate effectively in case of no interaction with samples minerals.

Permeability determination using transient methods showed its effectiveness, especially for tight samples where permeability can be units of Nano Darcies [75]. In a transient permeability experiment,

the input-end pressure is controlled and used to transmit time-dependent transient pressure-pulses to the sample [76]. Predefined amplitudes and phase settings control these transient pulses. Analytical solution for the diffusivity equation is used to estimate samples' permeability, given the recorded inlet and outlet pressures, sample dimensions, and pulse attributes. i.e., amplitude and phase [77]. Despite its accuracy, the estimated single-value permeability is derived from a simplified analytical solution with a dependency on the experiment conditions, i.e., pressure, temperature, and used fluid [78]. That bulk permeability ignores the effects of local heterogeneities inside the sample. Building coreflooding numerical models based on a single-value permeability/porosity can mislead the results' interpretation and causes a deviation from recovery profiles.

In this paper, a generic numerical model for coreflooding experiments is built based on an alternative realization approach for porosity and permeability rather than a single-value based approach. That approach is a realization for the local porosity and permeability by image processing samples' CT scans to track their local heterogeneities. The workflow starts with constructing the numerical model skeleton, i.e., boundaries and surfaces. Then, a fine 3D Cartesian grid is fashioned to represent the model's finite units on which governing flow equations will be applied. After that, gray-scale pixels in the CT scan are digitally binarized to a scale from 0 to 255 color code to segment the pore space. The binarized cloud of pixels is upscaled using 3D interpolation techniques and converted to an equivalent cloud of porosity data. The permeability cloud is consequently generated the porosity cloud by an empirical correlation. Geostatistical tools, i.e., 3D variograms and kriging algorithms in Petrel software, are used to populate porosity and permeability data to corresponding grids [79].

The generated static model is integrated with source nodes, i.e., injection and production, which are allocated to reflect the experiment's heads nozzles. The sources are defined with controls/constrains over local pressures and rates with time according to transient permeability experiment setup, e.g., sinusoidal pressure wave. For all gridblocks in the system, the diffusivity flow equations are discretized by finite difference technique, and Eclipse reservoir simulator is used to solve the created system of equations for pressure [80]. The simulated pressure is compared with the recorded experimental pressures.

4.3.1 Experimental Setup and Procedure of Transient Measurements for Permeability

AutoLab-1500 experimental setup by New England Research Inc. was used for performing the transient permeability experiment [81]. **Figure 1** shows the apparatus and its conceptual diagram of flow and controls. The core sample is placed inside a flexible rubber sleeve to enable applying confining pressure. The sleeve connects the sample to two cap heads with axial ports and circular grooves for distributing the used fluid, e.g., water to sample's entire surface. The sample holder is mounted into a vessel to be surrounded with hydrostatically confining mineral oil. A servo-controlled hydraulic intensifier controls upstream pressure while a miniature transducer monitors downstream pressure. The downstream transducer is attached to a small pocket as a downstream controlling volume of 0.63 cc.

The loading procedure starts with placing the core holder inside the vessel. The confining pressure is increased gradually to the desired level, which must be higher than the upstream pressure. After stabilization, pressurizing the upstream line, to the desired level, starts with a closed valve to the sample.

The downstream pressure should be constant at the atmospheric pressure if there is no leakage from the upstream line to the core; otherwise, there are integrity issues and a communication problem in the system. The transient pulse settings are defined based on the sample tightness. Tight samples require high-pressure pulse amplitude at low frequencies. Upstream pressure and downstream pressure are monitored and recorded when the upstream valve is opened.

Transient pressure pulses can be in the form of oscillating waves (a periodic function of time) or decay pulses [72]. During the experiment, the downstream pressure response follows the upstream source, e.g., a sinusoidal wave, with attenuated amplitude and a phase shift. Samples' permeability is calculated from the analytical solution of diffusivity equation using the ratio of upstream and downstream amplitudes and phase shift between the two waves [82,83]. The oscillating method has the advantage of being relatively short and can be used to estimate samples' porosity [84]. In the pressure-pulse decay method, a pressure pulse is supplied to make a sudden pressure difference in the sample until equilibrium [85]. The pulse decay method is considerably shorter compared to any other method. **Figure 2** summarizes the relationship between the upstream and downstream pressure in the three methods of permeability laboratory measurement.

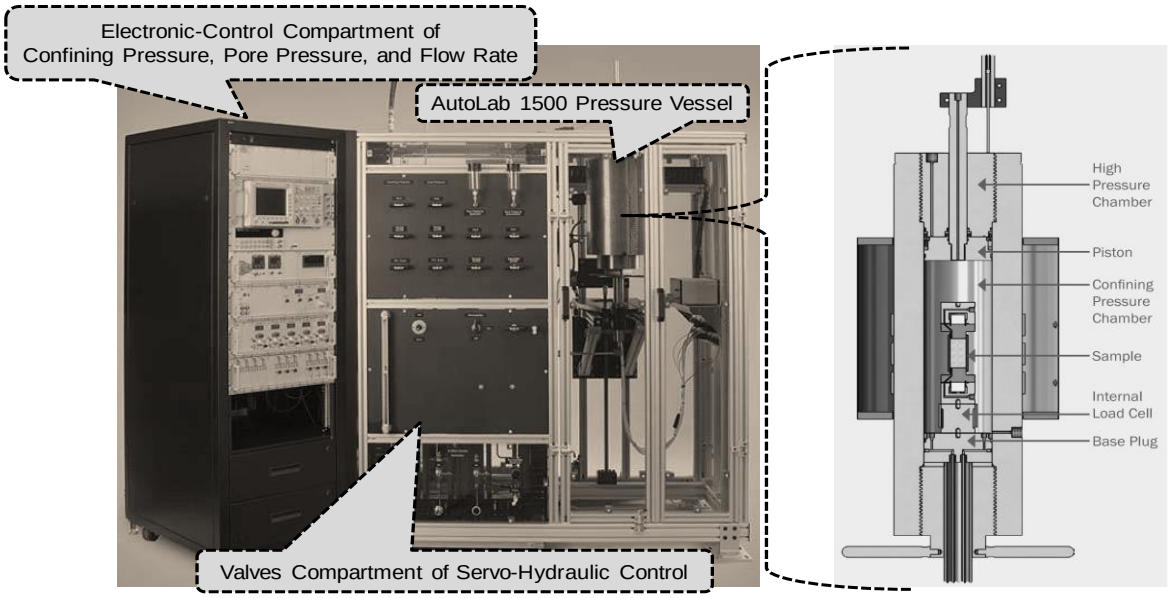

Figure 4.12: Schematic of AutoLab 1500 apparatus' pressure vessel, which is designed to perform transient permeability experiments on courtesy of New England Research (NER), Inc. [81][86]

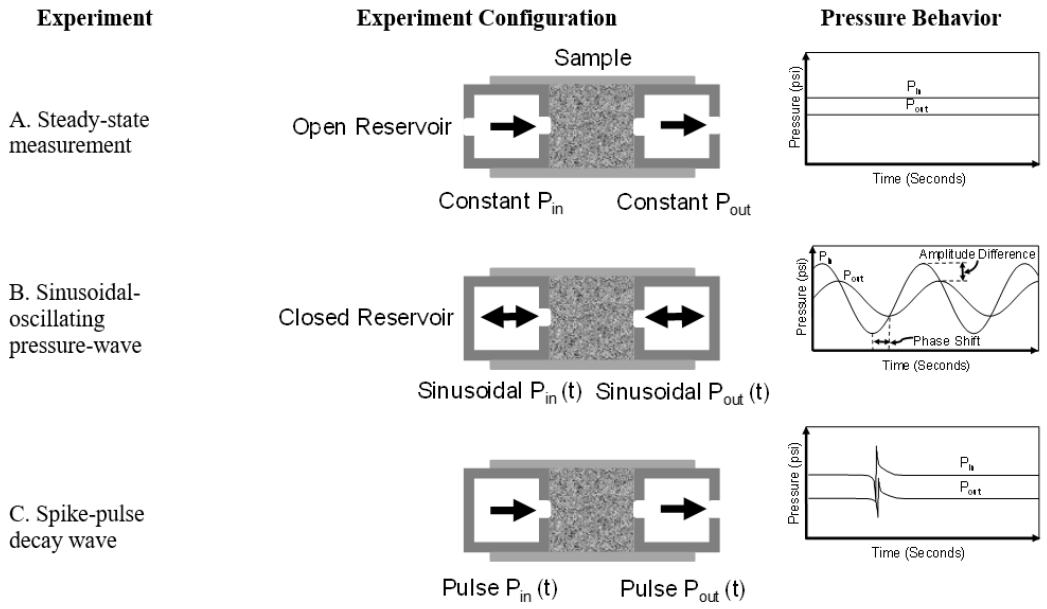

Figure 4.13: Types of transient waves in permeability measurement [87]

4.3.2 Analytical Solution

The downstream response in a transient permeability experiment is mainly controlled by permeability and specific storage [82]. Kranz et al. developed an analytical solution for the flow equation as a method for measuring hydraulic diffusivity. Fischer discussed the theoretical background, design considerations, and data analysis in transient permeability experiments in detail [83]. Bernabé et al. rearranged the analytical solution formulation to be a function of two parameters, i.e., amplitude attenuation and phase shift [77]. These two parameters are exclusive for samples with different permeability and porosity. The final solution form gives an estimate for dimensionless permeability and dimensionless porosity. The most simplified form of the analytical solution to correlate the downstream pressure response, p_{out}, with samples' rock properties is given by **Equation (1)** [72].

$$p_{out} = p_{in}(1 - e^{-kt/m}) \tag{4.4}$$

Where p_{in} is the pressure of amplitude at a time, t=0, m is a dependent constant on fluid properties and sample geometry, and k is the sample's permeability. Sinusoidal perturbation transfers **Equation (1)** from the time domain to the frequency domain, and it gives **Equation (2)** and **Equation (3)** [72].

$$A_r = (1 + \omega^2 m^2 k^{-2})^{-1/2} \tag{4.5}$$

$$\Phi = tan^{-1}(\frac{k}{\omega m}) \tag{4.6}$$

Where A_r is the amplitude ratio between p_{in} and p_{out}, Φ is the phase shift between them, and ω is the angular transfer frequency of the amplitude ratio at each time. Samples' permeability can be estimated using either the amplitude ratio or the phase shift equation.

Analytical estimation for permeability has limitations because of its assumptions and experiment setup constrains. For instance, it is affected by errors in readings caused by temperature changes, gas slippage effects, sensor errors, and laboratory noise [88]. Along with that, the assumptions of samples' homogeneity and isotropy are not valid in cases like shale formations due to the presence of lamination and the existence of induced or natural fractures. There are practical limitations on downstream reservoir volume, which impose constraints on high permeability samples with storage effects. The downstream capacity should be big enough to cover the impact of sample storage effects. Samples with a permeability of 1 mD to 100 mD will equilibrate in a few tenths of a second. Thus, to successfully estimate permeability for such core, the upstream transient pulse must be executed in milliseconds, which is not feasible for a hydraulic control system to achieve.

4.3.3 Constructing the Coreflooding Dynamic Model

Dynamic modeling of coreflooding experiments comes after static petrophysical modeling by including external flow sources, defining the initial conditions of the experiment, and setting the boundary conditions of the system. Simulating a coreflooding experiment requires a detailed description of the injection and production cap-grooves' configuration to guarantee a realistic representation of the flow paths. Injection grooves are defined as a well's completion nodes, as per Petrel and Eclipse simulator terminology, in layer-one and same for production grooves, but their nodes were in layer-seventy. Petrel defines those nodes as multilateral wells with three completion laterals, as shown in **Figure 14**. The bottom-hole pressure of the injection nodes is scheduled versus time to be similar to P_{in}, in the actual experiment. The producer pressure is left uncontrolled to be matched latter versus the recorded experimental P_{out}. By including the control schedule, the system is completed to simulate the actual coreflooding experiment by solving the differential diffusivity equation numerically. The diffusivity flow equation, in its discretized finite-difference form, is used to predict the pressure distribution through the experiment [89].

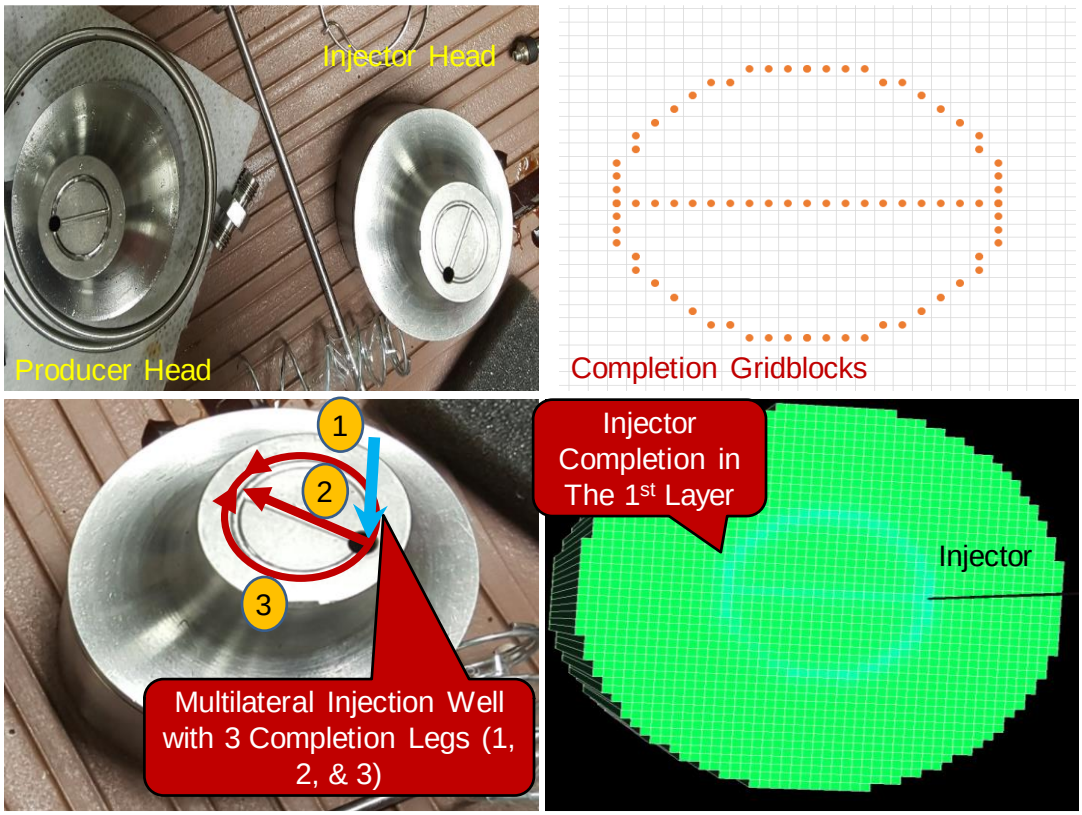

Figure 4.14: Wells (producer and injector) completion in the model based on heads configuration

4.3.4 Finite Difference Model

The finite-difference model is a numerical-approximation to discretize the derivatives in the flow equations using Taylor's series [90]. Discretized derivatives convert partial differential equations to algebraic equations. Those equations can be simultaneously and iteratively solved to estimate the new pressure distributions at further time steps using matrix solvers. **Equation (7)** represents the discretized form for a single-phase, i.e., water, flow equation to be implemented on each grid in the 3D dynamic model [91].

$$\sum_{j=1}^{n_i} T_{ij} \left(\frac{k_w}{\mu_w B_w}\right)_{ij}^{n+1} (\emptyset_{w_j} - \emptyset_{w_i})^{n+1} = \frac{V_{b_i}}{\Delta t}\left(\left(\frac{\phi}{B_w}\right)_i^{n+1} - \left(\frac{\phi}{B_w}\right)_i^{n}\right) + q_{w_i}^{n+1} \quad (4.7)$$

Where T, k, μ, B, ∅, V_b, Δt, ϕ, and q_w are grid transmissibility, permeability, viscosity, formation volume factor, fluid potential, pore-volume, time step, porosity, and external sink or source, respectively.

The generated finite-difference system of equations was solved for three scenarios of porosity and permeability realizations to show the significance of the CT processing workflow. With the same static skeleton and dynamic model, These scenarios are:

A. The traditional approach, in which unique values for porosity, 20 % measured by a gas porosimeter, and for permeameter, 100 mD measured by a gas permeameter, were assigned to all gridblocks
B. A statistical approach, in which unique values for porosity, 33 %, and permeameter, 175 mD, were assigned to all gridblocks. These values are inferred from the statistical analysis, mean values, of the processed CT-scan porosity, and permeability slices. **Table 2** and **Figure 15** demonstrate the statistical attributes and the frequency histogram for the processed CT-scan porosity and permeability. As mentioned earlier, permeability is dependent on porosity and hence has a similar frequency distribution.
C. Proposed image processing approach of the samples' CT-scan for assigning actual local porosity and permeability to gridblocks

Figure 16 shows a layer with different realizations for porosity.

Table 4.2: Image-processed CT-scan porosity and permeability statistical analysis

Statistical Attribute	Porosity	Permeability	Statistical Attribute	Porosity	Permeability
Mean	0.33	175	Range	0.463	656.387
Standard Error	0.000207	0.299649	Minimum	0.004	0.000
Median	0.333	153.093	Maximum	0.467	656.387
Mode	0.314	120.446	Sum	34124	18353383
Standard Deviation	0.066	96.245	Count	103164	103164
Sample Variance	0.004	9263.028	Largest (2)	0.467	656.387
Kurtosis	9.278	1.841	Smallest (2)	0.004	0.000
Skewness	-2.509	1.128	Confidence Level (95.0%)	0.000	0.587

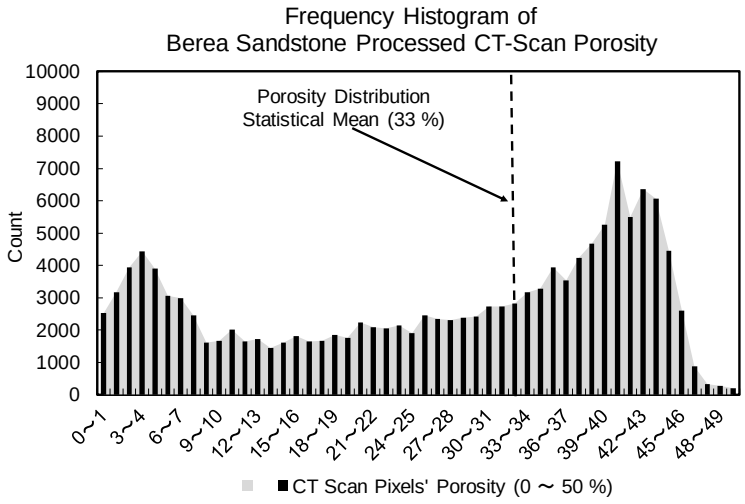

Figure 4.15: Frequency histogram of Berea sandstone processed CT-Scan porosity

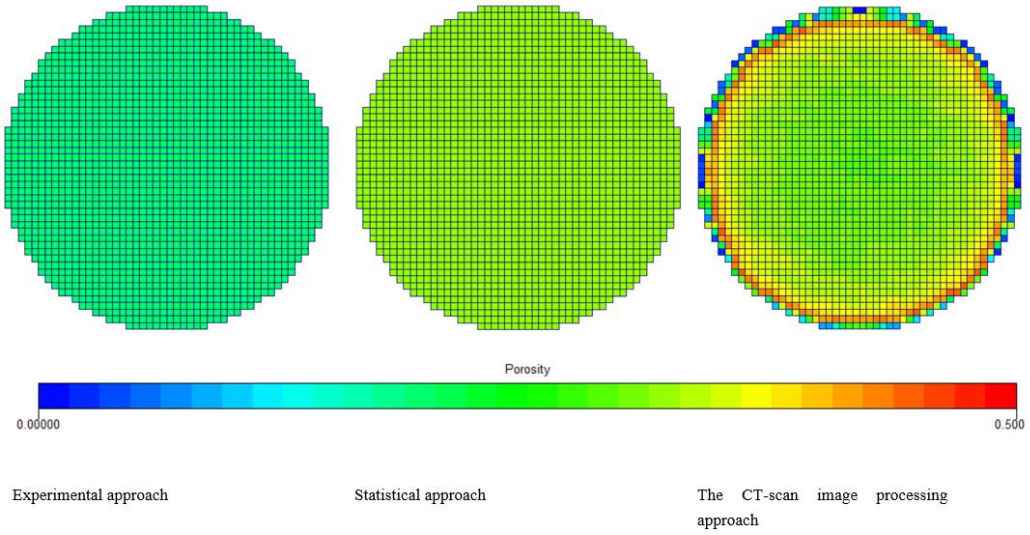

Figure 4.16: Approaches of porosity realization for coreflooding modeling

4.3.5 Results and Validation Versus Experimental Results

The ability of the constructed coreflooding dynamic-model, to accurately describe the core sample structure based on CT scan image processing, should be tested. The transient permeability experiment has multiple advantages to be used as a validation base for the proposed workflow. These advantages are:

1. Eliminating capillarity effects by using single-phase fluid, e.g., water, flooded in a standard water-wet sandstone,
2. Reducing fluid-compressibility effects by using incompressible fluid, e.g., water, and
3. Reflecting local-heterogeneities effects with transient pressure-waves and monitoring the instantaneous changes in the samples' responses

Figure 17 shows the simulation results, i.e., P_{out}, of the three realization approaches for two transient experiments, i.e., Sinusoidal oscillating pressure wave and spike pulse decay. There was no phase shift between P_{out} and P_{in} due to the high permeability of the sample. The experimental realization for porosity and permeability underestimated P_{out} in the two experiments. Contrarily, the statistical approach overestimated P_{out}. The CT scan approach precisely tracked the recorded uncontrolled P_{out} the producer head during both tests. As shown in **Figure 18** and **Figure 19**, the relative variance ((Recorded-Simulated)/Recorded) between each recorded P_{out} and the corresponding simulated pressure ranged between -2% and 5% for the two experiments. Pearson correlation coefficient was 0.98 and 0.99, calculated as the covariance of the recoded and simulated outlet pressure data of both experiments divided by their standard deviation product [92]. The simulated outlet pressure from the prosed workflow matched ideally, with the recorded one in the two experiments compared to underestimated or overestimated outlet pressure from the other two traditional realization approaches, i.e., statistical or experimental. That match, in pressure response and distribution (see **Figure 20**), is referred to its ability to reflect the local-heterogeneities effects.

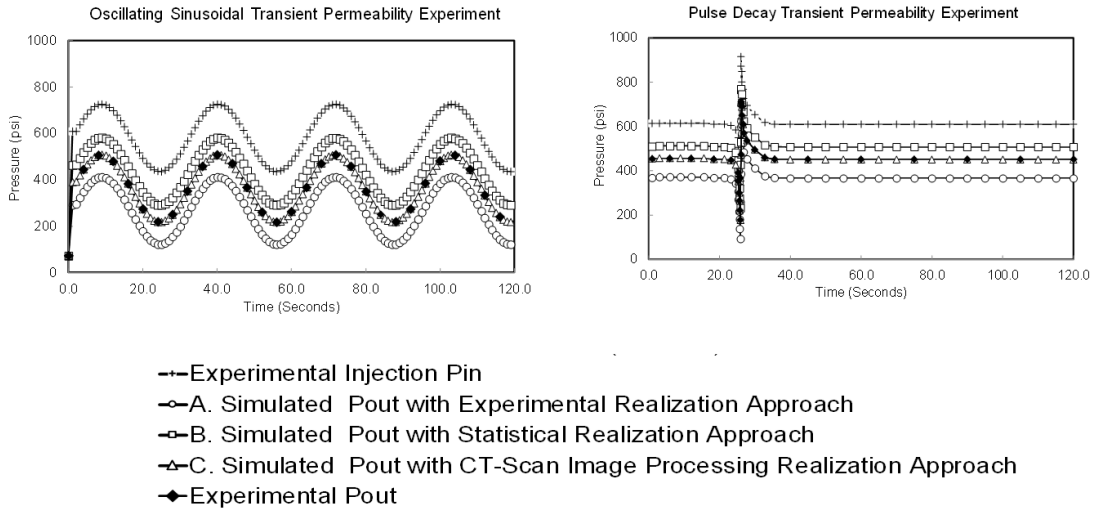

Figure 4.17: Simulation Results of transient permeability experiment (Left: Oscillating Sinusoidal Pressure, Right: Pulse Decay Method) using three realization approaches

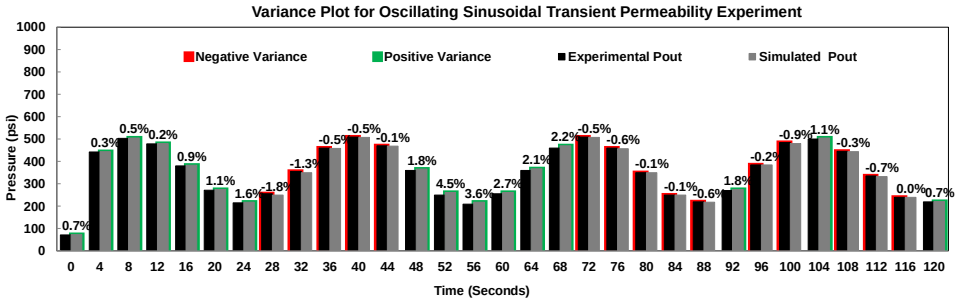

Figure 4.18: Comparing recorded Pout with its corresponding simulated Pout and presenting the relative variance for the oscillating sinusoidal transient experiment

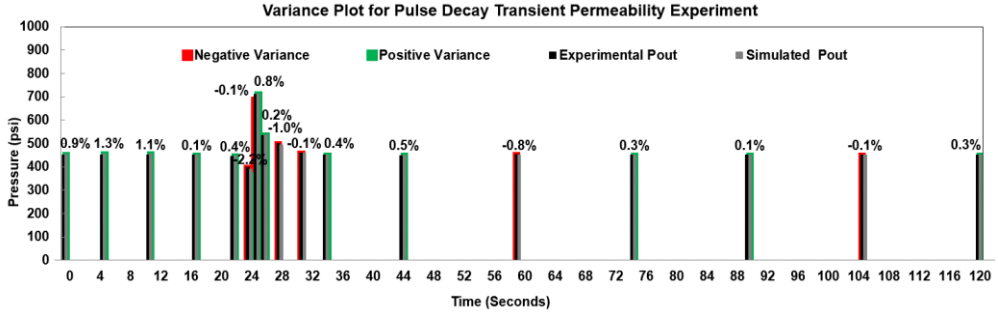

Figure 4.19: Comparing recorded Pout with its corresponding simulated Pout and presenting the relative variance for the pulse decay transient experiment

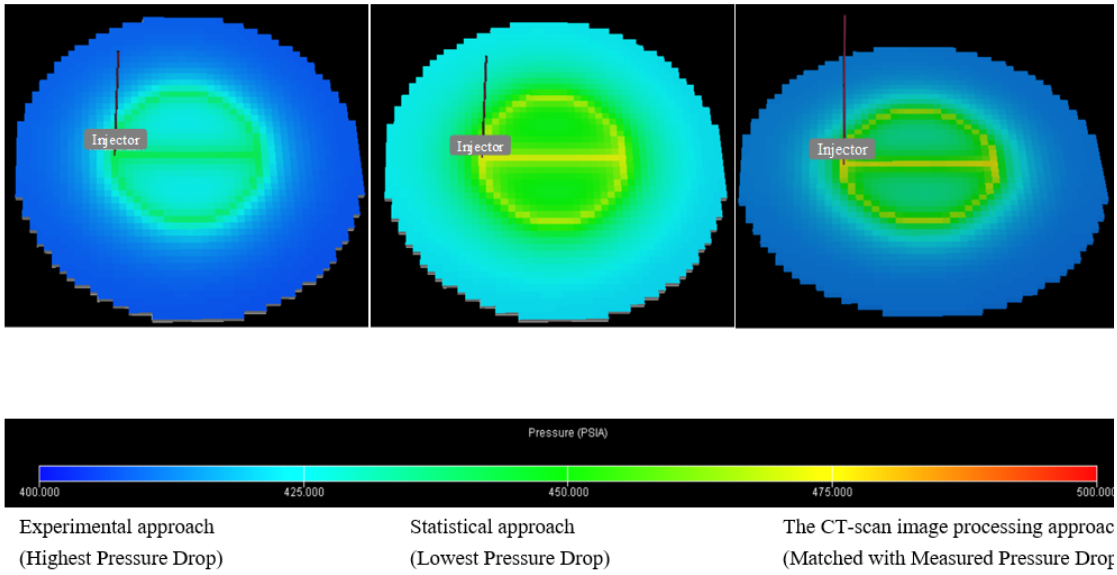

Figure 4.20: Pressure distribution, for the three realizations, approaches, in the production layer after 30 seconds in the oscillation experiment

4.4 CO2 Huff-n-Puff Experimentation and Numerical Simulation for 3D Printed Rock Samples

3D printed rock samples advance the experimental research of fluid flow physics in the petroleum industry. 3D printed replicas can be flexibly tailored to different experimental setups, in addition to the low cost of creation with uniform materials. The conducted experiments, on 3D printed samples, have less geometrical uncertainties, which is related to the accurately described structure of the pore network. The difficulties of describing fluid-rock interaction are diminished because of the compositional uniformity of the 3D-printing material. Therefore, 3D printed replicas were used, in this paper, to demonstrate the CO2 effects on oil recovery through a huff and puff experiment. The CT scan of a Berea core sample was reconstructed using image processing to prepare a 3D printable object. The two samples, i.e., the 3D printed gypsum replica and its original Berea core sample, were inserted simultaneously in a newly designed experimental setup to conduct the huff and puff experiment under the same conditions. The oil recovery was reported at three different CO2 injection pressures and temperatures. After running the experiment, the synthetic core sample was broken laterally and longitudinally to examine the CO2 action in the sample visually. As a pioneer study, the CO2 effect on a 3D-printed core sample was pictured, which can be used to explain the physics of CO2 diffusion in porous media. Finally, a supporting simulation model was created based on the CT scan to simulate the experiment. The simulation results matched the recovery results for the 3D printed replica and generated oil composition cross-sections similar to the pictured ones.

1. Introduction

Subsurface hydrocarbon reservoirs are considered as complex systems because of their heterogeneity and anisotropy at all scales, i.e., core, well, and reservoir scale [93] [94]. There are many uncertainties and challenges in describing a reservoir due to its non-uniformity from one point to another [95].

Reservoirs' future performance is predicted based on the simplified physics of fluid flow in porous media, which are implemented on the characterized rock-fluid system of the reservoir [96] [97]. Characterization uncertainties reduce the quality of performance prediction and impede the deep understanding of rock-fluid interaction phenomena [98]. Downhole core samples are acquired for experiments and characterization purposes [99]. The conducted experiments are simulated with the same physics with an underlying assumption, which is the uniformity of the understudy system at that small scale [100]. Unfortunately, that assumption is not always valid at any scale and led to the failure of lab-scale mathematical models to regenerate full-scale performance, especially for unconventional reservoirs [101].

3D printing technology was introduced to the experimental research of the oil and gas industry to reduce the characterization uncertainties [102] [103]. 3D printers' geometrical preciseness was boosted by the need to fabricate synthetic living organs using 3D printing technology [104] [105] [32]. The printing materials are chemically inert and have stable mechanical properties [106] [107]. Along with that, 3D printed replicas are cheap to create compared to the expensive cores and easily reproduced for destructive experiments [108]. Because of the spatially invariable composition of 3D printed replicas, the rock-fluid interaction can be accurately quantified in simulating the conducted experiments on them. Moreover, using the same geometry file in creating replicas and simulating experiments, leads to accurate characterization and matching results, which simplify the tuning process of the mathematical models. Therefore, investigating hydrocarbon-recovery responses of the 3D printed replicas' is a must for understanding the physics of fluid flow in porous media.

CO_2 huff-n-puff is preferred as an EOR technique for most reservoirs for numerous technical, economic, and environmental merits [109] [110]. Technically, CO_2 miscibility with oil enables reducing the residual saturation of unrecovered reserves [111] [112]. CO_2 is capable of wettability alteration and interfacial tension changes, which represent a substantial restriction for oil mobility [113]. CO_2 redundancy, from point-source coal-fired power stations, is a significant economic advantage [114]. This advantage aligns with the globally increasing demands of controlling greenhouse gas emissions [115]. CO_2 huff-n-puff is utilized where full-scale CO_2 EOR is not amenable in situations like minimal natural fracture network around the wellbore or compartmentalized formations with strong water drive [116]. The process of applying cyclical CO_2 huff-n-puff to stimulate aging wells is conducted by injecting the designed CO2 quantity till the required pressure into the well, followed by shutting the well for the predetermined soaking time, finally resuming production and monitoring recoverable hydrocarbons [117]. This cycle is repeated until it is not profitable to pursue, and CO_2 is not capable of recovering more oil.

In this paper, a newly designed experimental setup was used to simulate the CO_2 huff-n-puff process. The setup is designed to handle multiple samples simultaneously under the same conditions of pressure, temperature, and CO_2 injection. By leveraging the multiple-samples testing capability, an experiment of CO_2 huff-n-puff on a Berea core sample and its 3D printed replicas simultaneously [118]. The creation steps of 3D printed replica are presented as an image processing workflow for the CT scan of the Berea core sample. The reconstructed 3D-volume of the CT scan was utilized for 3D printing the replica, along with that, was used as a base for constructing the static and a dynamic model for simulating the CO_2 huff-n-puff. 3D geostatistical interpolation and kriging tools converted the grayscale voxels of the CT

scan to definite porosity and permeability values for the simulation model gridblocks. The gridblocks represented the static model of the system which was integrated with a fluid model of the compositional behavior of the hydrocarbon-CO_2 components using the Peng–Robinson equation of state [119]. Finally, the static and fluid model was integrated with a conforming numerical pseudo-CO_2 gas aquifer model with a pressure of the injection pressure of the CO_2 huff-n-puff experiment. The pseudo-CO_2 gas aquifer pressure was scheduled according to the cyclicity of injection/soaking/production of the experiment. The dynamic compositional model was solved by Eclipse reservoir simulator [120]. Finally, the simulated recovery, pressures, and residual hydrocarbon crosssections were compared with the recorded experimental ones from the experiment.

4.4.1 CO_2 Huff-n-Puff Experimental Setup

In a CO_2 huff-n-puff process, the selected well acts as an injector during the injection phase. CO_2 pushes the movable oil and water away from the near-wellbore region and bypasses the unmovable residual oil [121]. Pushing water to further locations in the reservoir reduces its saturation near the wellbore region, which increases the oil relative permeability [122]. Reservoir pressure is increased during the injection phase which drives oil competently later. During the soaking phase, CO_2 diffuses into the contact oil and activates the main huff-n-puff mechanism of viscosity reduction, oil swelling, reduction of interfacial tension, increasing water wettability, CO_2 solubility into the water, and solution gas drive [123]. The mass transfer of oil light/medium components into CO_2 happens in the soaking period. Such components are recovered from CO_2 during the production phase when the well is switched to act as a producer. The production pressure drops and movable water drive and flush the swelled oil toward the producer. **Figure 1** shows a conceptual diagram for horizontal well with multi-stage transverse hydraulic fractures.

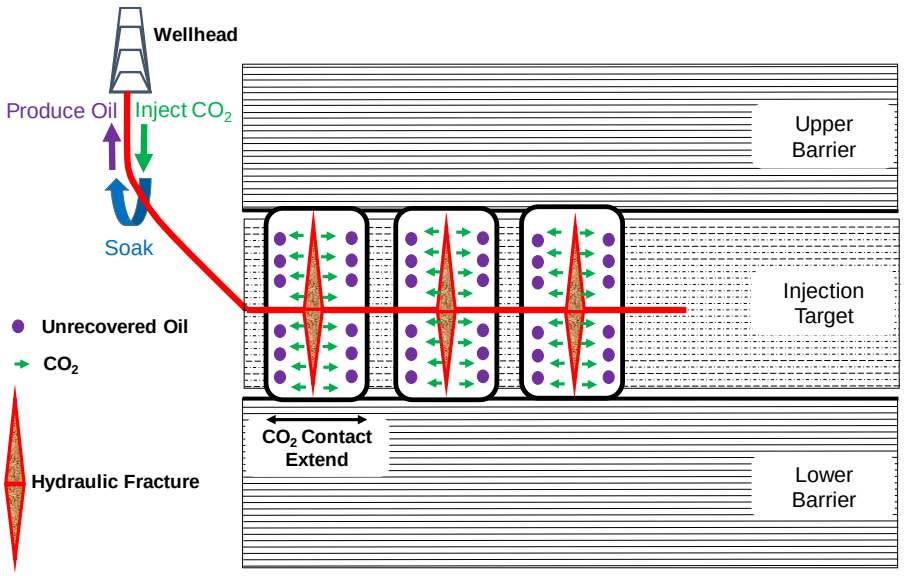

Figure 4.21: Conceptual diagram of CO2 huff-n-puff for horizontal well with multi-stage transverse hydraulically fractures

The setup used in the Huff-n-Puff test is presented in **Figure 2** and its schematic in **Figure 3**. The Huff-n-Puff setup consists of two vessels. The left one is used to encompass the test samples while the other vessel contains the CO_2 and used for pressurizing it. The two vessels are installed in an oven to control

the temperature of the experiment. The two vessels are connected with a CO_2 accumulator as a source for CO_2. The syringe pump is used to pressurize the CO_2 in the vessel by injecting water to push the piston upward. After pressurization to the specified level, CO_2 is transferred to the samples' vessel by opening the valves in between the two vessels. All valves and the reciprocating pumps are controlled and monitored with the data acquisition system by pressure transducers and a feedback loop connected to the real-time monitoring platform.

The Huff-n-Puff experiment procedure starts with samples' saturation. The samples are cleaned using toluene in the Dean-Stark distillation apparatus then dried for 24 hrs in a 120 ◦C desiccator oven. The dried samples are weighted to use their measured weights later in porosity estimations and recovery calculations. A vacuum pump is connected to the samples' vessel and used to evacuate the vapor from the samples' pores for 6 hrs. After that, the oil is flushed from the oil-filled/CO_2 vessel to the samples' vessel. The oil is pressurized to 3000 psi and was maintained for at least 24 hrs. The aging process was long enough to saturate both samples without changing the initial wettability conditions. Then, the samples are taken out and weighted to register the saturation weight. The samples are now fully saturated with oil (100%). The samples are reinstalled in their vessel, and all lines are vacuumed to start injecting CO_2. For one CO_2 huff-n-puff cycle, The CO_2 is injected for 1 to 30 min, and once the desired pressure and temperature are reached, all valves are closed to stop pistons from moving, and CO_2 is left to react with core samples for a 6 hrs soaking time. Then, the pressure is depleted gradually for 6 hrs with a rate of 20 psi/min till reaching the atmospheric pressure. The samples are weighed after each cycle, and the next CO_2 injection cycle starts immediately with the same procedure. The recovery is estimated experimentally by **Equation 1**.

$$Recovery = \frac{W_{after\ injection} - W_{dry}}{W_{saturated} - W_{dry}} \tag{4.8}$$

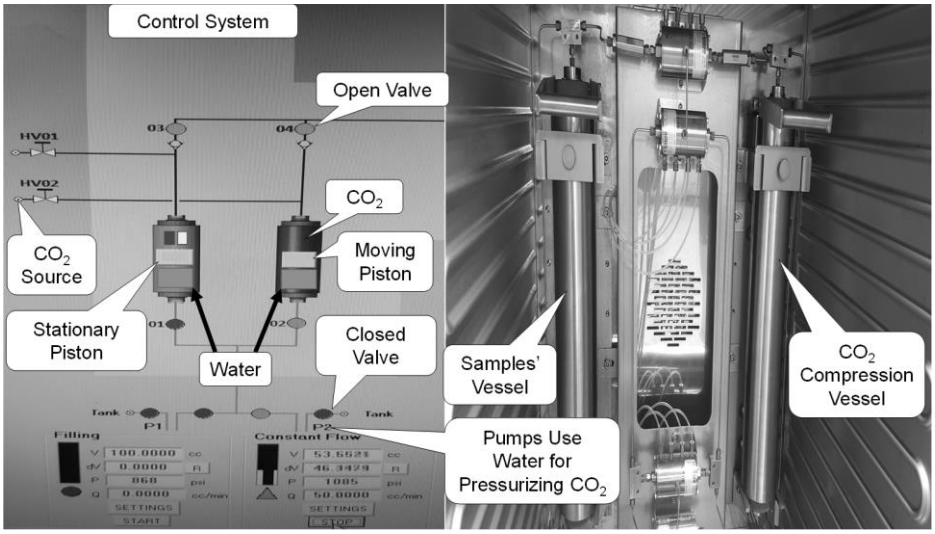

Figure 4.22: CO_2 huff-n-puff experimental setup and its control system

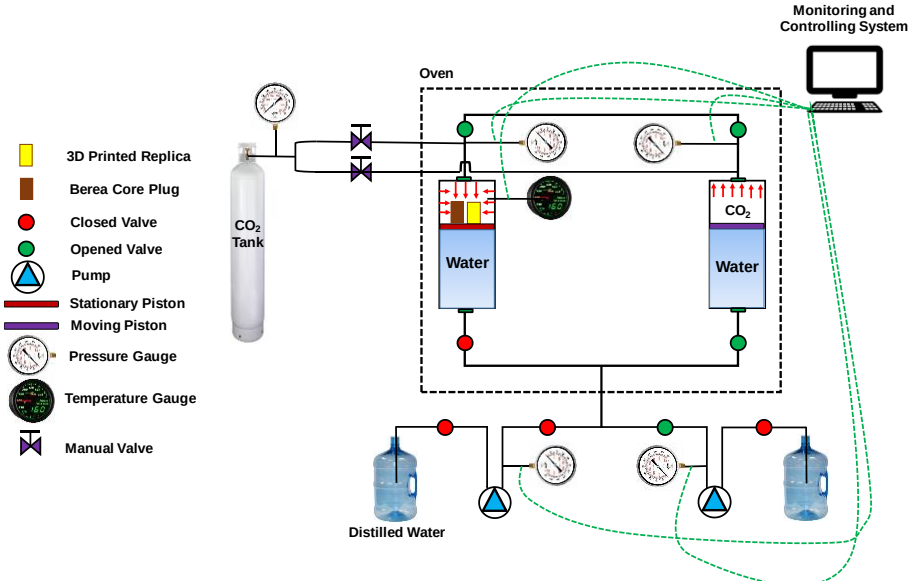

Figure 4.23: Schematic diagram for the CO_2 huff-n-puff setup for testing multi samples (Berea core sample and its replica)

4.4.2 Constructing a Finite Difference Simulation Model for CO_2 Huff-n-Puff Experiment

Core samples 3D printing enhances the preciseness of characterizing the understudy specimen in any petroleum-related experiment. Another valuable advantage that comes out from introducing 3D printing to oil and gas research, is that simulating models will be based on the same reconstructed CT scan for creating the sample itself. These simulation models will diminish any geometrical uncertainties and hence lead to accurate simulation results. Finite difference simulation for coreflooding experiments consists of two parts a static and a dynamic model of the sample [124]. A static model is composed of finite grids/volumes that reflect the core architecture, such as its structural geometry and petrophysical distribution in terms of porosity and absolute permeability [63]. Petrel™, Schlumberger's geologic-modeling suite, was utilized to construct the static model of the Berea sample and its gypsum replica based on their CT scan [125].

The skeleton of the model static was defined as a perfect cylinder considering the geometry of the Berea sample. That skeleton was meshed with a 3D Cartesian grid that has a grid dimension matching the upscaled CT voxels used in 3D printing. The number of layers in the model also matched the number of CT scan slices. The final skeletal Cartesian-configuration was 48*48*70 grid in each direction (161280 gridblock). The number of active-gridblocks was 129080, while for non-active gridblocks was 32200. Non-active gridblocks are allocated outside the model's physical dimensions with allocated zero porosity-value [64]. The upscaled CT grayscales voxels were normalized and converted to a porosity cloud using image processing, e.g., zero-grayscale voxels (a pore voxel) become a 100 % porosity gridblock and one-grayscale voxels (A sandstone grain voxel, 255 on a grayscale color code) become 0 % porosity gridblock. That porosity cloud was uploaded to the model and geostatistically populated using a 3D multi-azimuth variogram/kriging tools in Petrel to the 3D model [65]. The Kozeny-Carman permeability correlation (**Equation 2**) was implemented to the populated porosity model to generate the

static absolute permeability model [60]. **Figure 5** summarizes the construction steps of the static simulation model for the Berea core sample and its gypsum replica based on their CT scan.

$$k = c\frac{\phi^3 S^2}{(1-\phi)^2} \tag{4.9}$$

Where ϕ is the porosity of the gridblock, S is the average sandstone grain diameter, and c is a proportionality factor [mD/mm^2].

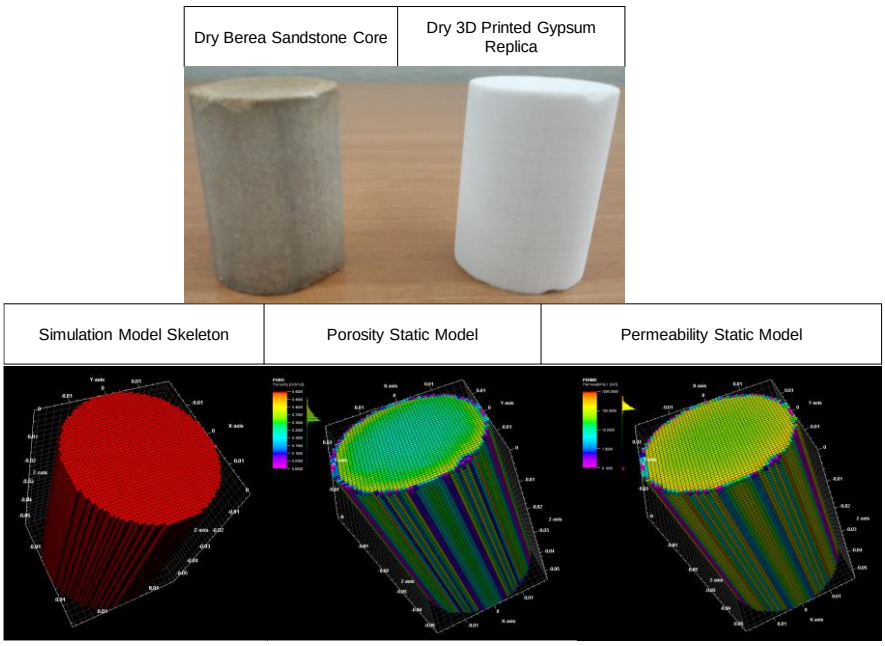

Figure 4.24: Steps of generating a static model for a core sample based on its CT scan

4.4.3 Mathematical Formulation of CO_2 Huff-n-Puff Experiment

The compositional mass-balance was used to characterize the variation of mass distribution in the vapor and liquid phases thermodynamically through the CO_2 huff-n-puff experiment [126] [110]. The used implicit 1-D finite difference form of the flow equation is represented by **Equation 3** for a gridblock i [127]. The flow equation along with the thermodynamic auxiliary equations are solved for all grid blocks to estimate the new pressure and compositional distribution for all components, $m = 1,2,\dots,n_c$, at a new time level $n+1$ [128]. Since the cores were dried, the water equation and water unknowns, i.e., water pressure p_w and water saturation S_w were excluded. The system is composed of a set of $(2nc+4)*I$ nonlinear equations in $(2nc+4)*I$ unknowns where nc is the number of components in the fluid model, and I is the number of grids in the model. The unknowns, for each gridblock; i, are the oil and gas pressure and the mole fractions in each phase, i.e., $(p_o, p_g, S_o, S_g, x_1, x_2, \dots, x_{nc}, y_1, y_2, \dots, y_{nc})_i$. The $(2nc+4)$ equations, for each gridblock; i, are the nc mass balance equations for each component (**Equation 3**) and the nc thermodynamic fugacity balance (**Equation 4**) for each component between the liquid and vapor phase, a constraint sum equation of mole fractions in the liquid phase (**Equation 5**), a constraint sum equation of mole fractions in the gas

phase (**Equation 6**), a constraint sum equation of saturations (**Equation 7**), and finally the capillarity relationship between pressures (**Equation 8**) [127].

$$\Delta\left[M_o^m\, T_o(\Delta p_o - \Delta pc_{go} - \gamma_0 \Delta D)\right]_i^{n+1} + \Delta\left[M_g^m T_g(\Delta p_g - \gamma_g \Delta D)\right]_i^{n+1} + (x_m \rho_o q_o + y_m \rho_g q_g)_i^{n+1} = \frac{V_{ri}}{\Delta t}\Delta_t\left[\emptyset(x_m \rho_o S_o + y_m \rho_g S_g)\right]_i \quad (4.10)$$

$$(fg_m)_i^{n+1} = (fo_m)_i^{n+1} \quad (4.11)$$

$$\left(\sum_{m=1}^{n_c} x_m\right)_i^{n+1} = 1 \quad (4.12)$$

$$\left(\sum_{m=1}^{n_c} y_m\right)_i^{n+1} = 1 \quad (4.13)$$

$$(S_o + S_g)_i^{n+1} = 1 \quad (4.14)$$

$$Pc_{go,i}^{n+1} = p_{g,i}^{n+1} - p_{o,i}^{n+1} \quad (4.15)$$

The counters are $i = 1, 2, \ldots\ldots, I\ (grid)$, $n = 0, 1, 2, \ldots\ldots,\ t\ (time\ level)$ and $m = 1, 2, \ldots, n_c\ (component)$. The generalized mobility, in **Equation 3**, is defined by $M_p^c = x_p^c\, k_{rp}(S_p)\frac{\rho_p}{\mu_p}$ where M_p^m is the generalized mobility of a component m in phase p, e.g., subscript; o for oil and subscript; g for gas, x_p^c is the mole fraction of component c in a phase p, k_{rp} is the relative permeability of phase p, S_p is the saturation of phase p, ρ_p is the molar density of phase p, μ_p is the viscosity of phase p, T is the geometrical transmissibility for a gridblock; i, Δp is the pressure difference between two adjacent gridblocks, γ is the phase specific gravity, ΔD is the depth difference between two adjacent gridblocks, f is the component fugacity, x_m is the m-component mole fraction in liquid phase, y_m is the m-component mole fraction in vapor phase, $q_{o,g}$ is the oil or gas external source, V_{ri} is the gridblock bulk volume, Δt is the time step, $\emptyset$ is the gridblock porosity, $S_{o,g}$ is the oil or gas saturation, and finally, Pc is the capillary pressure as a function of oil saturation.

4.4.3.1 Solution Algorithm

Newton-Raphson algorithm was used to solve the reduced residual form of Equation 3 to Equation 8 [129]. The equations' residuals should be minimized iteratively by the unknowns' perturbation till reaching zeros. Newton-Raphson arrangement is given by Equation 9 and the Jacobian residual derivatives matrix, for a gridblock; i, is presented by Equation 10, being $[J]$ the $nc * nc$ Jacobian matrix, or matrix of derivatives, ∂U is the vector of change in the unknowns, $(\partial U_{(2nc+2)1}, \partial U_2, \ldots, \partial U_I)^T$ and the $(2nc + 2)$ sub-vector for each gridblock; $\partial U_i = (\partial p_o, \partial S_g, \partial x_1, \partial x_2, \ldots, \partial x_{nc-1}, \partial y_2, \partial y_3, \ldots, \partial y_{nc})_i^T$, F is the vector of residuals $(F_{(2nc+2)1}, F_2, \ldots, F_I)^T$, and $v = 0, 1, 2, \ldots (iteration\ level)$. Considering that ∂^{v+1} represents the change of the unknowns, $\partial U^{v+1} = U^{v+1} - U^v$, over an iteration; $v + 1$. After reaching the equilibrium and conversion, the gas pressure; p_g and oil saturation; S_o calculated from Equation 7 and Equation 8. Also, the x_{nc} is Equation 5 and y_1 is Equation 6 [130] [127] [129].

$$[J]^{v}\partial U^{v+1} = -F^{v} \tag{4.16}$$

$$\begin{bmatrix} \frac{\partial R_{m=1}}{\partial p} & \frac{\partial R_{m=1}}{\partial S_g} & \frac{\partial R_{m=1}}{\partial x_1} & \cdots & \frac{\partial R_{m=1}}{\partial x_{nc-1}} & \frac{\partial R_{m=1}}{\partial y_2} & \cdots & \frac{\partial R_{m=1}}{\partial y_{nc}} \\ \vdots & \vdots & \vdots & & \vdots & \vdots & \cdots & \vdots \\ \frac{\partial R_{m=nc}}{\partial p} & \frac{\partial R_{m=nc}}{\partial S_g} & \frac{\partial R_{m=nc}}{\partial x_1} & \cdots & \frac{\partial R_{m=nc}}{\partial x_{nc-1}} & \frac{\partial R_{m=nc}}{\partial y_2} & \cdots & \frac{\partial R_{m=nc}}{\partial y_{nc}} \\ \frac{\partial R_{f,m=1}}{\partial p} & \frac{\partial R_{f,m=1}}{\partial S_g} & \frac{\partial R_{f,m=1}}{\partial x_1} & \cdots & \frac{\partial R_{f,m=1}}{\partial x_{nc-1}} & \frac{\partial R_{f,m=1}}{\partial y_2} & \cdots & \frac{\partial R_{f,m=1}}{\partial y_{nc}} \\ \vdots & \vdots & \vdots & & \vdots & \vdots & \cdots & \vdots \\ \frac{\partial R_{f,m=nc}}{\partial p} & \frac{\partial R_{f,m=nc}}{\partial S_g} & \frac{\partial R_{f,m=nc}}{\partial x_1} & \cdots & \frac{\partial R_{f,m=nc}}{\partial x_{nc-1}} & \frac{\partial R_{f,m=nc}}{\partial y_2} & \cdots & \frac{\partial R_{f,m=nc}}{\partial y_{nc}} \end{bmatrix}^{v} \cdot \begin{bmatrix} \partial p_{o,i} \\ \partial S_{g,i} \\ \partial x_{1,i} \\ \vdots \\ \partial x_{nc-1,i} \\ \partial y_{2,i} \\ \vdots \\ \partial y_{nc,i} \end{bmatrix} = -\begin{bmatrix} R_{m=1,i} \\ \vdots \\ R_{m=nc,i} \\ R_{f,m=nc,i} \\ \vdots \\ R_{f,m=nc,i} \end{bmatrix}^{v} \tag{4.17}$$

4.4.3.2 Thermodynamic Balance from Equation of State

The thermodynamic distribution of insitu components among phases is inferred from **Equation 4** or fugacity equation. The fugacity of a chemical component, c, in a phase, i.e., $p = o, g$, is given by **Equation 11** [119].

$$f_p^c = p_p \, x_p^c \, \Psi_p^c \tag{4.18}$$

Where p_p is calculated from the Peng and Robinson equation of state, x_p^c is the mole fraction of component c in a phase p, and Ψ_p^c is the fugacity coefficient which can be estimated from **Equation 12** [131].

$$\ln \Psi_p^c = \frac{b^c}{b_p}\left(Z_p - 1\right) - \ln\left(Z_p - B_p\right) - \frac{A_p}{2\sqrt{2}B_p}\left(\frac{2}{a_p}\sum_{l=1}^{nc} x_p^l \,(1 - K_l^c)\sqrt{a^c\, a^l} - \frac{b^c}{b_p}\right).ln\left(\frac{Z_p + (1+\sqrt{2})B_p}{Z_p - (1-\sqrt{2})B_p}\right) \tag{4.19}$$

Where K_l^c is the binary interaction constant between components c and l, The EOS mixing principle is used to estimate $b_p = \sum_{c=1}^{nc} x_p^c \, b^c$, $a_p = \sum_{m=1}^{nc}\sum_{l=1}^{nc} x_p^c \, x_p^l (1 - K_l^c)\sqrt{a^c\, a^l}$, $a^c = 0.45724\, \alpha^c \frac{R^2\, T_C^{c\,2}}{P_C^c}$, $b^c = 0.077796 \frac{R\, T_C^c}{P_C^c}$, such that R is the universal gas constant, T is the temperature, T_C^c and P_C^c are the critical temperature and pressure of a component c, $\alpha^c = \left(1 + (0.37464 + 1.5423\, \omega^c - 0.26992\, \omega^{c\,2})\left[1 - \frac{\sqrt{T}}{\sqrt{T_C^c}}\right]\right)^2$, T is the temperature and ω^c is the acentric factor of components c. PR EOS, **Equation 13**, and its cubic equation, **Equation 14**, are solved iteratively to estimate p_p, Z_p, and the deviation Factors; $A_p = \frac{a_p p_p}{R^2 T^2}$, $B_p = \frac{b_p p_p}{R\, T}$ [129].

$$p_p = \frac{RT}{V_p - b_p} - \frac{a_p(T)}{V_p(V_p + b_p) + b_p(V_p - b_p)} \text{ and the molar volume; } V_p = \frac{Z_p RT}{p_p} \tag{4.20}$$

$$Z_p^3 - (1 - B_p)Z_p^2 + (A_p - 2B_p - 3B_p^2)Z_p - (A_p B_p - B_p^2 - B_p^3) = 0 \tag{4.21}$$

4.4.3.3 Representing CO_2 injection with A Constant-head Numerical CO_2 Aquifer

All boundary gridblocks are exposed to the CO_2 during the injection phase of the experiment and CO_2 should be included as a source term in their flow equations. Those gridblocks also produce the recovered oil during the production phase of the experiment because of the pressure drop around the core. Representing that interaction was defined to the dynamic model by a constant-head numerical CO_2 aquifer communicating with the boundary gridblocks [132] [133]. The influx of CO_2 is represented by **Equation 15** [134]. The aquifer pressure was scheduled versus time to be the CO_2 injection pressure of huff-n-puff experiment. In addition to the thermodynamic interchange between the phases, the diffusion between CO_2 the insitu hydrocarbon is driven by the concentration gradient as in **Equation 16** [135].

$$q_{CO_{2_i}}^{n+1} = J\, A_f [p_{CO_2} - p_{CO_{2_i}}^{\ n} + \rho_{CO_2}\, g(d_i - d_a)] \tag{4.22}$$

where J is the productivity index, A_f is the gridblock's areal connection fraction to the CO_2 aquifer, p_{CO_2} is the CO_2 aquifer pressure, $p_{CO_{2_i}}^{\ n}$ is the CO_2 pressure in the gridblock; i, at a time level; n, ρ_{CO_2} is CO_2 density in the CO_2 aquifer, d_i is the depth of the gridblock; i, and d_a is the depth of the CO_2 aquifer.

$$J^c = -\left(\frac{1}{V_p}\right) D^c \frac{\partial\, x_p^c}{\partial d} \tag{4.23}$$

Where J^c is the molar flux of a component c per unit are and D^c is the component diffusion coefficient.

4.4.4 Experiment Results and Simulation Validation

Figure 6 shows both saturated Berea core sample and its gypsum 3D printed replica with crude Bakken oil [52] [118]. The oil saturation effect is obliviously noted on gypsum replica because of its compositional purity. Standard Bakken oil is characterized by seven pseudo-components and their corresponding Peng-Robinson EOS properties and molar fractions are listed in **Table 1** [136] [52].The PR EOS were used to generate the blackoil properties of the fluid model, e.g. oil compressibility, viscosity, and density versus pressure. The CO_2 was injected at three injection pressures of 850, 1200, and 3500 psi. Three injection/production cycles were conducted for each pressure at a temperature of 220 °F. After conducting the experiment, the 3D printed replica was sliced laterally and longitudinally to visually investigate the core's interior and the effects of the CO_2 injection as shown in **Figure 7** [118]. The capability of reprinting the replica cheaply encouraged slicing and destroying the replica for visual investigation which is not possible for natural cores, especially, for extended experiments. The extended experiment can be pursued and repeated on another 3D printed replica with the exact pore network and core material. The purity of the 3D printed sample enabled allocating the CO_2 effects inside the sample which represented a solid base for validating the simulation model of the experiment along with the measured oil recovery.

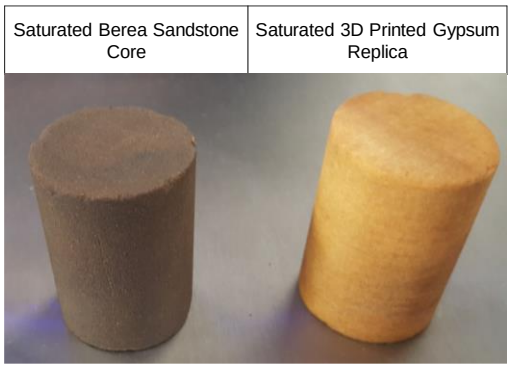

Figure 4.25: Saturated Berea core sample and its gypsum replica with Bakken oil

Table 4.3: Peng-Robinson Properties of Bakken Oil

	Peng-Robinson EOS Parameters							Binary Interaction Parameters						
Component	Dead Oil Molar Fraction	Critical Pressure (atm)	Critical Temperature (K)	Critical Volume (L/mol)	Molar Weight (g/gmol)	Acentric Factor	Parachor Coefficient	CO_2	N_2-C_1	C_1-C_4	C_5-C_7	C_8-C_{12}	C_{13}-C_{19}	C_{20}-C_{30}
CO_2	0.00008	72.8	304.2	0.094	44.01	0.225	78	0	0.1013	0.1317	0.1421	0.1501	0.1502	0.1503
N_2-C_1	0.00196	45.24	189.67	0.0989	16.21	0.0084	76.5	0.1013	0	0.013	0.0358	0.0561	0.0976	0.1449
C_1-C_4	0.07621	43.49	412.47	0.2039	44.79	0.1481	150.5	0.1317	0.013	0	0.0059	0.016	0.0424	0.0779
C_5-C_7	0.05275	37.69	556.92	0.3324	83.46	0.2486	248.5	0.1421	0.0358	0.0059	0	0.0025	0.0172	0.0427
C_8-C_{12}	0.43691	31.04	667.52	0.4559	120.52	0.3279	344.9	0.1501	0.0561	0.016	0.0025	0	0.0067	0.0251
C_{13}-C_{19}	0.28862	19.29	673.76	0.7649	220.34	0.5672	570.1	0.1502	0.0976	0.0424	0.0172	0.0067	0	0.0061
C_{20}-C_{30}	0.14347	15.38	792.4	1.2521	321.52	0.9422	905.7	0.1503	0.1449	0.0779	0.0427	0.0251	0.0061	0

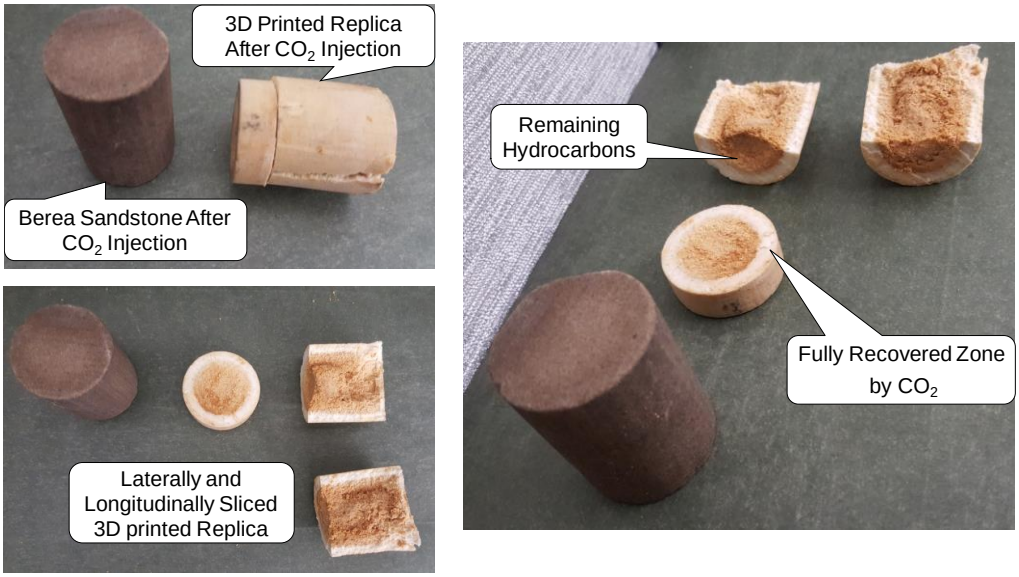

Figure 4.26: Laterally and longitudinally sliced 3D printed replica after CO_2 huff-n-puff experiment

The dynamic model had a control over the CO_2 aquifer pressure during the injection and the production phases. Brooks-Corey was used to generate the gas-oil relative permeability with K_{rg} = 0.096, K_{rog} = 0.106, S_{lg} = 0.730, S_{gr} = 0, n_g = 2, and n_{og} = 2.5 [137]. The injection pressure was scheduled to be three cycles of an 850 psi, 1200 psi, and finally followed by 3500 psi. The soaking time was 6 hours after each injection with a zero CO_2 aquifer pressure. The average model pressure was calculated to indicate

the amount of the stored driving force to flush the remaining hydrocarbon out of the core during the production sequence. The simulated average pressure is shown in **Figure 8** which is estimated by the "hydrocarbon weighted" gridblocks' pressure.

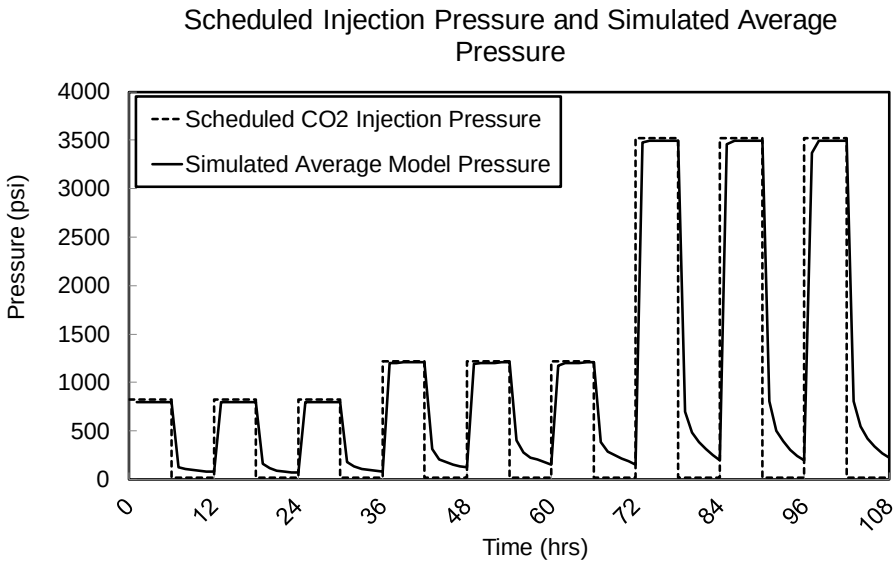

Figure 4.27: Model control over CO_2 injection pressure and the simulated average pressure

The CO_2 – hydrocarbon interaction physics can be understood when the simulation model generates matching results to the conducted experiment. Therefore, **Figure 9** and **Figure 10** compares the saturation configuration of the sliced 3D printed replica after the experiment with the corresponding cross-sections in the model, i.e. the z-layer 15 and 25 x-cross-section. The matching between the physical and simulated saturation distribution is a beneficial output of the ideality of the 3D printed replica and the simulation model, considering that both of them are based on image processing the CT scan of the Berea core sample. The simulated experimental oil recovery better matched the measured recovery of the printed replica compared to the Berea recovery after each CO_2 huff-n-puff cycle as shown in **Figure 11**.

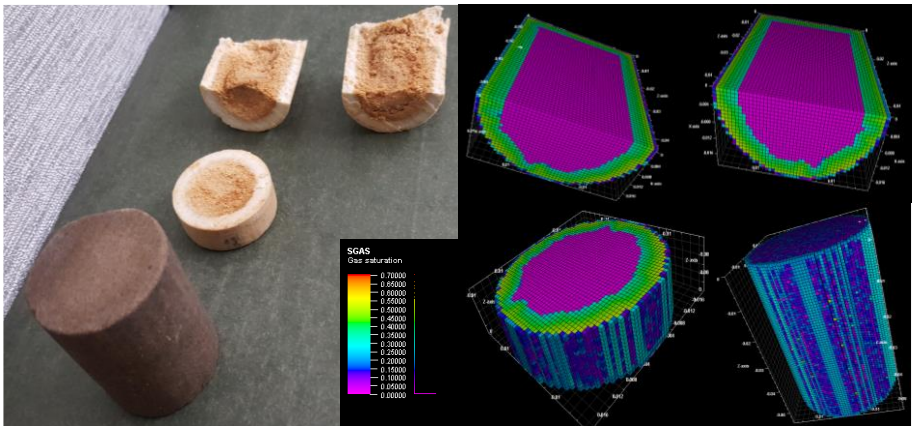

Figure 4.28: 3D view of the sliced 3D printed replica versus the simulated saturation distribution of the CO_2 huff-n-puff experiment

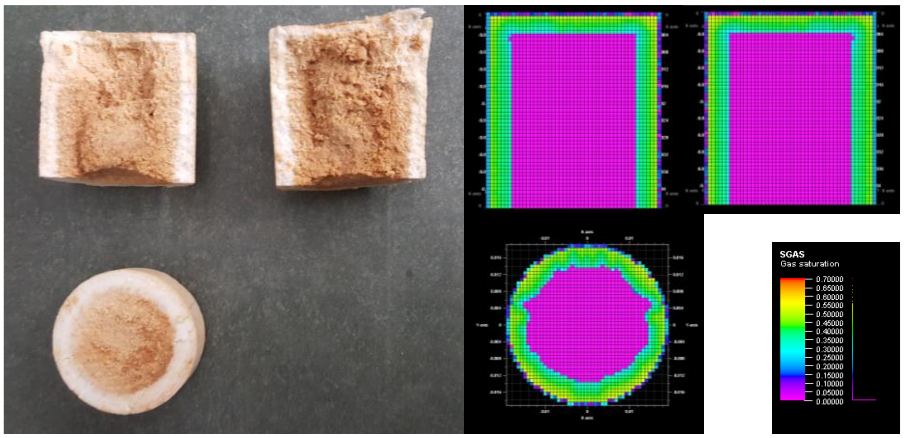

Figure 4.29: 2D view of the sliced 3D printed replica versus the simulated cross-sectional saturation distribution

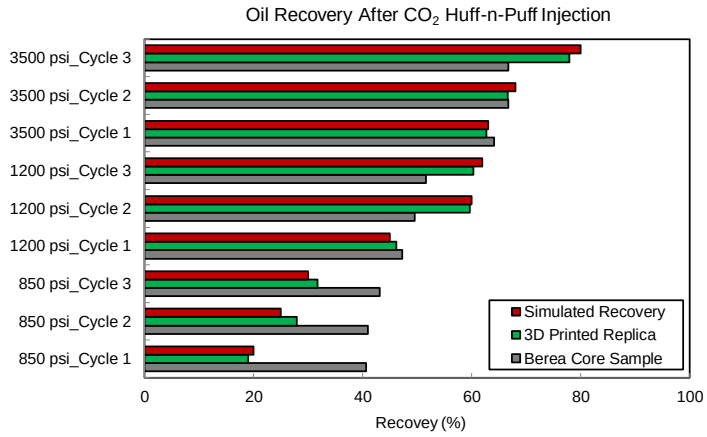

Figure 4.30: 2D view of the sliced 3D printed replica versus the simulated cross-sectional saturation distribution

4.5 Modeling MICP Experiment

The main premise in that paper was proving that using 3D printed rock replicas in oil and gas experimental research will enhance the modeling capabilities to match experimental results of physical samples. The replicas have the advantage of robustness, repeatability, and less geometrical and compositional uncertainties. Therefore, the generated processed and segmented Berea CT scan by MLIPT was used to simulate the MICP experiment to test this hypothesis numerically. A commercial digital rock physics (DPR) software was used to implement the MICP experiment flow conditions on the segmented connected pores shown in Figure 35. As confirmed by previous experiments, the sample has a considerable amount of non-connected and tiny pores, as shown in Figure 36**.** These pores are grouped into different classes based on their ranges and given different color codes. My applying finite element simulation on the fluid domain, Figure 37 shows the match and consistency in the MICP capillary curve between the simulated MLIPT segmented CT scan and 3D printed replica experimental results. On the other hand, manual segmentation did not match the actual behavior of the MICP experiment for the sample.

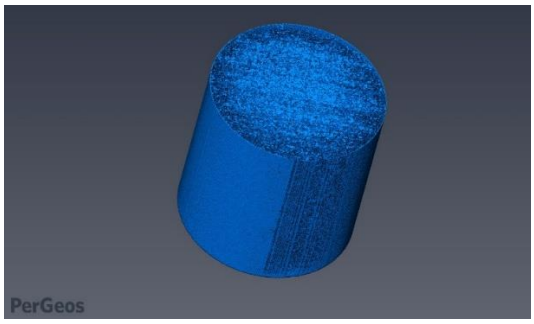

Figure 4.31 Modelling MICP experiment using manual and automated machine learning morphological segmentation

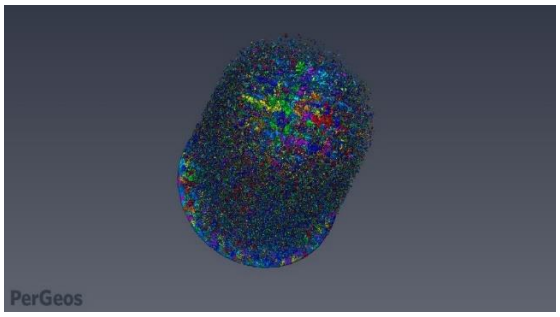

Figure 4.32 Segmented pores in the sample colored pores are grouped based on their connectivity and dimensions in PerGeos.

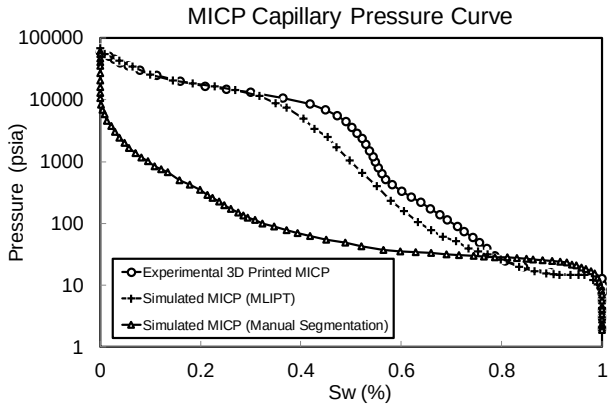

Figure 4.33 Modelling MICP experiment using manual and automated machine learning morphological segmentation

4.6 Conclusion

Accurate description and characterization, for core samples, is crucial to interpret corefloodings' responses, e.g., EOR. In this paper, CT scanning was used as a valuable base for characterizing core samples and simulating their coreflooding experiments. The following summarizes the presented workflow and outcomes:

- A detailed image processing approach was introduced to convert the CT scan grayscale slices to a porosity static model.
- Permeability was estimated using the Kozeny-Carman correlation from that porosity model.
- Then, the steps of constructing a gridding skeleton for the simulation model were detailed using Petrel software.
- 3D variograms enabled geostatistical populating the porosity and permeability data to the static model skeleton.
- Coreflooding experimental configurations of injection and production sources were integrated with the static model to generate a robust dynamic model for coreflooding experiments.

- After that, the finite difference formulation of single-phase flow was solved explicitly to acquire pressure distribution in the sample as a response for a similar injection schedule of the experiments.
- Two transient permeability experiments, i.e., Sinusoidal oscillating pressure wave and spike pulse decay, were selected to validate the CT scan processing workflow.
- Transient permeability experiments enabled investigating the ability of the model to capture the Berea sample's heterogeneities essence in the simulated pressure response.
- The CT-scan model succeeded in generating the recorded pressure response of the two experiments accurately with a correlation coefficient of 98% to 99%.
- Traditional approaches of porosity and permeability realization, based on single-value experimental measurement, underestimated the pressure in the sample in coreflooding simulation.
- Single-value statistical approach wrongly overestimated the pressure response also as the ignored local micro-heterogeneities profoundly affect the preferential flow paths and hence the dynamic response.
- The proposed CT scan realization approach enabled allocating these heterogeneities in the model, and it is highly recommended to accurately mimic samples' structure in numerical coreflooding simulations, especially for heterogeneous samples.

In this work, a CT-scanned Berea core sample was 3D printed after reconstructing its pore structure by image processing. The 3D printing process started with a resolution adaption of the CT scan to the 3D printers' requirements. Then, pores and grains were segmented to extract the solid printable volume. Finally, the virtual solid volume was triangulated to create the printable mesh. The mesh was 3D printed with Gypsum-based powder with a chemical binding. The printed replica had a close petrophysical properties to its original Berea sample. The Berea core sample and its replica were used simultaneously in a CO_2 huff-n-puff experiment. The experiment was conducted at three different pressures, 850, 1200, and 3500 psi with three injection/soaking/production cycles. The 3D printed replica was sliced laterally and longitudinally to visually investigate the CO_2 – hydrocarbon interaction inside the core. The purity of the 3D printed replica highlighted the CO_2 effects on the core interior and proved its value as a base for experimental research. 3D printed replicas are cheap to create and reduce the geometrical and material composition uncertainties.

A static simulation model was constructed to reflect the actual core architecture and its petrophysical properties. The porosity cloud was generated by binarizing the upscaled CT scan. The porosity model was constructed by geostatistically populating the CT-porosity to the model. The permeability model was inferred from the porosity model using Kozeny-Carman model. Fluid model was defined by PR EOS for Bakken oil. The CO_2 huff-n-puff experiment was simulated dynamically as CO_2 gas aquifer conform the model from all sides and its pressure was scheduled as the CO_2 injection pressure during the experiment. The model succeeded to generate same saturation distribution of the replica interior after the experiment and matched its oil recovery. The presented work of 3D printing ideal core replicas and building precise coreflooding simulation models for them will advance the experimental research of fluid flow physics because of its accurate characterization of the understudy system.

5 3D Printing Replication of Porous Media for Future Lab-Scale Petrophysical Characterization Research

Simplifying the physics of fluid flow in conventional reservoirs is convenient by assuming uniform lithology and system-geometry with minimal rock/hydrocarbon interactions. In unconventional reservoirs, such simplification restrains mathematical models' ability to simulate the actual flow behavior and production performance. Precise adaption for the physics of fluid flow in porous media can be achieved if the system understudy is geometrically characterized appropriately, and there are minimal interactions indeed. 3D-printed replicas of porous-rock samples obey this criterion. Image processing tools were used for creating presentable porous and permeable replicas of different scales and configurations of the petroleum system from lab-scale to field-scale. The workflow of 3D-printed replicas creation is presented for replicas of conventional core samples, naturally and synthetically fractured cores, geological drilling units of multistage fractured horizontal wells, and full-field models, e.g., Norne field in Norway. These samples are ideal for experimentally testing the validity of the analytical or numerical models of oil and gas reservoirs in the laboratory, along with judging the quality of reservoirs' characterization. The ideality of these replicas is a result of the limited uncertainties of the understudy-system geometry and fluid/rock interactions because of the uniform composition. For validation purposes, 3D-printed replicas with different materials and 3D-printing technologies were created based on a reconstructed image-proceed CT scan of their original Berea sandstone. These replicas were tested for storage capacity (Porosity) and transport capacity (Permeability) and compared with their original sample's capacities. The matched results proved the ability of 3D replicas to be used in oil and gas laboratory experimental research.

5.1 Introduction

Experimental research, in the oil and gas industry, is crucial to estimate hydrocarbon reserves and to develop their optimal exploitation strategies [138]. Fluid-flow and characterization experiments, e.g., core flooding, porosity, permeability, and wettability experiments, etc., are conducted on samples acquired from subsurface reservoirs [139]. Those experiments reflect the fluid-rock interactions in the subsurface, and their results are used to build representative mathematical models, numerical or analytical, to predict reservoirs' future performance [97]. The effectiveness of potential enhanced oil recovery (EOR) technology is also tested experimentally on core samples from the reservoir before the expensive field-implementation [140]. Laboratory experiments are conducted under similar conditions to downhole/reservoir insitu conditions, i.e., injection pressure, reservoir temperature, normal stresses, and fluid composition. Under such conditions, acquired attributes like oil recovery, decline rates, pressure changes, and fluid composition changes enhance understanding the reservoir nature and its response to production mechanisms [141].

Numerical and analytical models are used to predict reservoirs' future performance after accurate characterization and validation versus core-scale lab-results [142]. The fundamental challenge to validate such models is characterizing rock/fluid interactions for samples with spatially-varying rock mineralogy and complex flow geometry [59]. Complicated models have been developed to accurately simulate fluid flow in porous media to its finest complexity scale, i.e., Micro and Nanoscale [53]. These models failed to handle complex interactions and/or complex geometries because of the limitations on

computational power and the issues of convergence and stability of the mathematical solution [143]. Even the perfect-matching models, among them, have nonquantifiable uncertainties due to the existence of too many controlling variables, e.g. pore network configuration, the physical boundaries of the system, and governing equations' assumptions [144]. Therefore, geo-modelers tend to simplify the system complexities, geometrical and/or compositional, to have usable models for lab- and field-scale systems [145]. Petrophysical properties' upscaling is an example of models' simplification, which eases models' utilization [64]. Assuming minimal spatial-variabilities and interactions can be useful for simulating experiments on samples from conventional reservoirs and can generate reliable results [64]. For unconventional reservoirs, such simplifications cannot be trusted where system complexity is nonnegligible and controls the system behavior [146].

3D-printers are capable of creating complicated designs effectively with minimal waste and flaws [147]. Wide applications of 3D-printing are presented recently in fundamental research areas, e.g., multiphase fluid flow, geomechanics, paleontology, geomorphology [148][149][4][150][107][151][103]. The usage of 3D-printing technology stimulated researchers in the petroleum engineering and geoscience fields [152]. Applications of 3D-printing are signified by its capability of translation of virtual models into 3-D printed specimens for experimental research [9][16]. 3D-printing technology was used to create ideal porous specimens from the lab- to field-scale petroleum systems to overcome their geometrical and compositional complexity challenge [103] [102]. Image-processing tools were developed for manufacturing physically tangible replicas of petroleum systems based on their reconstructed conceptual models, e.g., a reconstructed core CT scan or seismic field data [16]. The advantages of manufacturing 3D-printed replicas of core samples and full-field models are multifold. These advantages are:

1. Numerical models of experiments, which are conducted on the 3D-printed Replicas, have minimal geometrical uncertainties as these models will be created based on the same geometrical mesh that will be used in the 3D-printing process itself.
2. 3D-printed replicas eliminate the uncertainties of rock/fluid interactions because of the uniform composition of the 3D-printing materials, e.g., plastics or gypsum, which enables quantifying the interaction with hydrocarbons in the simulation models accurately.
3. 3D-printed replicas reduce the cost of destructive experiments as these synthetic samples have the advantage of cheap 3D-printing repeatability and preserving expensive original samples.
4. 3D-printing enables inserting syntactic or natural fractures inside the specimen to simulate fracture-matrix flow physics experimentally.
5. Unconsolidated rock samples can be 3D-printed to create replicas which can persist firmly extreme pressures during coreflooding experiments.
6. 3D-printing enables creating downscaled lab-scale pilot or full-field models that are physically unattainable to acquire form subsurface to test in the laboratory.

The following cases present the capabilities of image processing tools and 3D-printing technology to create and tailor synthetic specimens of cores and downscaled pilot/full-field models in reasonable dimensions for laboratory experiments.

5.2 3D-Printing Conventional Cores Using Different Materials & Printing Technologies

Standard commercial Berea sandstone core (1.5 inches in diameter and 2 inches in length) was 3D-printed after building its virtual 3D-printable object (Figure 1). The Berea sample was CT-scanned, and its CT scan was image-processed to segment Berea's grains/pores into two separate classes. The grains class represented the solid volume to be 3D-printed and create the synthetic replica. The image processing and segmentation steps are:

A. Adapting the CT scan's areal and longitudinal resolution to match the resolution limitations of 3D-printers on objects details and also reduce processing memory requirements, the adaption process is conducted by upscaling the number of pixels per each CT slice along with 3D interpolation to fill the gaps between the CT slices [16].
B. Segmenting grains/pores geometrical domains in the scan using a definite grayscale threshold which separates the pores' pixels from the grains' ones [153]
C. Meshing the grains' segmented pixels to construct a 3D continuous object which can be 3D-printed in a stereolithography format (.stl file) [102]
D. Slicing the 3D object to a sequence of intersection horizontal-layers to be 3D-printed one by one by the 3D-printer to construct the replica [105]
E. 3D-printing the sliced 3D object using different 3D-printing materials and technologies, as shown in Figure 2

Figure 2 shows the 3D-printed replicas with different printing materials such as common white and transparent plastic PLA; Polylactic Acid, CPE; Co-Polyester, ABS, Acrylonitrile Butadiene Styrene, transparent resins, and colored sandstone [154]. Each material has its well-documented mechanical and texture properties [155] [156][157]. The used material is selected based on the purpose of 3D-printing, the operating conditions of the experiment (pressure and temperature), the complexity of the model, and the maximum required resolution [25]. Five 3D-printers were used with four different 3D-printing technologies, i.e., Fused Filament Fabrication (FFF); Ultimaker 3D-printer, Fused deposition modeling (FDM); Prusa I3 and Stratasys, Photo-polymerization technology Stereolithograph (SLA); Formlabs, and Powder Deposition/Lamination 3D-printing technology; ProJet 660 [158][157]. In both FFF and FDM 3D-printing technologies, a thick string of raw filament material is extruded through a heated nozzle. That nozzle is controlled by a motion system to track the object details. Melted filament is deposited and solidifies to form the 3D-printing layers, one by one. In the SLA technology, a laser beam is used to cure liquid photo-polymer resin into solid according to the object geometry. Finally, deposition 3D-printing technology uses a selective of silica or gypsum powder and a jetting-binder material to build the object geometry layers.

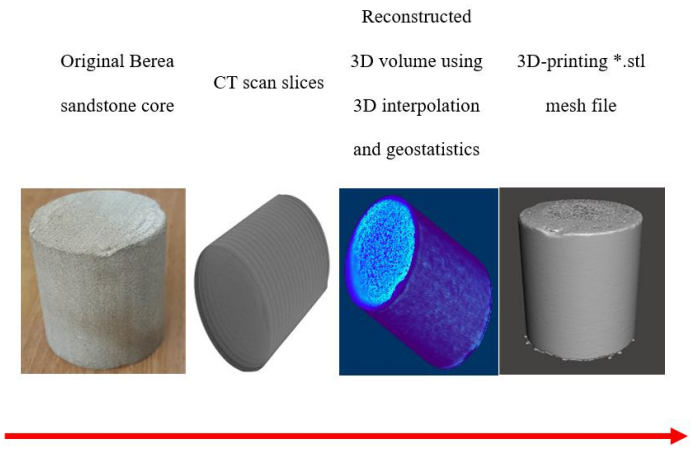

Figure 5.1: Berea core sample's replicas 3D-printing steps

Material:	White PLA	White PLA	Transparent PLA	Transparent CPE	ABS	Black PLA	Transparent Resin	Sandstone
3D-printer:	Stratasys	Ultimaker	Ultimaker	Ultimaker	Ultimaker	Prusa I3	Formlabs	ProJet 660

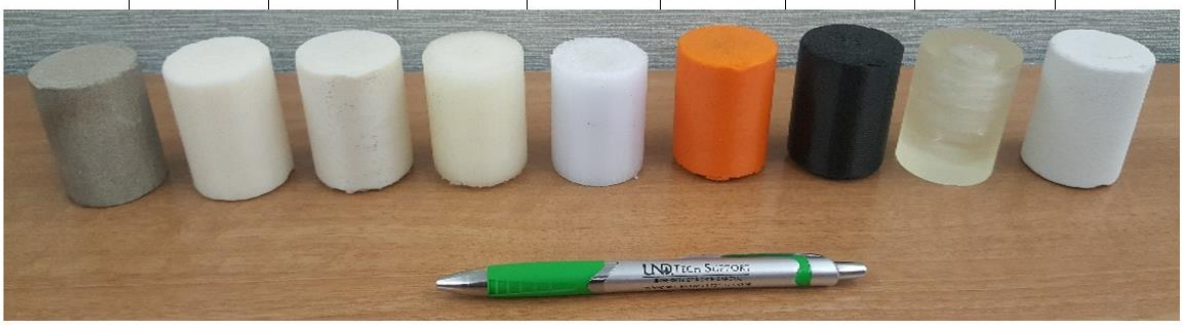

Figure 5.2: 3D-printing porous and permeable synthetic core samples replicating original core sample (Berea sandstone) with different materials and 3D-printing technologies

The quality of 3D-printing differs from a technology to another and even from one 3D-printer model to another with the same printing technology [157]. Porosity and permeability were measured and listed for all samples in Table 1 to compare the original's static and dynamic properties with 3D-printed replicas' properties. The measurements show that transparent resins and colored-sandstone replicas have closer hydraulic behavior to their original properties. 3D-printing with plastics (BLA or ABS) resulted in low permeabilities as the plastic-printing material melted during the printing process and plugs pores. Figure 3 highlights the significance of 3D-printing in petroleum and geoscience research. The proposed image-processing workflow showed its significance experimentally by the usage of the created colored-sandstone replica in a CO_2 huff and puff experiment. Considering it's low-cost to create another replica, CO_2 effects on the core interior were investigated visually after splitting the replica laterally and longitudinally without destroying the natural Berea core. The importance of the workflow in fluid flow in porous media was realized by using the segmented pores field form the CT scan was utilized to build a precise compositional simulation model for the CO_2 huff and puff experiment (Figure 3). Finally, the

segmented grains field was used to construct a geomechanical simulation model to simulate the uniaxial compression strength (UCS) test. The printed replicas are 1.5-inch in diameter and 2-inch long. These dimensions can fit the size requirements of a coreflooding setup. For other experiments, size requirements are different in diameter and length. The proposed image processing workflow and 3D-printing technology can be used to tailor the dimensions of the sample. That tailoring will preserve the original cores and avoiding wasting them by resizing them for another set of experiments. In the next section, resizing a CT scan will be explained to create smaller samples without damaging original cores.

Table 5.1: Petrophysical Properties for Original and 3D-Printed Core Samples

	Material	3D-Printer	Por. (%)	Perm. (md)
	Original core		20	100
1	PLA	Stratasys	18	150
2	PLA	Ultimaker	25	70
3	Transparent PLA	Ultimaker	26	75
4	Transparent CPE	Ultimaker	28	80
5	ABS	Ultimaker	15	60
6	PLA	Prussia I3	12	62
7	Transparent Resin	Formlabs	23	96
8	Sandstone	ProJet 660	22	110

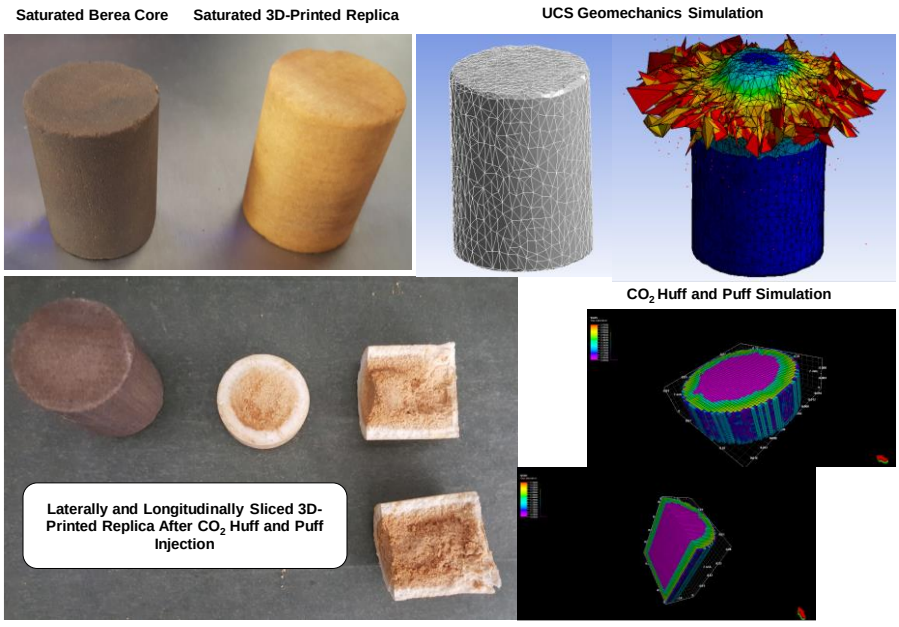

Figure 5.3: Applications of 3D-printed core replicas in experimental research, fluid flow simulation in porous media, and geomechanics modeling

5.3 3D-Printing Tailored and Resized Core Samples' Replicas

Nitrogen-adsorption measurement requires samples of 1 inch in diameter and 1 inch in length [42][47]. In contrast, tri-axial geomechanics- and transient permeability measurements require samples 1 inch in diameter and 2 inches in length [74]. So, Berea sample, of 1.5 inches in diameter and 2 inches in length, cannot be used to conduct such experiments. Other Berea samples can be acquired to proceed with the experiments, but that will lead to inconsistent results because of samples' different pore network structure and mineralogy. The appropriate solution is to resize the sample to the new dimensions. The two possible means of samples' resizing are:

A. Resizing the core mechanically, and
B. Resizing the CT scan digitally using image processing and then 3D-print the new reconstructed object

The mechanical method is not preferred due to the probable damage and the possibility of losing the sample. Therefore, it is preferred to resize the CT scan digitally by image processing. To resize the diameter of the sample, the original CT-scan images/slices can be cropped to the required new diameter by trimming the pixels outside the area of interest. As an example, Figure 4 shows a CT slice cropped from 1.5-inch to 1-inch diameter. On the other hand, resizing the scan in length can be conducted by removing the redundant CT slices from the original scan, as shown in Figure 5 (a, b, and c). After fitting the CT scan to the desired size, the continuous conceptual models, shown in Figure 5 (d, e, and f), are reconstructed. Finally, those models are 3D-printed with different materials (colored sandstone, PLA, ABS, Resin), as shown in Figure 6. The proposed process saves the manual efforts, sampling expenditure, and experiments' time of lab-work by providing as many samples as needed with suitable configurations once the CT scan of the original sample is acquired.

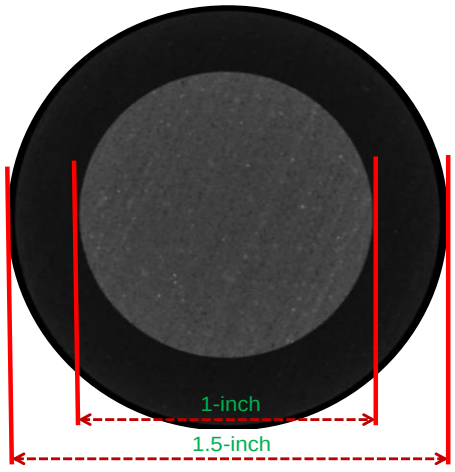

Figure 5.4: Cropping 1.5-inch diameter CT scan slice to 1-inch in diameter

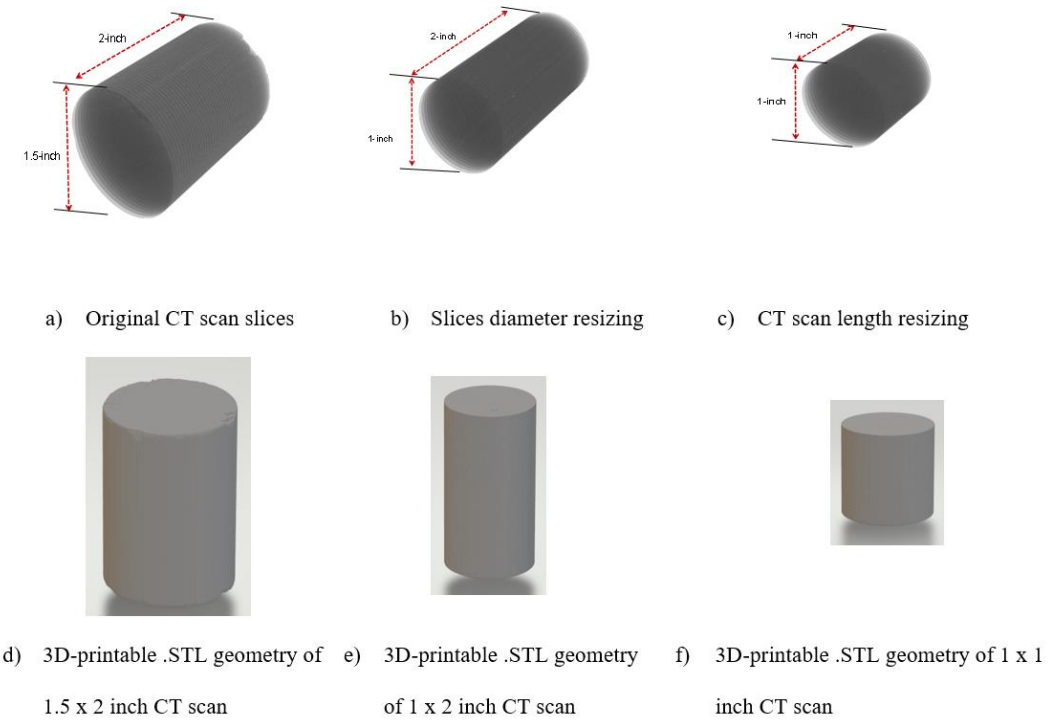

Figure 5.5: Resizing the original CT scan in length and diameter

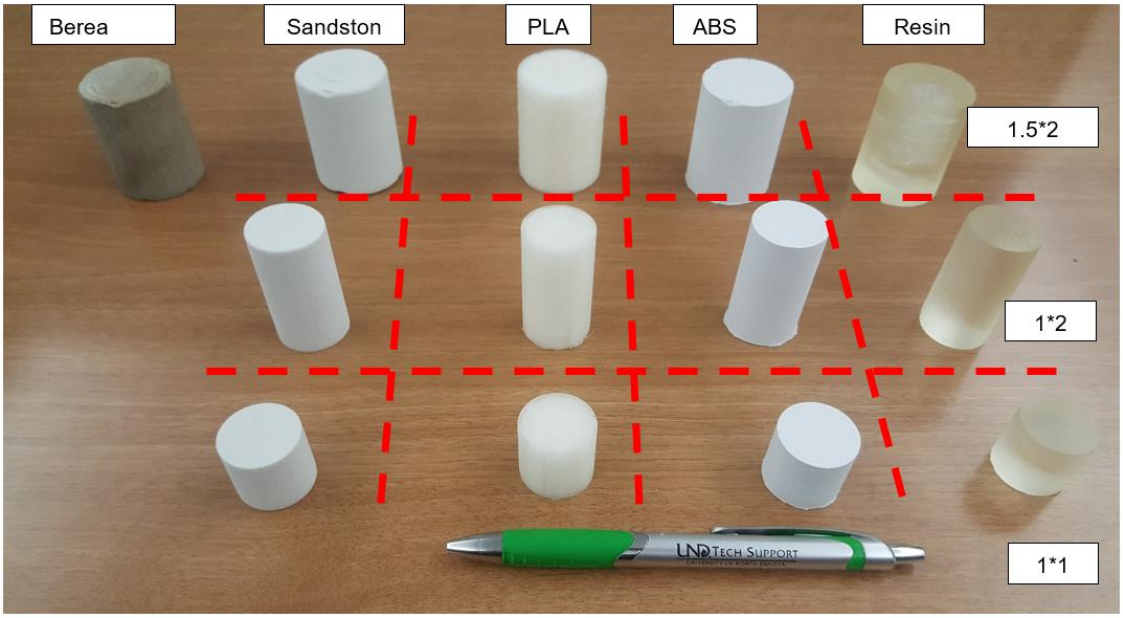

Figure 5.1: 3D-Printing resized image processed CT scan with different materials (Colored Sandstone, PLA, ABS, Resin) [166]

5.4 3D-Printing Naturally and Synthetically Fractured Core Samples

The flow physics of matrix/fractures are not fully understood yet because of the limited conducted experiments. For instance, naturally fractured rocks are fragile and rupture under the applied friction stresses and heat of the coring process [159]. Another characterization issue, to extensively describe

their physics, is referred to the deficiency in describing the matrix/fractures system geometrically. The proposed image-processing methodology can be extended to 3D-print cores with such complex geometry, i.e., cores with natural fissures. 3D-printing facilitates experimental research on naturally-fractured samples and makes it possible and more practical. Figure 7 compares synthetic sections produced from Berea sandstone (conventional core; left) and a section 3D-printed from a core which includes vugs and fissures (right).

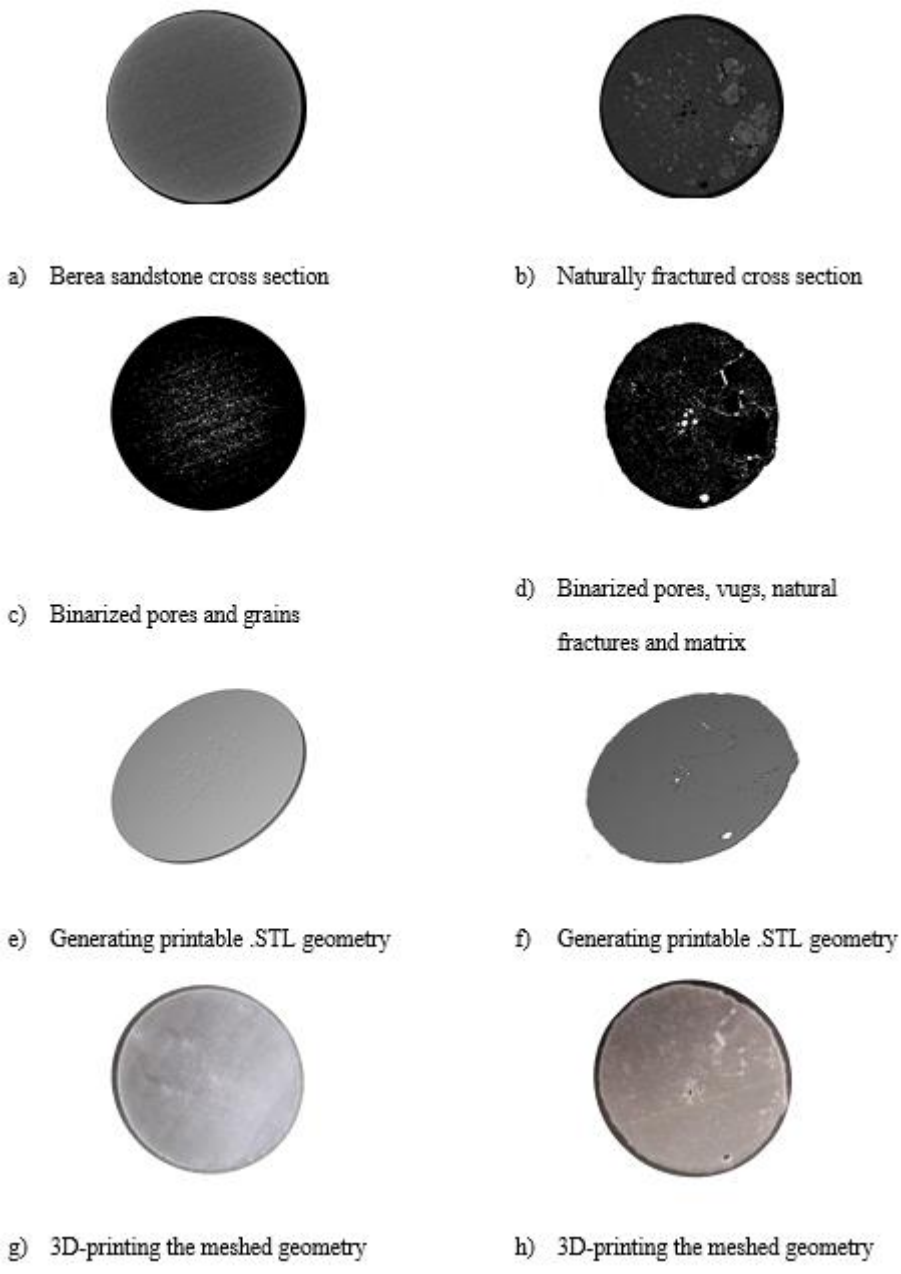

Figure 5.7: Creating 3D-printable cores with natural fractures compared with conventional cores

Experimental research, on cores with synthetic fractures, is important to study failure modes and flow physics of field-hydraulic fracturing operations. Artificial inclusion of cracks, inside natural core

samples, is challenging if impossible. The proposed image processing workflow enables a precise insertion of synthetic fractures to the CT scan and 3D-print the processed object to study the stress-strain geomechanical behavior, e.g., fatigue planes, during an injection experiment. The steps of the workflow (Figure 8) are:

1. Selecting the CT slices, where the fracture is encompassed intentionally.,
2. Overlaying the fracture geometry (aperture, profile, and width) on the CT slices,
3. Removing the pixels of the fracture geometry from the scan set,
4. Constructing the meshed 3D-structure (i.e. *.stl file), and
5. 3D-printing the resulted object with proper printing material and technology

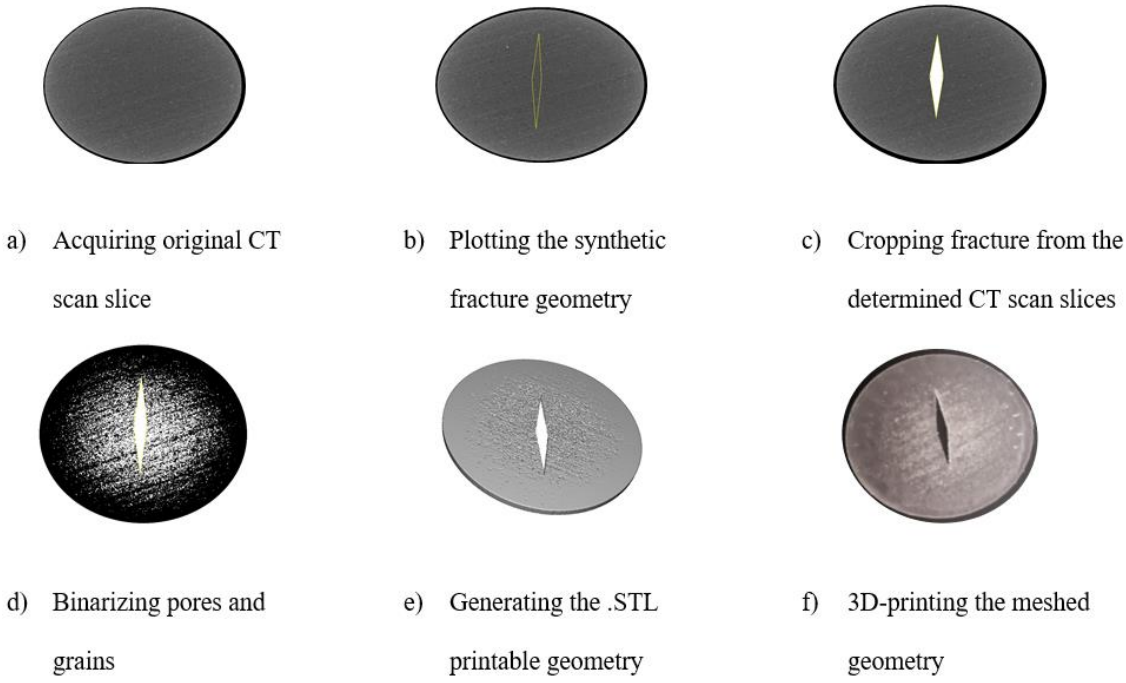

Figure 5.8: Creating 3D-printable cores with synesthetic fractures

5.5 3D-Printing Prototype of Drilling Units Pilot Model

Up till today, there is no published literature regarding experimental research on downscaled pilot models [160]. Most feasibility studies, on pilots, were based on a field application or simulation studies [161]. 3D-printing enables creating a tangible pilot model for lab-scale experiments. The printed pilot-replicas can be used to physically study the reactions of stimulated reservoir volumes (SRVs) to any recovery strategy and support analytical/numerical models experimentally. Different models, for a multistage-fractured horizontal well (MSFHW), were created from virtual cross-sections, which includes a well path, porous media, natural fractures, and different hydraulic fractures geometries in the SRV. These models can save ineffective strategies' field expenditures by facilitating conducting sensitivity experiments for testing different EOR/development plans before implementing them in the field. Various combinations of a reservoir (homogenous, naturally fractured, tight, and conventional), well (vertical, horizontal, slanted, and fractured), and hydraulic fractures (transverse, longitudinal, and

complex branches) can be geometrically designed. Figure 9 and Table 2 show the steps of generating printable pilot models for four cases with different well/reservoir configurations. The steps are:

1. Plotting a 2D geometry of a cross-section of the system,
2. Segmenting the grayscale solid-domain from pore's one as followed for segmenting a CT-scan slice,
3. Extruding as many slices as needed to cover the SRV's 3D-volume,
4. Building the continuous conceptual volume to be meshed, and
5. 3D-printing the pilot model in proper dimensions for lab-testing

Matrix porosity can be gained from the porosity of the printing material, i.e., sandstone silica/gypsum powder, or by artificial insertion of pore space. This local porosity and permeability should be downscaled from a reservoir-scale to lab-scale for each volumetric unit. A useful application of 3D-printing pilot models is studying stress changes and their implications, e.g., subsidence and changes of hydraulic fractures' configurations. Basins' subsidence rates have been widely investigated for oil and gas reservoirs [162][163]. Such studies were not experimentally investigated on a laboratory scale. Downscaled 3D-printed pilot models accommodate specimens to study the impacts of field-scale attributes on the reservoir system. Figure 10 shows a geomechanical model to study insitu stresses changes effects on the fractures dimensions, which can be validated experimentally with a 3D-printed pilot model in Table 2.

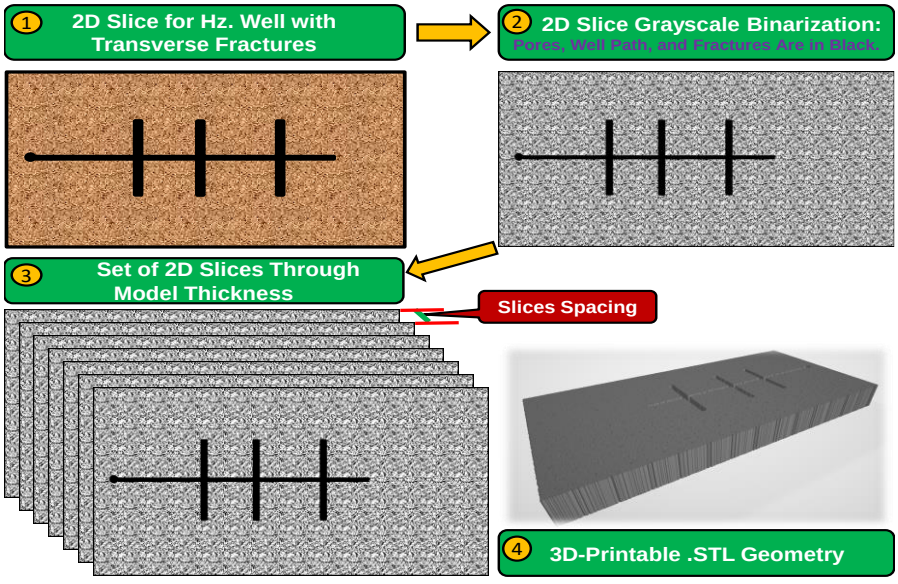

Figure 5.9: Generating 3D-printable .STL geometry steps for the analytical pilot model

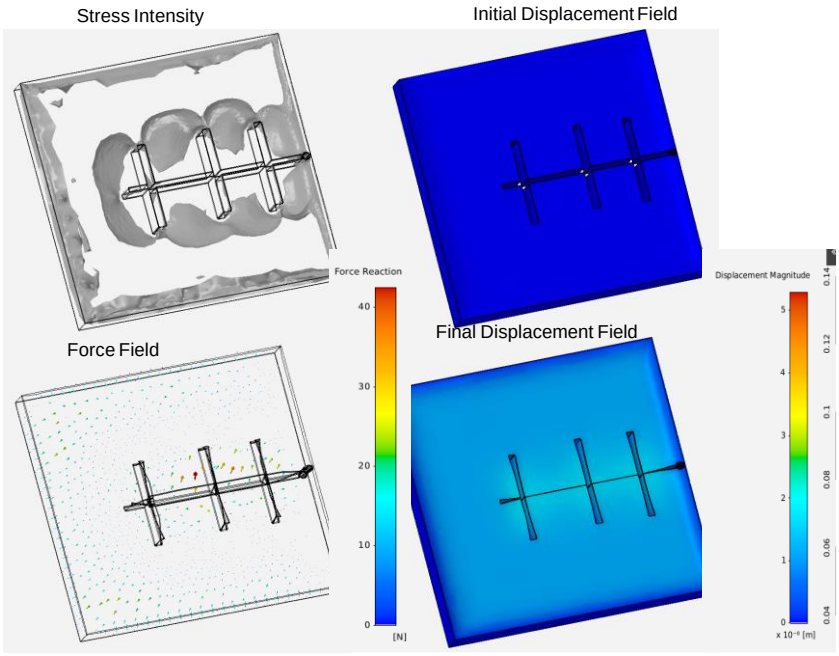

Figure 5.10: A geomechanical model to study insitu stresses changes effects on the fractures dimensions

Table 5.2: Steps of creating four different geometrical combinations (well, fractures, and reservoir) of 3D-printable pilot model of a multistage hydraulically fractured horizontal well

	2D Geometrical Configuration	*.STL Printable Geometry	3D-Printed Geometry
A) horizontal well with transverse fractures * porosity from 3D-printing material	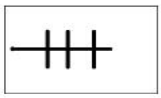	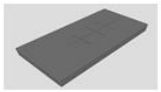	
B) horizontal well with transverse fractures * porosity from the system porosity		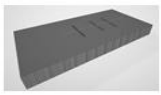	
C) horizontal well with complicated fractures branches * porosity from 3D-printing material	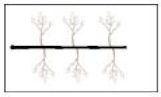	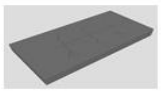	
D) horizontal well with transverse fractures in a naturally fractured system * porosity from 3D-printing material and the natural fractures network	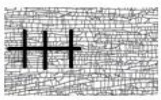	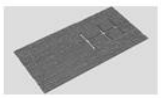	

5.6 3D-Printing a Lab-Scale Replica for A Full-Field Model

3D-printing also enables full-field studies of production mechanisms and EOR processes in a lab-scale. For any EOR technique, flooding fronts can be physically monitored, streamlines can be tracked and visualized, and sweep efficiency can be quantified experimentally on full-field 3D-printed prototypes. Downscaled static models will be a base for 3D-printing porosity, permeability, and boundaries transmissibilities, e.g., sealing faults and reservoir limits. The E-Segment of Norne field, in the Norwegian Sea; Heidrun oil field, is examined, and its static model is processed from seismic data [164][165]. The downscaled static is then 3D-printed by following the workflow summarized below (Figure 11 and Figure 12):

1. Acquiring the geologic model's attributes, e.g., reservoir boundaries, porosity, and permeability from seismic data, well logs, etc.
2. 2D Slicing the porosity static model to generate a set of 2D slices to be image processed, i.e., digitally binarized, as CT scan slices
3. Cartesian meshing the reservoir's horizons and surfaces to obtain corner-point nodes to track the outer boundaries of the 3D-printing model accurately
4. Triangulating the reservoir's Cartesian mesh, as 3D-printable objects' surfaces should be defined by triangular facets (see Figure 12)
5. Resizing the global dimensions of the mesh with a reasonable aspect ratio, Figure 13 shows the 3D-printed E-Segment of Norne field printed in three different sizes.
6. Geostatistically populating a virtual cloud of 3D solid spheres to generate artificial porosity and permeability inside the printable volume or 3D-printing a solid volume and count on the approximate printing-material's porosity and permeability

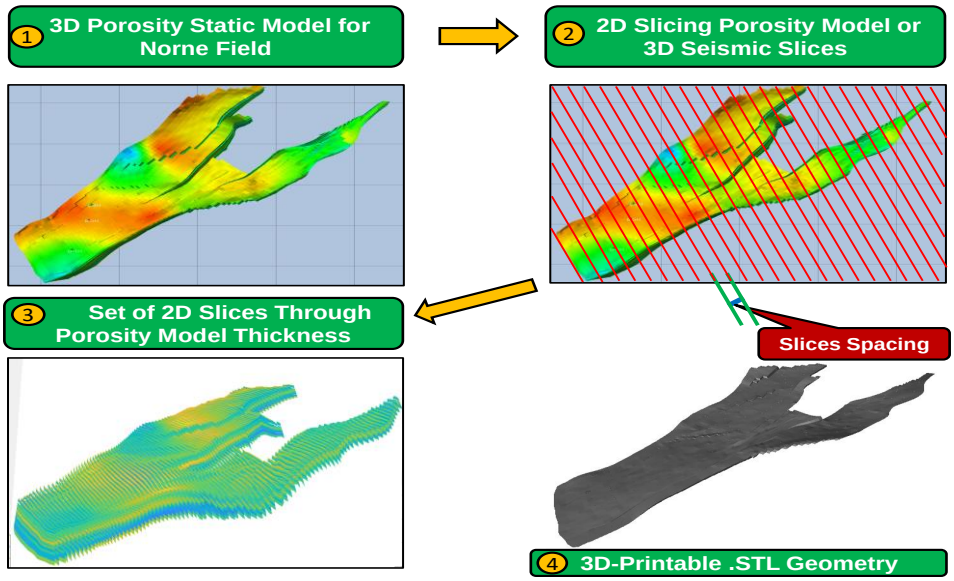

Figure 5.11: Steps of using 3D porosity static model slices or 3D seismic survey slices to generate 3D-printable .STL geometry for a full field model, e.g., E-Segment of Norne field in the North Sea

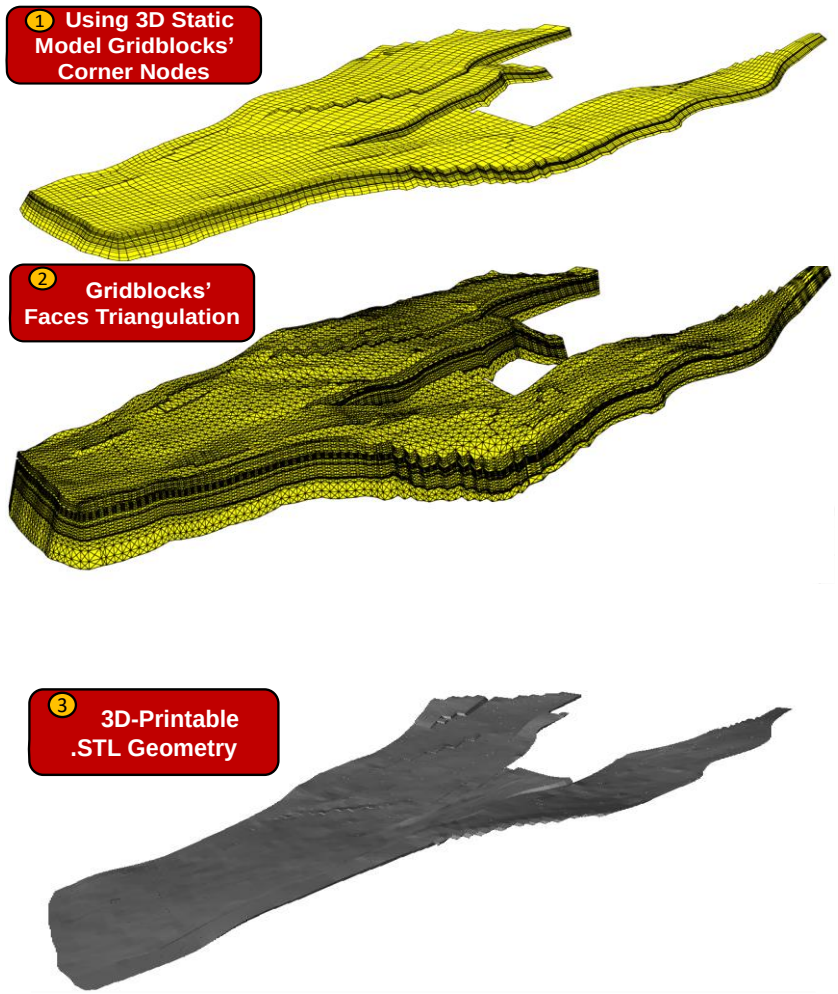

Figure 5.12: Triangulation of Cartesian corner nodes of the static model to generate 3D-printable .STL geometry for a full field model, e.g., E-Segment of Norne field in the North Sea [166]

Figure 5.13: 3D-Printing the meshed geometry of E-Segment of Norne field in the North Sea in three different sizes [166]

5.7 Conclusions and Recommendations for Future Work

Image processing and 3D-printing technology facilitate reconstructing and tailoring specimens for experimental research and modeling validation of the physics of fluid flow in petroleum systems. Along with the sizing flexibility, 3D-printed samples reduce the geometrical and lithological uncertainties of real rock samples with quantifiable rock-fluid interactions. Such simplifications, in subsurface complexities, advance and ease the development of precise analytical/numerical fluid flow formulations. An image processing workflow is proposed to create 3D-printable porous and permeable specimens for laboratory experiments. The processing steps were explained for reconstructing the acquired CT-scan slices by binarizing the grayscale slices and segmenting pores from grains. Cropping and resizing the CT scan is presented as another beneficial image-processing application that overcame samples' resizing challenge, i.e., physical damage of mechanical resizing, to fit different size requirements of various experiments. The ability to reevaluate matrix/fractures flow physics experimentally is enabled by the image processing approach of synthetic fractures insertion in a CT scan, and 3D-print fractured replicas. The workflow of 3D-printing conventional core samples or synthetically/naturally fractured ones was used to 3D-print full-field models and pilot models of different combinations of well-reservoir configurations. Cases of multistage-fractured horizontal wells in naturally fractured SRVs were 3D-printed. Static seismic data and artificial cross-sections were treated as CT slices to 3D-print pilot and full-field models. On the 3D-printed models, analytical and numerical models of recovery mechanisms, e.g., EOR, can be tested and validated experimentally. The 3D-printed core samples were created with different materials and printing technologies. The petrophysical properties, i.e., porosity and permeability, of the replicas were measured and matched its original Berea's properties.

To boost the benefits of the technology of 3D-printing in oil and gas industry research, it is highly recommended that the 3D-printers' manufacturers develop their technology to:

1. Reduce resolution limitations to facilitate 3D-printing tight rocks with smaller pore throats
2. Increase physical-dimensions' limitations to enable 3D-printing full-field models with larger dimensions
3. Adapt 3D-printers to print with natural materials, e.g., sandstone grains, not only with synthetic ones
4. Enable multi-material printing in which actual hydrocarbon material can be implanted inside the model
5. Increase the mechanical stability of the 3D-printing materials to hold extreme conditions of high pressure and temperature
6. Increase the chemical stability of the printing materials to avoid any interaction with the used experimental fluids

References

[1] Y. Ju, L. Wang, H. Xie, G. Ma, Z. Zheng, L. Mao, Visualization and Transparentization of the Structure and Stress Field of Aggregated Geomaterials Through 3D Printing and Photoelastic Techniques, Rock Mech. Rock Eng. 50 (2017) 1383–1407. https://doi.org/10.1007/s00603-017-1171-9.

[2] M.J. Blunt, Multiphase Flow in Permeable Media: A Pore-Scale Perspective, Cambridge University Press, Cambridge, 2017. https://doi.org/DOI: 10.1017/9781316145098.

[3] L. Kong., M. Ostadhassan., C. Li., N. Tamimi., Rock Physics and Geomechanics of 3-D Printed Rocks, 51st U.S. Rock Mech. Symp. (2017) 8. https://doi.org/.

[4] S. Ishutov, F.J. Hasiuk, 3D Printing Berea Sandstone: Testing a New Tool for Petrophysical Analysis of Reservoirs, Petrophysics. 58 (2017) 592–602. https://doi.org/.

[5] S. Peng, Q. Hu, S. Dultz, M. Zhang, Using X-ray computed tomography in pore structure characterization for a Berea sandstone: Resolution effect, J. Hydrol. 472–473 (2012) 254–261. https://doi.org/https://doi.org/10.1016/j.jhydrol.2012.09.034.

[6] E.S. Amirtharaj, M.A. Ioannidis, B. Parker, C.D. Tsakiroglou, Statistical Synthesis of Imaging and Porosimetry Data for the Characterization of Microstructure and Transport Properties of Sandstones, Transp. Porous Media. 86 (2011) 135–154. https://doi.org/10.1007/s11242-010-9612-x.

[7] B. Bera, S.K. Mitra, D. Vick, Understanding the micro structure of Berea Sandstone by the simultaneous use of micro-computed tomography (micro-CT) and focused ion beam-scanning electron microscopy (FIB-SEM), Micron. 42 (2011) 412–418. https://doi.org/10.1016/J.MICRON.2010.12.002.

[8] P.L. Churcher, P.R. French, J.C. Shaw, L.L. Schramm, Rock Properties of Berea Sandstone, Baker Dolomite, and Indiana Limestone, SPE Int. Symp. Oilf. Chem. (1991) 19. https://doi.org/10.2118/21044-MS.

[9] A.G. Almetwally, H. Jabbari, CT-Scan Image Processing for Accurate Pore Network Modeling and Core Samples 3D Printing: Polynomial Interpolation & Geostatistical QC, 53rd U.S. Rock Mech. Symp. (2019) 8. https://doi.org/.

[10] N. Keat, X-ray CT, ImPact Group., (2002). http://www.impactscan.org/slides/xrayct/index.htm.

[11] NIBIB: National Institute of Biomedical imaging and Bioengineering, Computed Tomography (CT), 2018. (n.d.). https://www.nibib.nih.gov/science-education/science-topics/computed-tomography-ct.

[12] L.W. Goldman, Principles of CT: Radiation Dose and Image Quality, J. Nucl. Med. Technol. 35 (2007) 213–225. https://doi.org/10.2967/JNMT.106.037846.

[13] S.A. Hertel, M. Rydzy, B. Anger, S. Berg, M. Appel, H. de Jong, Upscaling of Digital Rock Porosities by Correlation With Whole Core CT Scan Histograms, SPWLA 59th Annu. Logging Symp. (2018) 10. https://doi.org/.

[14] and E.W. Fisher R., S. Perkins, A. Walker, Pixel Values, (2003). https://homepages.inf.ed.ac.uk/rbf/HIPR2/value.html.

[15] T. Grimm, User's Guide to Rapid Prototyping, Society of Manufacturing Engineers, 2004. https://books.google.com/books?id=o2B7OmABPNUC.

[16] A.G. Almetwally, H. Jabbari, Development of Novel Workflow to Replicate Pore Network of Porous Core Samples Through 3D Printing Technology, 53rd U.S. Rock Mech. Symp. (2019) 8. https://doi.org/.

[17] J. Sachs, Image resampling, (2001). http://www.dl-c.com/Temp/downloads/Whitepapers/Resampling.pdf.

[18] J. Summers, Basics of image resampling, (2012). https://entropymine.com/imageworsener/resample/.

[19] and H.O. Touati, M., S. Siddiqui, T. Mostafa, Geostatistical analysis and classification of individual core sample data, (2008). https://patents.google.com/patent/WO2009058390A1/en#citedBy.

[20] T.M. Lehmann, C. Gonner, K. Spitzer, Survey: interpolation methods in medical image processing, IEEE Trans. Med. Imaging. 18 (1999) 1049–1075. https://doi.org/10.1109/42.816070.

[21] P. and R.M. Rajarapollu, Bicubic interpolation algorithm implementation for image appearance enhancement, 2017. (n.d.). www.ijcst.com. 8. 23-26.

[22] H. Wackernagel, Multivariate Geostatistics, Springer Verlag, Berlin, Heidelberg, 2003.

[23] Matheron G., Principles of Geostatistics, Economic Geology, 1963. https://doi.org/58 (8): 1246-1266.

[24] A. Tripathy, A. Kumar, V. Srinivasan, K.H. Singh, T.N. Singh, Fractal analysis and spatial disposition of porosity in major indian gas shales using low-pressure nitrogen adsorption and advanced image segmentation, J. Nat. Gas Sci. Eng. 72 (2019) 103009. https://doi.org/10.1016/J.JNGSE.2019.103009.

[25] L.C. Hwa, S. Rajoo, A.M. Noor, N. Ahmad, M.B. Uday, Recent advances in 3D printing of porous ceramics: A review, Curr. Opin. Solid State Mater. Sci. 21 (2017) 323–347. https://doi.org/10.1016/J.COSSMS.2017.08.002.

[26] J. Goral, I. Walton, M. Andrew, M. Deo, Pore system characterization of organic-rich shales using nanoscale-resolution 3D imaging, Fuel. 258 (2019) 116049. https://doi.org/10.1016/J.FUEL.2019.116049.

[27] R. Caselli, B. Forte, Image Segmentation by Minimum Information Loss BT - Proceedings of the Fourth European Conference on Mathematics in Industry, in: H. Wacker, W. Zulehner (Eds.), Springer Netherlands, Dordrecht, 1991: p. 235. https://doi.org/10.1007/978-94-009-0703-4_24.

[28] D.M. Rizzo, D.E. Dougherty, Artificial Neural Networks in Subsurface Characterization BT - Artificial Neural Networks in Hydrology, in: R.S. Govindaraju, A.R. Rao (Eds.), Springer Netherlands, Dordrecht, 2000: pp. 111–134. https://doi.org/10.1007/978-94-015-9341-0_7.

[29] S. Misra, H. Li, J. He, Machine Learning for Subsurface Characterization, Elsevier Science, 2019. https://books.google.com/books?id=IYQTvgEACAAJ.

[30] I. Arganda-Carreras, V. Kaynig, C. Rueden, K.W. Eliceiri, J. Schindelin, A. Cardona, H. Sebastian Seung, Trainable Weka Segmentation: a machine learning tool for microscopy pixel classification, Bioinformatics. 33 (2017) 2424–2426. https://doi.org/10.1093/bioinformatics/btx180.

[31] R. Xu, M. Prodanović, Effect of pore geometry on nitrogen sorption isotherms interpretation: A pore network modeling study, Fuel. 225 (2018) 243–255. https://doi.org/10.1016/J.FUEL.2018.03.143.

[32] B. Yenilmez, M. Temirel, S. Knowlton, E. Lepowsky, S. Tasoglu, Development and characterization of a low-cost 3D bioprinter, Bioprinting. 13 (2019) e00044. https://doi.org/10.1016/J.BPRINT.2019.E00044.

[33] 3D Systems, VisiJet ® PXL Material, VisiJet ® PXL Mater. User Guid. (2019) 1. https://www.think3d.in/wp-content/uploads/2017/07/logeeksdm_3dsystems_visijetpxl.pdf.

[34] 3D Systems, Open A Part In 3D Print | ProJet CJP x60 (260, 360, 460), User Guid. - Color. Instant Infiltrant. (2019) 2. http://infocenter.3dsystems.com/projetcjpx60/user-guide/setup-and-print-build/open-part-3d-print.

[35] 3D Systems, ProJet® x60 Series User Guide, Proj. X60 Ser. User Guid. (2019) 1–5. https://www.3dsystems.com/sites/default/files/projet-x60-series-us_0.pdf.

[36] S. Sharma, J.J. Sheng, Comparison of huff-n-puff gas injection and solvent injection in large-scale shale gas condensate reservoirs, J. Nat. Gas Sci. Eng. 52 (2018) 434–453. https://doi.org/10.1016/J.JNGSE.2017.10.007.

[37] L. Liu, X.-B. Luo, L. Ding, S.-L. Luo, Application of Nanotechnology in the Removal of Heavy Metal From Water, Nanomater. Remov. Pollut. Resour. Reutil. (2019) 83–147. https://doi.org/10.1016/B978-0-12-814837-2.00004-4.

[38] Micromeritics, Micromeritics 3Flex Surface Analyzer, Micromeritics. (2019) 1–17. https://www.micromeritics.com/Repository/Files/3Flex_Customer_Presentation_Website.pdf.

[39] F.J. Trogus, T. Sophany, R.S. Schechter, W.H. Wade, Static and Dynamic Adsorption of Anionic and Nonionic Surfactants, Soc. Pet. Eng. J. 17 (1977) 337–344. https://doi.org/10.2118/6004-PA.

[40] Z. Knor, Static Volumetric Methods for Determination of Absorbed Amount of Gases on Clean Solid Surfaces, Catal. Rev. 1 (1968) 257–313. https://doi.org/10.1080/01614946808064706.

[41] K.Y. Foo, B.H. Hameed, Insights into the modeling of adsorption isotherm systems, Chem. Eng. J. 156 (2010) 2–10. https://doi.org/10.1016/J.CEJ.2009.09.013.

[42] S. Brunauer, P.H. Emmett, E. Teller, Adsorption of Gases in Multimolecular Layers, J. Am. Chem. Soc. 60 (1938) 309–319. https://doi.org/10.1021/ja01269a023.

[43] V. Bolis, Fundamentals in Adsorption at the Solid-Gas Interface. Concepts and Thermodynamics BT - Calorimetry and Thermal Methods in Catalysis, in: A. Auroux (Ed.), Springer Berlin Heidelberg, Berlin, Heidelberg, 2013: pp. 3–50. https://doi.org/10.1007/978-3-642-11954-5_1.

[44] Z. Ye, D. Chen, Z. Pan, G. Zhang, Y. Xia, X. Ding, An improved Langmuir model for evaluating methane adsorption capacity in shale under various pressures and temperatures, J. Nat. Gas Sci. Eng. 31 (2016) 658–680. https://doi.org/10.1016/J.JNGSE.2016.03.070.

[45] I. Langmuir, THE ADSORPTION OF GASES ON PLANE SURFACES OF GLASS, MICA AND PLATINUM., J. Am. Chem. Soc. 40 (1918) 1361–1403. https://doi.org/10.1021/ja02242a004.

[46] P. Chènebault, A. Schürenkämper, The Measurement of Small Surface Areas by the B.E.T. Adsorption Method1, J. Phys. Chem. 69 (1965) 2300–2305. https://doi.org/10.1021/j100891a027.

[47] K.S.. Sing, Adsorption methods for the characterization of porous materials, Adv. Colloid Interface Sci. 76–77 (1998) 3–11. https://doi.org/10.1016/S0001-8686(98)00038-4.

[48] B.C. Lippens, J.H. de Boer, Studies on pore systems in catalysts: V. The t method, J. Catal. 4 (1965) 319–323. https://doi.org/10.1016/0021-9517(65)90307-6.

[49] W.D. Harkins, G. Jura, Surfaces of Solids. XII. An Absolute Method for the Determination of the Area of a Finely Divided Crystalline Solid, J. Am. Chem. Soc. 66 (1944) 1362–1366. https://doi.org/10.1021/ja01236a047.

[50] D. Ongari, P.G. Boyd, S. Barthel, M. Witman, M. Haranczyk, B. Smit, Accurate Characterization of the Pore Volume in Microporous Crystalline Materials, Langmuir. 33 (2017) 14529–14538. https://doi.org/10.1021/acs.langmuir.7b01682.

[51] E.P. Barrett, L.G. Joyner, P.P. Halenda, The Determination of Pore Volume and Area Distributions in Porous Substances. I. Computations from Nitrogen Isotherms, J. Am. Chem. Soc. 73 (1951) 373–380. https://doi.org/10.1021/ja01145a126.

[52] R. Sun, W. Yu, F. Xu, H. Pu, J. Miao, Compositional simulation of CO2 Huff-n-Puff process in Middle Bakken tight oil reservoirs with hydraulic fractures, Fuel. 236 (2019) 1446–1457. https://doi.org/10.1016/J.FUEL.2018.09.113.

[53] H.J. Deglint, C.R. Clarkson, A. Ghanizadeh, C. DeBuhr, J.M. Wood, Comparison of micro- and macro-wettability measurements and evaluation of micro-scale imbibition rates for unconventional reservoirs: Implications for modeling multi-phase flow at the micro-scale, J. Nat. Gas Sci. Eng. 62 (2019) 38–67. https://doi.org/10.1016/J.JNGSE.2018.11.026.

[54] Y. Yu, X. Luo, Z. Wang, M. Cheng, Y. Lei, L. Zhang, J. Yin, A new correction method for mercury injection capillary pressure (MICP) to characterize the pore structure of shale, J. Nat. Gas Sci. Eng. 68 (2019) 102896. https://doi.org/10.1016/J.JNGSE.2019.05.009.

[55] J.T. Comisky, M. Santiago, B. McCollom, A. Buddhala, K.E. Newsham, Sample Size Effects on the Application of Mercury Injection Capillary Pressure for Determining the Storage Capacity of Tight Gas and Oil Shales, in: Can. Unconv. Resour. Conf., Society of Petroleum Engineers, Calgary, Alberta, Canada, 2011: p. 23. https://doi.org/10.2118/149432-MS.

[56] Micromeritics, AutoPore IV Series - Automated Mercury Porosimeters, Micromeritics. (2012). http://www.micromeritics.com/Repository/Files/AutoPore_IV_Series_Mercury_Porosimeters_Brochure.pdf.

[57] J. Shafer, J. Neasham, Mercury Porosimetry Protocol for Rapid Determination of Petrophysical and Reservoir Quality Properties, Int. Symp. Soc. Core Anal. (2000) 18–22.

[58] E.W. Washburn, Note on a Method of Determining the Distribution of Pore Sizes in a Porous Material, Proc. Natl. Acad. Sci. U. S. A. 7 (1921) 115–116. https://doi.org/10.1073/pnas.7.4.115.

[59] M.J. Blunt, B. Bijeljic, H. Dong, O. Gharbi, S. Iglauer, P. Mostaghimi, A. Paluszny, C. Pentland, Pore-scale imaging and modelling, Adv. Water Resour. 51 (2013) 197–216. https://doi.org/10.1016/J.ADVWATRES.2012.03.003.

[60] H.A. Nooruddin, M.E. Hossain, Modified Kozeny–Carmen correlation for enhanced hydraulic flow unit characterization, J. Pet. Sci. Eng. 80 (2011) 107–115. https://doi.org/10.1016/J.PETROL.2011.11.003.

[61] M. Seppä, High-quality two-stage resampling for 3-D volumes in medical imaging, Med. Image Anal. 11 (2007) 346–360. https://doi.org/10.1016/J.MEDIA.2007.03.002.

[62] Z. Pan, W. Chen, Z. Jiang, L. Tang, Y. Liu, Z. Liu, Performance of global look-up table strategy in digital image correlation with cubic B-spline interpolation and bicubic interpolation, Theor. Appl. Mech. Lett. 6 (2016) 126–130. https://doi.org/10.1016/J.TAML.2016.04.003.

[63] A.O. Adelu, A.A. Aderemi, A.O. Akanji, O.A. Sanuade, S.I. Kaka, O. Afolabi, S. Olugbemiga, R. Oke, Application of 3D static modeling for optimal reservoir characterization, J. African Earth Sci. 152 (2019) 184–196. https://doi.org/10.1016/J.JAFREARSCI.2019.02.014.

[64] H. Luo, M. Delshad, G.A. Pope, K.K. Mohanty, Scaling up the interplay of fingering and channeling for unstable water/polymer floods in viscous-oil reservoirs, J. Pet. Sci. Eng. 165 (2018) 332–346. https://doi.org/10.1016/J.PETROL.2018.02.035.

[65] M.A. Oliver, R. Webster, A tutorial guide to geostatistics: Computing and modelling variograms and kriging, CATENA. 113 (2014) 56–69. https://doi.org/10.1016/J.CATENA.2013.09.006.

[66] M.A. Oliver, The Variogram and Kriging BT - Handbook of Applied Spatial Analysis: Software Tools, Methods and Applications, in: M.M. Fischer, A. Getis (Eds.), Springer Berlin Heidelberg, Berlin, Heidelberg, 2010: pp. 319–352. https://doi.org/10.1007/978-3-642-03647-7_17.

[67] M. Armstrong, Improving the Estimation and Modelling of the Variogram BT - Geostatistics for Natural Resources Characterization: Part 1, in: G. Verly, M. David, A.G. Journel, A. Marechal (Eds.), Springer Netherlands, Dordrecht, 1984: pp. 1–19. https://doi.org/10.1007/978-94-009-3699-7_1.

[68] E.C. Donaldson, G. V Chilingarian, T.F. Yen, M.K. Sharma, Chapter 1 Introduction, in: E.C. Donaldson, G. V Chilingarian, T.F.B.T.-D. in P.S. Yen (Eds.), Enhanc. Oil Recover. II, Elsevier, 1989: pp. 1–11. https://doi.org/https://doi.org/10.1016/S0376-7361(08)70453-9.

[69] A.M. AlSofi, J.S. Liu, M. Han, S. Aramco, Numerical simulation of surfactant–polymer coreflooding experiments for carbonates, J. Pet. Sci. Eng. 111 (2013) 184–196. https://doi.org/10.1016/J.PETROL.2013.09.009.

[70] N. Alyafei, T.J. Mckay, T.I. Solling, Characterization of petrophysical properties using pore-network and lattice-Boltzmann modelling: Choice of method and image sub-volume size, J. Pet. Sci. Eng. 145 (2016) 256–265. https://doi.org/10.1016/J.PETROL.2016.05.021.

[71] B. Jia, L. Jin, B.A.F. Mibeck, S.A. Smith, J.A. Sorensen, An integrated approach of measuring permeability of naturally fractured shale, J. Pet. Sci. Eng. (2019) 106716. https://doi.org/10.1016/J.PETROL.2019.106716.

[72] G.N. Boitnott, Use of Complex Pore Pressure Transients to Measure Permeability of Rocks, SPE Annu. Tech. Conf. Exhib. (1997) 9. https://doi.org/10.2118/38717-MS.

[73] S. Whitaker, Flow in porous media I: A theoretical derivation of Darcy's law, Transp. Porous Media. 1 (1986) 3–25. https://doi.org/10.1007/BF01036523.

[74] B. Abdelmalek, Z.T. Karpyn, S. Liu, H. Yoon, T. Dewers, Gas permeability measurements from pressure pulse decay laboratory data using pseudo-pressure and pseudo-time transformations, J. Pet. Explor. Prod. Technol. 8 (2018) 839–847. https://doi.org/10.1007/s13202-017-0376-5.

[75] A. Mathur, C.H. Sondergeld, C.S. Rai, Comparison of Steady-State and Transient Methods for Measuring Shale Permeability, SPE Low Perm Symp. (2016) 22. https://doi.org/10.2118/180259-MS.

[76] C. Cao, Numerical interpretation of transient permeability test in tight rock, J. Rock Mech. Geotech. Eng. 10 (2018) 32–41. https://doi.org/10.1016/J.JRMGE.2017.07.009.

[77] Y. Bernabé, U. Mok, B. Evans, A note on the oscillating flow method for measuring rock permeability, Int. J. Rock Mech. Min. Sci. 43 (2006) 311–316. https://doi.org/10.1016/J.IJRMMS.2005.04.013.

[78] C.A. Jermy, B.J. Venter, A simple apparatus for measuring the permeability of borehole core, Bull. Int. Assoc. Eng. Geol. - Bull. l'Association Int. Géologie l'Ingénieur. 52 (1995) 79–83. https://doi.org/10.1007/BF02602684.

[79] E. Hosseini, R. Gholami, F. Hajivand, Geostatistical modeling and spatial distribution analysis of porosity and permeability in the Shurijeh-B reservoir of Khangiran gas field in Iran, J. Pet. Explor. Prod. Technol. 9 (2019) 1051–1073. https://doi.org/10.1007/s13202-018-0587-4.

[80] D.I. Gerogiorgis, M. Georgiadis, G. Bowen, C.C. Pantelides, E.N. Pistikopoulos, Dynamic oil and gas production optimization via explicit reservoir simulation, Comput. Aided Chem. Eng. 21 (2006) 179–184. https://doi.org/10.1016/S1570-7946(06)80043-X.

[81] New England Research Inc., Autolab 1500 Manual, Autolab 1500 Man. (2009). https://www.ner.com/site/systems/autolab-series/autolab-1500.html.

[82] R.L. Kranz, J.S. Saltzman, J.D. Blacic, Hydraulic diffusivity measurements on laboratory rock samples using an oscillating pore pressure method, Int. J. Rock Mech. Min. Sci. Geomech. Abstr. 27 (1990) 345–352. https://doi.org/10.1016/0148-9062(90)92709-N.

[83] G.J. Fischer, Chapter 8 The Determination of Permeability and Storage Capacity: Pore Pressure Oscillation Method, Int. Geophys. 51 (1992) 187–211. https://doi.org/10.1016/S0074-6142(08)62823-5.

[84] I. Song, J. Renner, Analysis of oscillatory fluid flow through rock samples, Geophys. J. Int. 170 (2007) 195–204. https://doi.org/10.1111/j.1365-246X.2007.03339.x.

[85] W.F. Brace, J.B. Walsh, W.T. Frangos, Permeability of granite under high pressure, J. Geophys. Res. 73 (1968) 2225–2236. https://doi.org/10.1029/JB073i006p02225.

[86] K. Ling, J. He, P. Pei, S. Wang, Comparisons of Biot's Coefficients of Bakken Core Samples Measured by Three Methods, 2016.

[87] V.I. Malkovsky, A. V Zharikov, V.M. Shmonov, New methods for measuring the permeability of rock samples for a single-phase fluid, Izv. Phys. Solid Earth. 45 (2009) 89–100. https://doi.org/10.1134/S1069351309020013.

[88] M. Mokhtari, A. Tutuncu, Characterization Of Anisotropy In The Permeability Of Organic-Rich Shales, J. Pet. Sci. Eng. 133 (2015) 496–506. https://doi.org/10.1016/j.petrol.2015.05.024.

[89] A.L. Manríquez, K. Sepehrnoori, The diffusivity equation for geopressure prediction using well logs, J. Pet. Sci. Eng. 134 (2015) 186–198. https://doi.org/10.1016/J.PETROL.2014.10.009.

[90] F. Zhou, A. Shi, X. Wang, An efficient finite difference model for multiphase flow in fractured reservoirs, Pet. Explor. Dev. 41 (2014) 262–266. https://doi.org/10.1016/S1876-3804(14)60031-8.

[91] K. Aziz, A. Settari, A New Iterative Method For Solving Reservoir Simulation Equations, J. Can. Pet. Technol. 11 (1972) 8. https://doi.org/10.2118/72-01-04.

[92] K. Schouhamer Immink, J.H. Weber, Minimum Pearson Distance Detection for Multilevel Channels With Gain and/or Offset Mismatch, Inf. Theory, IEEE Trans. 60 (2014) 5966–5974. https://doi.org/10.1109/TIT.2014.2342744.

[93] S.A. Sadrnejad, Modeling Heterogeneity And Anisotropy Of Rocks, ISRM Int. Symp. - 5th Asian Rock Mech. Symp. (2008) 8. https://doi.org/.

[94] W.J. Al-Mudhafar, From Coreflooding and Scaled Physical Model Experiments to Field-Scale Enhanced Oil Recovery Evaluations: Comprehensive Review of the Gas-Assisted Gravity Drainage Process, Energy & Fuels. 32 (2018) 11067–11079. https://doi.org/10.1021/acs.energyfuels.8b01023.

[95] N. Goodwin, M. Powell, Simulation and Uncertainty: Lessons From Other Industries, W. Ahead. 08 (2012) 20–24. https://doi.org/10.2118/0312-020-TWA.

[96] T. Ahmed, T. Ahmed, Fundamentals of Reservoir Fluid Flow, Reserv. Eng. Handb. (2010) 331–483. https://doi.org/10.1016/B978-1-85617-803-7.50014-6.

[97] J.H. Abou-Kassem, S.M.F. Ali, M.R. Islam, Chapter 1 - Introduction, in: J.H. Abou-Kassem, S.M.F. Ali, M.R.B.T.-P.R.S. Islam (Eds.), Gulf Publishing Company, 2006: pp. 1–6. https://doi.org/https://doi.org/10.1016/B978-0-9765113-6-6.50007-1.

[98] T. Budney, C. Jose, H. Jacot, T. Svarczkopf, Optimized Rock Fluid Interaction and Stimulation Intensity Enhancement Improves Well Performance: A Marcellus Case Study, SPE/AAPG East. Reg. Meet. (2018) 9. https://doi.org/10.2118/191798-18ERM-MS.

[99] A. Kumar, C.L. Farmer, G.R. Jerauld, D. Li, Efficient Upscaling from Cores to Simulation Models, SPE Annu. Tech. Conf. Exhib. (1997) 16. https://doi.org/10.2118/38744-MS.

[100] A. Vilela, I. Fjelde, Modeling of Interaction Between CO2 and Rock in Core Flooding Experiments., SPE Heavy Oil Conf. (2013) 8. https://doi.org/10.2118/165500-MS.

[101] M.A. Christie, Upscaling for Reservoir Simulation, J. Pet. Technol. 48 (1996) 1004–1010. https://doi.org/10.2118/37324-JPT.

[102] F.J. Hasiuk, L.J. Florea, M.C. Sukop, Three-Dimensional Printing: Transformative Technology for Experimental Groundwater Research, Groundwater. 54 (2016) 157–158. https://doi.org/10.1111/gwat.12394.

[103] F. Hasiuk, C. Harding, Touchable topography: 3D printing elevation data and structural models to overcome the issue of scale, Geol. Today. 32 (2016) 16–20. https://doi.org/10.1111/gto.12125.

[104] M. Guvendiren, J. Molde, R.M.D. Soares, J. Kohn, Designing Biomaterials for 3D Printing, ACS Biomater. Sci. Eng. 2 (2016) 1679–1693. https://doi.org/10.1021/acsbiomaterials.6b00121.

[105] S. Bose, S. Vahabzadeh, A. Bandyopadhyay, Bone tissue engineering using 3D printing, Mater. Today. 16 (2013) 496–504. https://doi.org/10.1016/J.MATTOD.2013.11.017.

[106] J.-Y. Jung, S.E. Naleway, Y.N. Maker, K.Y. Kang, J. Lee, J. Ha, S.S. Hur, S. Chien, J. McKittrick, 3D Printed Templating of Extrinsic Freeze-Casting for Macro–Microporous Biomaterials, ACS Biomater. Sci. Eng. 5 (2019) 2122–2133. https://doi.org/10.1021/acsbiomaterials.8b01308.

[107] C. Jiang, G.-F. Zhao, A Preliminary Study of 3D Printing on Rock Mechanics, Rock Mech. Rock Eng. 48 (2015) 1041–1050. https://doi.org/10.1007/s00603-014-0612-y.

[108] L. Kong, M. Ostadhassan, S. Fereshtenejad, J.-J. Song, C. Li, Anisotropy Analysis of 3D Printed Gypsum Rocks Integrating Pulse-Transmission, Nanoindentation and Micro-CT Techniques, 52nd U.S. Rock Mech. Symp. (2018) 7. https://doi.org/.

[109] L. Li, Y. Su, J.J. Sheng, Y. Hao, W. Wang, Y. Lv, Q. Zhao, H. Wang, Experimental and Numerical Study on CO2 Sweep Volume during CO2 Huff-n-Puff Enhanced Oil Recovery Process in Shale Oil Reservoirs, Energy & Fuels. 33 (2019) 4017–4032. https://doi.org/10.1021/acs.energyfuels.9b00164.

[110] W. Yu, H. Lashgari, K. Sepehrnoori, Simulation Study of CO2 Huff-n-Puff Process in Bakken Tight Oil Reservoirs, SPE West. North Am. Rocky Mt. Jt. Meet. (2014) 16. https://doi.org/10.2118/169575-MS.

[111] A. Abedini, F. Torabi, Oil Recovery Performance of Immiscible and Miscible CO2 Huff-and-Puff Processes, Energy & Fuels. 28 (2014) 774–784. https://doi.org/10.1021/ef401363b.

[112] R. Wu, Prediction of CO2 Miscibility Pressures, Tech. Meet. / Pet. Conf. South Saskatchewan Sect. (1995) 29. https://doi.org/10.2118/95-142.

[113] S.M. Al-Mutairi, S.A. Abu-khamsin, M.E. Hossain, A Novel Approach to Handle Continuous Wettability Alteration during Immiscible CO2 Flooding Process, Abu Dhabi Int. Pet. Conf. Exhib. (2012) 12. https://doi.org/10.2118/160638-MS.

[114] C.A. Kang, A.R. Brandt, L.J. Durlofsky, Optimizing heat integration in a flexible coal–natural gas power station with CO2 capture, Int. J. Greenh. Gas Control. 31 (2014) 138–152. https://doi.org/10.1016/J.IJGGC.2014.09.019.

[115] Y. Yang, C. Li, N. Wang, Z. Yang, Progress and prospects of innovative coal-fired power plants within the energy internet, Glob. Energy Interconnect. 2 (2019) 160–179. https://doi.org/10.1016/J.GLOEI.2019.07.007.

[116] J. (John) Sun, A. Zou, E. Sotelo, D. Schechter, Numerical Simulation of CO2 Huff-n-puff in Complex Fracture Networks of Unconventional Liquid Reservoirs, J. Nat. Gas Sci. Eng. 31 (2016). https://doi.org/10.1016/j.jngse.2016.03.032.

[117] D. Janiga, R. Czarnota, J. Stopa, P. Wojnarowski, Huff and puff process optimization in micro scale by coupling laboratory experiment and numerical simulation, Fuel. 224 (2018) 289–301. https://doi.org/10.1016/J.FUEL.2018.03.085.

[118] A.G. Almetwally, H. Jabbari, Experimental Investigation of 3D Printed Rock Samples Replicas, J. Nat. Gas Sci. Eng. (2020) 103192. https://doi.org/10.1016/J.JNGSE.2020.103192.

[119] Y. Wei, Z.J. Chen, M. Satyro, C.C. Dong, H. Deng, Compositional Simulation Using an Advanced Peng-Robinson Equation of State, SPE Reserv. Simul. Symp. (2011) 12. https://doi.org/10.2118/141898-MS.

[120] A. Al-Qasim, M.A. AlDawsari, Comparison Study of Asphaltene Precipitation Models Using UTCOMP, CMG/GEM and ECLIPSE Simulators, SPE Oil Gas India Conf. Exhib. (2017) 16. https://doi.org/10.2118/185370-MS.

[121] R. Ehrlich, J.H. Tracht, S.E. Kaye, Laboratory and Field Study of the Effect of Mobile Water on CO2-Flood Residual Oil Saturation, J. Pet. Technol. 36 (1984) 1797–1809. https://doi.org/10.2118/11957-PA.

[122] A.R. Traki, M. Sohrabi, The impact of rock pore structure on Co2 relative permeability, Int. Pet. Technol. Conf. (2014) 17. https://doi.org/10.2523/IPTC-18125-MS.

[123] X. Zhou, Q. Yuan, X. Peng, F. Zeng, L. Zhang, A critical review of the CO2 huff ‘n’ puff process for

enhanced heavy oil recovery, Fuel. 215 (2018) 813–824. https://doi.org/10.1016/J.FUEL.2017.11.092.

[124] W.W. Symes, I.S. Terentyev, T.W. Vdovina, Gridding Requirements For Accurate Finite Difference Simulation, 2008 SEG Annu. Meet. (2008) 5. https://doi.org/.

[125] D.R. Hoffman, Petrel Workflow for Adjusting Geomodel Properties for Simulation, SPE Middle East Oil Gas Show Conf. (2013) 16. https://doi.org/10.2118/164420-MS.

[126] S. Sharma, J.J. Sheng, Z. Shen, A Comparative Experimental Study of Huff-n-Puff Gas Injection and Surfactant Treatment in Shale Gas-Condensate Cores, Energy & Fuels. 32 (2018) 9121–9131. https://doi.org/10.1021/acs.energyfuels.8b01816.

[127] F. Rodriguez, A. Galindo-Nava, A General Formulation for Compositional Reservoir Simulation, Int. Pet. Conf. Exhib. Mex. (1994) 15. https://doi.org/10.2118/28705-MS.

[128] L. Schmall, A. Varavei, K. Sepehrnoori, A Comparison of Various Formulations for Compositional Reservoir Simulation, SPE Reserv. Simul. Symp. (2013) 16. https://doi.org/10.2118/163630-MS.

[129] K.H. Coats, An Equation of State Compositional Model, Soc. Pet. Eng. J. 20 (1980) 363–376. https://doi.org/10.2118/8284-PA.

[130] A. Varavei, K. Sepehrnoori, An EOS-Based Compositional Thermal Reservoir Simulator, SPE Reserv. Simul. Symp. (2009) 15. https://doi.org/10.2118/119154-MS.

[131] Z. Chen, Reservoir Simulation: Mathematical Techniques in Oil Recovery, Society for Industrial and Applied Mathematics, 2008. https://books.google.com/books?id=A6sfxAEACAAJ.

[132] L.X. Nghiem, V.K. Shrivastava, D. Tran, B.F. Kohse, M.S. Hassam, C. Yang, Simulation of CO2 Storage in Saline Aquifers, SPE/EAGE Reserv. Charact. Simul. Conf. (2009) 15. https://doi.org/10.2118/125848-MS.

[133] P.L. Randolph, Natural Gas From Geopressured Aquifers?, SPE Annu. Fall Tech. Conf. Exhib. (1977) 12. https://doi.org/10.2118/6826-MS.

[134] S. Sona, K. Sasaki, Y. Sagai, A. Fujiwara, Numerical Simulation on Solubility of CO2 in Aquifer, SPWLA 19th Form. Eval. Symp. Japan. (2013) 5. https://doi.org/.

[135] B. Jia, J.-S. Tsau, R. Barati, Measurement of CO2 Diffusion Coefficient in the Oil-Saturated Porous Media, Abu Dhabi Int. Pet. Exhib. Conf. (2018) 15. https://doi.org/10.2118/192703-MS.

[136] D. Alfarge, M. Wei, B. Bai, Factors Affecting CO2-EOR in Shale-Oil Reservoirs: Numerical Simulation Study and Pilot Tests, Energy & Fuels. 31 (2017) 8462–8480. https://doi.org/10.1021/acs.energyfuels.7b01623.

[137] B. Kurtoglu, H. Kazemi, R. Rosen, W. Mickelson, T. Kosanke, A Rock and Fluid Study of Middle Bakken Formation: Key to Enhanced Oil Recovery, SPE/CSUR Unconv. Resour. Conf. – Canada. (2014) 19. https://doi.org/10.2118/171668-MS.

[138] D. Head, T. Vanorio, Effects of changes in rock microstructures on permeability: 3-D printing investigation, Geophys. Res. Lett. 43 (2016) 7494–7502. https://doi.org/10.1002/2016GL069334.

[139] O. Torsæter, M. Abtahi, EXPERIMENTAL RESERVOIR ENGINEERING LABORATORY WORK BOOK, 2003.

[140] L.W. Lake, Enhanced oil recovery, Prentice Hall, 1989. https://books.google.com/books?id=nm5MAQAAIAAJ.

[141] J.R. Fanchi, Principles of Applied Reservoir Simulation, Elsevier Science, 2005. https://books.google.com/books?id=lyEDWVqE1_YC.

[142] S.P. Sinha, SPE 93491 Numerical Simulation To Design and Analyze Pressure Transient Tests in a Shaly , Interbedded Reservoir, Society. 93491-MS (2005).

[143] B.H. Hahn, D.T. Valentine, B.H. Hahn, D.T. Valentine, Introduction to Numerical Methods, Essent. MATLAB Eng. Sci. (2017) 295–323. https://doi.org/10.1016/B978-0-08-100877-5.00016-5.

[144] S.D. Mohaghegh, Data-driven Reservoir Modeling: Top-down Modeling (TDM) : a Paradigm Shift in Reservoir Modeling, the Art and Science of Building Reservoir Models Based on Field Measurements, Society of Petroleum Engineers, 2017. https://books.google.com/books?id=W8DktAEACAAJ.

[145] M. Kelkar, G. Perez, A. Chopra, Applied Geostatistics for Reservoir Characterization, Society of

Petroleum Engineers, 2002. https://books.google.com/books?id=jBHdAAAACAAJ.

[146] P. Pankaj, Characterizing Well Spacing, Well Stacking, and Well Completion Optimization in the Permian Basin: An Improved and Efficient Workflow Using Cloud-Based Computing, SPE/AAPG/SEG Unconv. Resour. Technol. Conf. (2018) 29. https://doi.org/10.15530/URTEC-2018-2876482.

[147] S. Ishutov, T.D. Jobe, S. Zhang, M. Gonzalez, S.M. Agar, F.J. Hasiuk, F. Watson, S. Geiger, E. Mackay, R. Chalaturnyk, Three-dimensional printing for geoscience: Fundamental research, education, and applications for the petroleum industry, Am. Assoc. Pet. Geol. Bull. 102 (2018) 1–26. https://doi.org/10.1306/0329171621117056.

[148] F. Watson, J. Maes, S. Geiger, E. Mackay, M. Singleton, T. McGravie, T. Anouilh, T.D. Jobe, S. Zhang, S. Agar, S. Ishutov, F. Hasiuk, Comparison of Flow and Transport Experiments on 3D Printed Micromodels with Direct Numerical Simulations, Transp. Porous Media. 129 (2019) 449–466. https://doi.org/10.1007/s11242-018-1136-9.

[149] M. Bacher, A. Schwen, J. Koestel, Three-Dimensional Printing of Macropore Networks of an Undisturbed Soil Sample, Vadose Zo. J. 14 (2015). https://doi.org/10.2136/vzj2014.08.0111.

[150] S. Ishutov, F.J. Hasiuk, S.M. Fullmer, A.S. Buono, J.N. Gray, C. Harding, Resurrection of a reservoir sandstone from tomographic data using three-dimensional printing, Am. Assoc. Pet. Geol. Bull. 101 (2017) 1425–1443. https://doi.org/10.1306/11111616038.

[151] M. Bourke, H.A. Viles, J. Nicoli, P. Lyew-Ayee, R. Ghent, J. Holmlund, Innovative applications of laser scanning and rapid prototype printing to rock breakdown experiments, Earth Surf. Process. Landforms. 33 (2008) 1614–1621. https://doi.org/10.1002/esp.1631.

[152] B. Berman, 3-D printing: The new industrial revolution, Bus. Horiz. 55 (2012) 155–162. https://doi.org/10.1016/J.BUSHOR.2011.11.003.

[153] N.A. Idowu, C. Nardi, H. Long, T. Varslot, P.-E. Øren, Effects of Segmentation and Skeletonization Algorithms on Pore Networks and Predicted Multiphase-Transport Properties of Reservoir-Rock Samples, SPE Reserv. Eval. Eng. 17 (2014) 473–483. https://doi.org/10.2118/166030-PA.

[154] W. Gao, Y. Zhang, D. Ramanujan, K. Ramani, Y. Chen, C.B. Williams, C.C.L. Wang, Y.C. Shin, S. Zhang, P.D. Zavattieri, The status, challenges, and future of additive manufacturing in engineering, Comput. Des. 69 (2015) 65–89. https://doi.org/10.1016/J.CAD.2015.04.001.

[155] K. Roebuck, 3D Printing: High-Impact Emerging Technology - What You Need to Know Definitions, Adoptions, Impact, Benefits, Maturity, Vendors, Tebbo, 2011.

[156] H. Kim, E. Park, S. Kim, B. Park, N. Kim, S. Lee, Experimental Study on Mechanical Properties of Single- and Dual-material 3D Printed Products, Procedia Manuf. 10 (2017) 887–897. https://doi.org/10.1016/J.PROMFG.2017.07.076.

[157] B. Redwood, F. Schoffer, B. Garret, The 3D printing handbook : technologies, design and applications, 2017.

[158] B. Evans, Practical 3D Printers: The Science and Art of 3D Printing, 1st ed., Apress, USA, 2012.

[159] K. Bisdom, B.D.M. Gauthier, G. Bertotti, N.J. Hardebol, Calibrating discrete fracture-network models with a carbonate three-dimensional outcrop fracture network: Implications for naturally fractured reservoir modeling, Am. Assoc. Pet. Geol. Bull. 98 (2014) 1351–1376. https://doi.org/10.1306/02031413060.

[160] A. Salmachi, E. Dunlop, M. Rajabi, Z. Yarmohammadtooski, S. Begg, Investigation of permeability change in ultradeep coal seams using time-lapse pressure transient analysis: A pilot project in the Cooper Basin, Australia, Am. Assoc. Pet. Geol. Bull. 103 (2019) 91–107. https://doi.org/10.1306/05111817277.

[161] R.M. Sneider, J.S. Sneider, NEW OIL IN OLD PLACES, Am. Assoc. Pet. Geol. Bull. 83 (1999). https://doi.org/10.1306/E4FD4765-1732-11D7-8645000102C1865D.

[162] A.-C. Sarr, L. Husson, P. Sepulchre, A.-M. Pastier, K. Pedoja, M. Elliot, C. Arias-Ruiz, T. Solihuddin, S. Aribowo, Susilohadi, Subsiding Sundaland: REPLY, Geology. 47 (2019) e470–e470. https://doi.org/10.1130/G46493Y.1.

[163] N. Fernandez, M.R. Hudec, C.A.-L. Jackson, T.P. Dooley, O.B. Duffy, The competition for salt and kinematic interactions between minibasins during density-driven subsidence: observations from numerical models, Pet. Geosci. (2019). https://doi.org/10.1144/petgeo2019-051.

[164] M. Maleki, A. Davolio, D.J. Schiozer, Qualitative time-lapse seismic interpretation of Norne Field to assess challenges of 4D seismic attributes, Lead. Edge. 37 (2018) 754–762. https://doi.org/10.1190/tle37100754.1.

[165] A. Suman, T. Mukerji, Sensitivity study of rock-physics parameters for modeling time-lapse seismic response of Norne field, Geophysics. 78 (2013) D511–D523. https://doi.org/10.1190/geo2013-0045.1.

[166] A. G. Almetwally and H. Jabbari, "3D-Printing Replication of Porous Media for Lab-Scale Characterization Research," *ACS Omega*, vol. 6, no. 4, pp. 2655–2664, Feb. 2021.